Ignition and Flame Stabilization in *n*-dodecane Turbulent Premixed Flames at Compression Ignition Engine Conditions

Samyar Farjam

Thesis submitted to the University of Ottawa
for the degree of
Master of Applied Science in Mechanical Engineering

Department of Mechanical Engineering
Faculty of Engineering
University of Ottawa

Abstract

Controlling ignition timing and flame stabilization is one of the most outstanding challenges limiting the development of modern, efficient and low-emission compression ignition engines (CIEs). In this study, the role of turbulence on two-stage ignition dynamics and subsequent flame stabilization at diesel engine conditions is assessed by performing direct numerical simulations in a simplified inflow-outflow premixed configuration. The thermochemical conditions are chosen to match those of the most reactive mixture in the Engine Combustion Network's *n*-dodecane Spray A flame (temperature of 813 K, pressure of 60 atm, equivalence ratio of 1.3, and with 15% vol. O_2 in the ambient gas). Inflow velocities 4 to 16 times larger than the laminar flame speed are considered. As a result, in the absence of turbulence, ignition and flame stabilization are controlled by advection and chemistry, diffusion being negligible. Ignition delays match those of the homogeneous reactor and both the cool flame, due to low-temperature chemistry (LTC), and the hot flame, due to high-temperature chemistry (HTC), are spontaneous ignition fronts. Turbulence alters this picture in two ways. First, the second-stage (HTC) ignition delay is increased considerably, in contrast with the first-stage (LTC) ignition delay, which remains virtually unaffected. Second, a sufficiently high turbulence intensity makes the cool spontaneous ignition front transition to a cool deflagration which moves upstream to the inlet, while the hot flame is pushed downstream, still stabilized by spontaneous ignition. The latter phenomenon is caused by the reduced reactivity of LTC products as the cool flame transitions from spontaneous ignition to deflagration. Further increasing the turbulence intensity leads to both cool and hot flames transitioning to deflagrations. For the hot flame, the mechanism governing this transition is the increase in magnitude of progress variable gradient under increased turbulence or reduced inflow velocity, while in cool flames it is mainly due to the reduction in chemical source terms. In addition to turbulence intensity, the role of inflow velocity, integral length scale, and oxygen concentration level on this transition is assessed and modeling challenges are discussed. Finally, a chemical explosive

mode analysis is provided to further characterise the ignition and transition phenomena. The present results highlight important fundamental roles of turbulence expected to modulate CIE combustion dynamics.

Acknowledgements

First and foremost I would like to thank my advisor Prof. Bruno Savard for giving me the opportunity to work in his team. I gained much knowledge and insight on combustion and flames, mostly numerical analysis and working with supercomputers. His valuable guidance and continuous care throughout my studies helped me carry out this research in the appropriate timeframe. The quality of his work and the projects made me enthusiastic on pursuing my studies towards PhD.

I gratefully acknowledge the support of the Natural Sciences and Engineering Research Council of Canada (NSERC), [funding reference numbers RGPIN-2019-04309 , RGPAS-2019-00131 , DGCER-2019-00390]. Computational resources were provided by Compute Ontario and Compute Canada.

Contents

List of figures

List of tables

Nomenclature

α	mixture thermal diffusivity
$\boldsymbol{\sigma}$	viscous stress tensor
$\boldsymbol{a}_{\text{exp}}$	right eigenvector associated with the most explosive mode
$\boldsymbol{b}_{\text{exp}}$	left eigenvector associated with the most explosive mode
$\boldsymbol{f}$	turbulence forcing term
$\boldsymbol{I}$	identity matrix
$\boldsymbol{J}_{\boldsymbol{\omega}}$	chemical Jacobian
$\boldsymbol{j}_i$	ith species diffusion mass flux
$\boldsymbol{s}$	non-chemical source term
$\boldsymbol{u}$	velocity
$\chi_{r'}$	dissipation rate of the fluctuating component of the residence time
δ	reaction zone thickness
$\dot{\boldsymbol{\omega}}$	chemical source term
$\dot{\omega}_i$	ith species production rate
$\dot{\omega}_T$	temperature production rate
$\dot{\omega}_{i,c}$	ith species consumption rate
$\dot{\omega}_{i,p}$	ith species production rate
ϵ	turbulent kinetic energy dissipation rate

η	Kolmogorov length scale
λ	conductivity of the mixture
λ_{exp}	the eigenvalue of $\boldsymbol{J}_{\boldsymbol{\omega}}$ associated with the most explosive mode
$\mathcal{D}_{i,m}$	ith species mixture-averaged diffusion coefficient
$\mathcal{D}_{ij}$	binary diffusion coefficient of ith species relative to jth species
$\mathcal{D}_i$	ith species mixture-averaged diffusivity
μ	mixture dynamic viscosity
ν	kinematic viscosity
ν_{js}	stoichiometric coefficient of species s in reaction j
ω_c	mean progress variable source term
ϕ	equivalence ratio
ϕ_s	projected diffusion term onto the most explosive mode
ϕ_ω	projected chemical term onto the most explosive mode
ρ	density
τ	0D ignition delay
τ_η	Kolmogorov time scale
τ_{ign}	ignition delay
$\tau_{t,o}$	integral eddy turnover time
a	constant
A_j	pre-exponential factor
b_j	temperature exponent
c	progress variable
c_p	mixture heat capacity
$c_{p,i}$	ith species heat capacity

D	diffusivity
Da	Damköhler number
Da_η	Kolmogorov Damköhler number
e_x	unit vector parallel to the inlet bulk flow
h_i	specific enthalpy of the ith species
h_i^0	specific enthalpy of the ith species at standard temperature T_0
k_j	chemical reaction constant
Ka	Karlovitz number
Ka_u	unburnt side Karlovitz number
Ka_δ	Karlovitz number in the reaction zone
L	length
l	integral length scale
L_f	laminar flame position
l_F	laminar flame thickness
L_x	duct length
L_y	duct height
L_z	duct width
Le	Lewis number
n	coordinate normal to the local progress variable iso-surface
N_x	x direction number of grid points
N_y	y direction number of grid points
N_z	z direction number of grid points
P	pressure
p	hydrodynamic pressure

P_0 thermodynamic pressure

r residence time

R_u universal gas constant

Re_t turbulent Reynolds number

S strain rate tensor

S_d^* density-weighted displacement speed

$S_{d,c}^*$ density-weighted curvature term of displacement speed

$S_{d,n}^*$ density-weighted normal diffusion term of displacement speed

$S_{d,r}^*$ density-weighted reaction term of displacement speed

S_L laminar reference speed

S_R laminar reference speed

S_{SP} speed of the spontaneous ignition front

T temperature

t time

T_b burnt temperature

t_F flame time

T_u unburnt temperature

t_{end} total simulation time

T_{aj} activation temperature of the jth reaction

u' root-mean-square of velocity fluctuations

U_{in} inflow velocity

$U_{in,trans}$ transition inflow velocity

W mixture molar weight

W_i ith species molecular weight

x physical coordinate

X_i ith species mole fraction

y physical coordinate

Y_i ith species mass fraction

z physical coordinate

List of Abbreviations

CIE	compression ignition engine
DNS	direct numerical simulation
ECN	engine combustion network
LTC	low-temperature chemistry
ITC	intermediate-temperature chemistry
HTC	high-temperature chemistry
GHG	green house gas
EGR	exhaust-gas re-circulation
HCCI	homogeneous charge compression ignition
LES	large eddy simulation
RANS	Reynolds average Navier-Stokes
NTC	negative temperature coefficient
HRR	heat release rate
DME	dimethyl ether
TKE	turbulent kinetic energy
MSG	mean scalar gradient
HIT	homogeneous isotropic turbulence
CEMA	chemical explosive mode analysis

CEM chemical explosive mode

REDIM reaction-diffusion manifold

Chapter 1

Introduction

1.1 Background

1.1.1 Environmental imperatives

In the last few decades, global warming and climate change have sparked major concerns all around the globe as these have been linked to a broad range of observed effects that are destructive and dangerous for current and future societies [56]. Global warming is mainly due to fossil fuel burning [144], which increases heat-trapping greenhouse gas (GHG) [62, 76] levels in Earth's atmosphere. Due to their high volumetric energy density, fossil fuels have long been used to power aerial, road, and maritime vehicles through combustion engines. However, in recent years, drastic reductions in regulation limits for exhaust emissions have obligated manufacturers and researchers to improve the design of combustion technologies in order to conform to these stringent environmental requirements.

In an effort to achieve this goal, many industries are moving towards development of sustainable energy [12, 29, 30, 40, 49, 77] using new green technologies. In general terms, switching to green electricity [113], zero-carbon fuels (*e.g.,* hydrogen) in combustion engines [40, 46, 77], or fuel cells [50, 91, 115, 128, 181] can potentially be the solution in the long term. However, the transition to such "fully green" alternatives requires substantial technological development and faces inertia to change in some energy or transportation sectors.

1.1.2 Alternative perspectives to conventional fuels in transportation engines

There is no doubt that fully electrical vehicles [106, 146] or vehicles propelled by hydrogen fuel-cells [33, 69, 75] are gaining popularity for light-duty and personal transport. However, for heavy-duty trucks, cargo ships [4, 11, 88, 143], and aviation [18, 22, 195], the complete transition to fully electric or fuel-cell propulsion is not expected soon and it seems out of reach for at least two to three decades to come [51, 104, 151, 152, 171, 185, 188]. Instead, effectively using alternative fuels with lower carbon content in combustion engines is anticipated in a short to mid-term perspective.

In that regard, hydrogen and ammonia (NH_3) are considered as possible surrogates to replace heavy-hydrocarbon fuels and there is a growing body of work in the literature that deals with understanding the fundamentals of hydrogen [8, 57, 65, 162] and ammonia flames [16, 93, 116, 148] in engine conditions. However, applicability of these fuels in currently commercialized combustion engines is very limited and it will take several decades of technological development and certification (in particular for the aviation sector) to fully transition to a large-scale utilization of zero-carbon fuels. An alternative approach is to mix zero-carbon fuels such as hydrogen or ammonia with carbon-containing fuels such as traditional fossil fuels (*e.g.*, diesel, kerosene) [48, 148, 186] or bio-derived fuels (*e.g.*, bio-diesel, ethanol) [15, 84, 183, 206] for improved GHG footprint, while maintaining combustion characteristics more compatible with current engine technology. Nevertheless, with this approach, improved fundamental understanding of the complex combustion processes involved in transportation engines is needed to further reduce emission levels and pave the way to a full transition to zero-carbon combustion.

1.1.3 Controlling ignition and flame stabilization in advanced transportation combustion engines

Traditionally, compression ignition engines (CIEs) and jet engines operate in a non-premixed mode, while spark-ignition engines operate in a premixed mode [24]. In non-premixed systems, ignition and flame stabilization can be more easily controlled, since chemical reactions take place at the boundary between the fuel and oxidizer streams where a local stoichiometric mixture can be found. This relative ease of control enables more optimal engine designs in terms of overall fuel efficiency. However, non-premixed

combustion leads to high products temperature, resulting in high NO_x production, as well as soot formation on the fuel-rich side. In premixed systems, the fuel-to-air ratio (equivalence ratio) can be tuned to strongly limit NO_x and eliminate soot production, *i.e.,* by running fuel lean. However, the propagation of premixed flames coupled with the lack of precise ignition control in a nearly homogeneous fuel-air mixture constrains the optimization of premixed combustion engines.

There have been extensive efforts to reduce GHG, NO_x, and soot emissions in the context of using carbon-containing fuels such as diesel, kerosene, biodiesel [81, 92, 120], or even partial mixtures of these fuels with hydrogen and ammonia [103, 110, 122, 147, 148, 192] in CIEs and jet engines. For CIEs, in-cylinder strategies helped reduce emissions without sacrificing much power. These strategies included utilization of higher fuel injection pressure, mixture intake habituation [140], injection and ignition timing adjustments [41, 66, 66, 86, 145, 184], and improved combustion chamber design [90]. Furthermore, exhaust-gas re-circulation (EGR) at high rates was employed [32, 78, 97, 139]. EGR at such high rates showed many drawbacks, mainly, decreasing efficiency [32]. Following these, aftertreatment devices were improved to further tackle the emission problem [72, 150]. Diesel emission control research has provided viable technologies using aftertreatment but its widespread adoption is hindered by higher economic cost, durability issues, economical inefficiency, and greater space requirement [83]. Moreover, reduction of NO_x is a significant challenge for diesel exhaust aftertreatment. As a result, researchers and manufacturers have mainly focused on in-cylinder strategies in the recent years. Accordingly, two implementations have been recently studied: 1) reducing combustion temperatures, and 2) using premixed or partially premixed fuel/oxidizer mixtures [15, 119]. The latter approach led, in addition to the low-temperature diesel combustion concept [119], to the development of the homogeneous charge compression ignition (HCCI) engine and other variations [149] which all aim at combining the efficiency of the diesel engine with the emission level of the spark-ignition engine. For jet engines, similar strategies are favoured, *i.e.*, increased premixing and reduction of combustion temperature, in part through EGR [15]. While decreasing products temperature, EGR comes with higher unburnt mixture temperature which can lead to autoignition [15]. Overall, for these strategies to be successfully implemented, a detailed understanding of ignition and flame stabilization in increasingly autoignitive premixed systems is needed.

Most carbon-containing transportation fuels are composed in significant proportion of linear alkanes or chemical compounds with similar chemical characteristics. An alkane

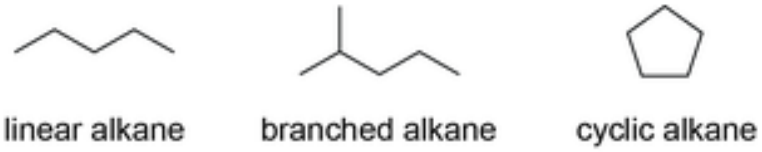

FIGURE 1.1: Alkane bond types.

consists of hydrogen and carbon atoms arranged in a tree structure in which all the carbon–carbon bonds are single. Alkanes have the general chemical formula of $\mathrm{C_nH_{2n+2}}$. Linear alkanes are alkane compounds with straight-chain bonds and are usually prefixed with "*n*-" to distinguish them from branched-chain, and cyclic-chain isomers as depicted in Fig. 1.1. The simplest linear alkane is methane ($\mathrm{CH_4}$), while compounds such as *n*-heptane ($\mathrm{C_7H_{16}}$) [5, 34, 166, 196] and *n*-dodecane ($\mathrm{C_{12}H_{26}}$) [59, 127, 165, 166, 198] are larger linear alkanes generally included in surrogates for real fuels [34, 35, 114, 121]. An important attribute of $\mathrm{C_3}$+ linear alkanes (linear alkanes at least as heavy as propane) is their two-stage ignition behavior at engine conditions [63, 117], *i.e.,* a first stage due to low-temperature chemistry (LTC) [85], and a second stage due to high temperature chemistry (HTC) (more information on linear alkanes chemical pathways in Section 2.1). The LTC is responsible for shorter ignition delays, which means that the chemistry of large linear alkanes such as *n*-heptane and *n*-dodecane is expected to control ignition and likely to control flame stabilization under autoignitive conditions in advanced transportation engines [15, 85, 119].

1.1.4 The Engine Combustion Network's Spray A reference case

The Engine Combustion Network (ECN) is an international platform organized to coordinate engine combustion research towards a common goal [3, 14, 126, 135]. This platform contains vast series of experimental and numerical reference flames at various conditions for combustion model development and validation. In particular, the heavy linear alkane, *n*-dodecane flame at diesel engine condition (Spray A) is one such flame that has been extensively investigated [3, 126, 127, 135, 176] to provide fundamental understanding of the complex turbulence-chemistry interaction in CIEs. Yet its relevance is not only limited to CIEs, as similar thermofluid complexity can be encountered in HCCI-like engines and advanced jet engines, namely the interaction of strong turbulence with large *n*-alkane-air autoignitive mixtures under high pressure.

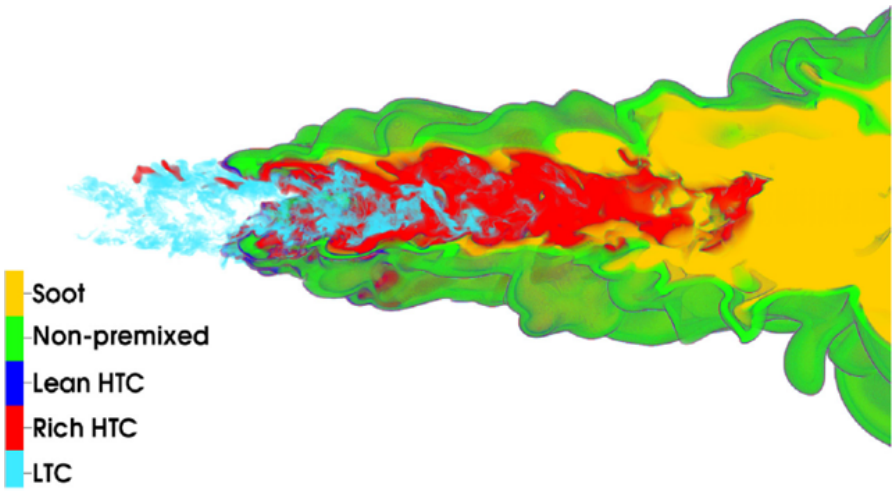

FIGURE 1.2: Conceptual model of diesel spray combustion. Figure taken from Dalakoti *et al.* [37].

The *n*-dodecane Spray A flame is characterized by a highly complex structure as summarized by Dec [42] and Musculus *et al.* [119]. A rendered representation of a downscaled high-fidelity simulation of a Spray A flame, performed by Dalakoti *et al.* [37], is shown in Fig 1.2. Downstream of the fuel jet, LTC occurs first, followed by a shrouding non-premixed flame stabilized in the products of LTC. A rich premixed combustion region sits in the center of the jet, inside the non-premixed flame, and a sooting region follows downstream of the reaction zone.

The Spray A flame has been studied over a wide range of conditions experimentally [14, 126, 127, 135, 175], as well as numerically, using Reynolds-averaged Navier-Stokes (RANS) simulations [17, 28], large eddy simulation (LES) [39, 193, 194, 204], and direct numerical simulations (DNS) [37, 165, 208]. There are several theories aimed at predicting its stabilization mechanism. In general it is suspected that both ignition and deflagration can play a role [94, 136]. A suggested stabilization mechanism is through edge flame propagation (at the intersection of a lean premixed flame, a rich premixed flame and a diffusion flame) which highlights the importance of understanding flame propagation under Spray A conditions. A number of numerical studies attempted to match the ignition delays observed in experiments [14, 175, 193], but fundamental understanding of the role of turbulence on ignition delay remains elusive.

1.2 Knowledge gap addressed

Based on the above discussion, to reduce GHG, NO_x, and soot emissions from advanced CIEs and jet engines, improved control of ignition timing and flame stabilization is desired. Although zero-carbon fuels are expected to be introduced as additives, due to the high reactivity of heavy linear alkanes present in current transportation fuels, their chemical kinetics is likely to control ignition and flame stabilization. However, there is only limited understanding of the role of turbulence on two-stage ignition and flame stabilization (characteristic of heavy linear alkanes) at engine conditions.

Since it is extremely challenging to resolve experimentally turbulence-chemistry interaction at their finest scales at high pressure engine conditions [127], previous fundamental work focused on DNS to resolve all such scales [20, 37]. However, due to the high computational cost associated with DNS, the authors of these studies chose to include as much complexity as possible in single simulations. Large parametric DNS studies of two-stage ignition and flame stabilization at engine conditions have not yet been performed. Here, the approach taken is to reduce the complexity by considering only premixed mixtures to enable such parametric study to be conducted.

Understanding premixed combustion at Spray A conditions is highly relevant to elucidate the complex ignition and flame stabilization process in the actual partially premixed flame. In particular, edge flames (triple flames) are likely to control flame stabilization, and these flames can propagate in a deflagrative or spontaneous ignition manner, similar to fully premixed flames. Furthermore, partially premixed turbulent combustion is often modelled as a continuous series of premixed flames [105] and this approach was shown to capture well the structure of the downscaled Spray A flame performed by Dalakoti *et al.* [36–38]. In general, as discussed in Section 1.1 understanding autoignitive two-stage premixed combustion becomes increasingly important to most advanced transportation engines.

1.3 Objectives

In this numerical study, the role of turbulence on the flame stabilization regime and ignition delay in a fully premixed environment at Spray A diesel engine conditions is investigated. Reduced detailed chemical kinetics of *n*-dodecane combustion, including LTC and HTC, is considered. A canonical inflow-outflow configuration is implemented

and direct numerical simulations (DNS) are performed. In particular, the objectives are as follows: 1) identify and model the role of turbulence on the flame stabilization regime and, 2) quantify and explain the impact of stabilization mode on ignition delay.

1.4 Thesis Outline

The rest of this thesis is organized as follows. First, a literature review of the fundamentals and state-of-the-art research relevant to the problem studied is provided in Chapter 2. In Chapter 3, a description of the governing equations, numerical approach, reference laminar flames, and the turbulent flames setup is provided. In Chapter 4, a comprehensive analysis of the turbulent flames is performed, from qualitative analysis to various quantitative results to provide a valid description of flame ignition timing, stabilization, and transition mechanism. Finally, conclusions and a discussion on recommended future work are provided in Chapter 5.

Chapter 2

Literature review

In this chapter, fundamentals of autoignitive turbulent premixed flames relevant to engine combustion are reviewed. First, ignition characteristics and chemical kinetics of large *n*-alkanes are discussed. Second, basics of non-autoignitive laminar premixed flames are introduced. Third, premixed flames under autoignitive conditions are discussed, with a focus on the duality between deflagrations and spontaneous ignition fronts. Fourth, turbulence theory is briefly presented. Fifth, classical non-autoignitive turbulent premixed flame regimes are reviewed. Finally, recent results on turbulent autoignitive premixed flames are discussed.

2.1 Large *n*-alkane chemistry and the negative temperature coefficient regime

As the temperature of a fuel-oxidizer mixture increases, chemical reactions are promoted and as a result, ignition delay generally decreases. The negative temperature coefficient (NTC) regime refers to a range of temperature over which the opposite behavior is seen [19, 94, 125, 134, 155, 179, 202]. The NTC regime is an essential feature of low-temperature combustion for large *n*-alkane fuels. Figure 2.1, taken from the CaltechMech resources website [19], illustrates the NTC regime for *n*-heptane/air combustion at an equivalence ratio of unity ($\phi = 1$), in a constant pressure homogeneous reactor. Results are considered from Cizeki *et al.* [31] (blue), Minetti [118] (orange), Gauthier *et al.* [58] (red), Shen *et al.* [172] (green), and Heufer *et al.* [74] (red circle).

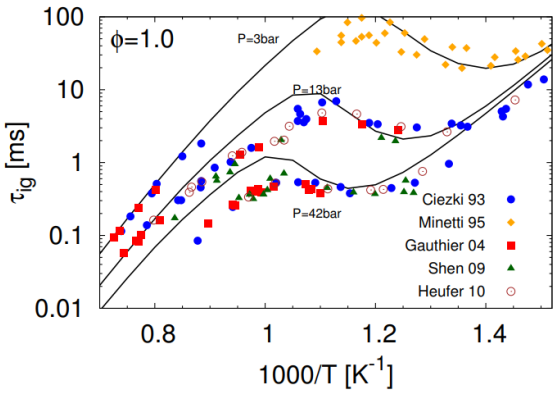

FIGURE 2.1: Ignition delay time *vs.* inverse of temperature. The figure is added from [19].

The numerical results obtained with CaltechMech [19] are indicated using solid lines. Ignition delay (second-stage) is shown with respect to the inverse of temperature.

In the NTC regime, ignition occurs in two stages as depicted in Fig. 2.2 for a representative mixture of large *n*-alkane fuel at CIE thermochemical conditions. A first ignition stage is followed by a period of relatively low heat release rate (HRR), before a second ignition stage takes place at higher temperature. The chemical pathways controlling these ignition stages and the lower reactivity intermediate period are introduced below.

Here, oxidation pathways for large *n*-alkane fuels in the NTC regime are presented following the studies of Curran *et al.* [34] and Ju *et al.* [85]. It is argued that three sets

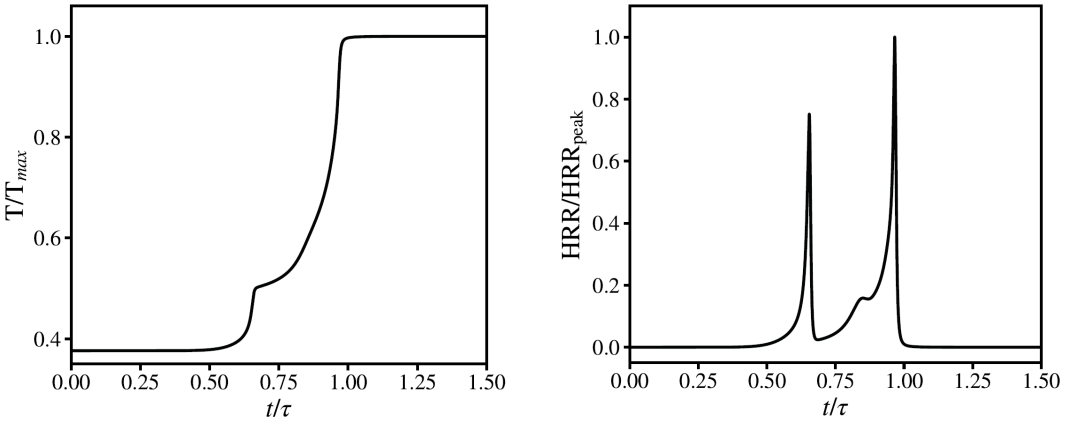

(a) Temperature normalized with the maximum temperature *vs.* time.

(b) HRR normalized with the peak HRR *vs.* time.

FIGURE 2.2: Temperature (a) and HRR (b) temporal evolution of a representative ignition in the NTC regime at CIE thermochemical conditions. The solution is obtained from a constant pressure homogeneous reactor numerical simulation using Cantera [60]. The thermochemical conditions are those introduced in Section 3.3. τ is the (second-stage) ignition delay.

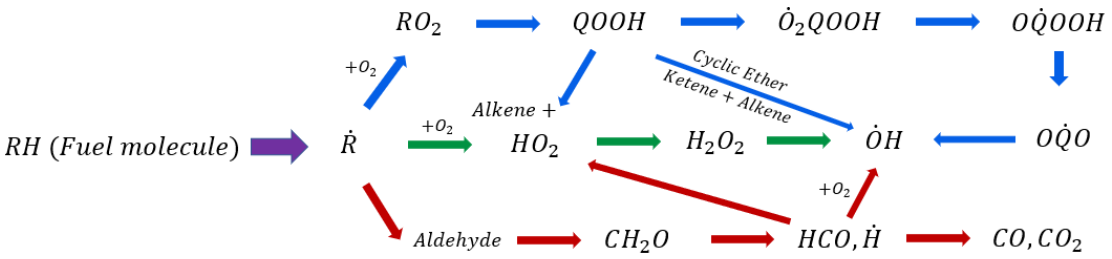

FIGURE 2.3: A reduced schematic of reaction pathways for linear alkane type fuel, at high (red arrow), intermediate (green arrow), and low temperatures (blue arrow.

of chain-branching reaction pathways exist with respect to temperature. These chain-branches are referred to as low temperature chemistry (LTC), intermediate temperature chemistry (ITC), and high temperature chemistry (HTC) pathways [85, 201, 205]. According to Fig. 2.3 (taken from [85]) these pathways are produced as follows:

LTC:

$$\dot{\mathrm{R}} \rightarrow \mathrm{R\dot{O}_2} \rightarrow \dot{\mathrm{Q}}\mathrm{OOH} \rightarrow \mathrm{\dot{O}_2QOOH} \rightarrow \mathrm{O\dot{Q}OOH} \rightarrow \mathrm{O\dot{Q}O} + \dot{\mathrm{O}}\mathrm{H} \tag{2.1}$$

ITC:

$$\dot{\mathrm{R}} \rightarrow \mathrm{HO_2} \rightarrow \mathrm{H_2O_2} \rightarrow \dot{\mathrm{O}}\mathrm{H} \tag{2.2}$$

$$\dot{\mathrm{Q}}\mathrm{OOH} \rightarrow \mathrm{alkene} + \mathrm{HO_2} \rightarrow \mathrm{H_2O_2} + \dot{\mathrm{O}}\mathrm{H} \tag{2.3}$$

$$\dot{\mathrm{Q}}\mathrm{OOH} \rightarrow \mathrm{ketene} + \mathrm{alkene} + \mathrm{ether} + \dot{\mathrm{O}}\mathrm{H} \tag{2.4}$$

$$\mathrm{CH_2O} \rightarrow \mathrm{HCO} \rightarrow \mathrm{HO_2} \rightarrow \mathrm{H_2O_2} \rightarrow \dot{\mathrm{O}}\mathrm{H} \tag{2.5}$$

HTC:

$$\dot{\mathrm{R}} \rightarrow \mathrm{aldehyde} \rightarrow \mathrm{CH_2O} \rightarrow \mathrm{HCO} + \dot{\mathrm{H}} + \dot{\mathrm{O}}\mathrm{H} \tag{2.6}$$

Through the LTC pathway, as denoted in Eq. 2.1, the $\dot{\mathrm{H}}$ radical is segregated from the fuel molecule (RH) producing the fuel radical ($\dot{\mathrm{R}}$). The fuel radical combines with $\mathrm{O_2}$ molecules and forms alkylperoxy ($\mathrm{R\dot{O}_2}$) which then leads to the formation of the hydroperoxy-alkyl radical ($\dot{\mathrm{Q}}\mathrm{OOH}$). Then, $\dot{\mathrm{Q}}\mathrm{OOH}$ advancement at low temperatures goes through a second addition of $\mathrm{O_2}$ molecule to form $\mathrm{\dot{O}_2QOOH}$ which then can turn into $\mathrm{O\dot{Q}OOH}$. Lastly ketohydroperoxide ($\mathrm{O\dot{Q}O}$) and $\dot{\mathrm{O}}\mathrm{H}$ are produced. $\dot{\mathrm{O}}\mathrm{H}$ is the main chain carrier of the LTC pathway [100]. The first peak in HRR observed in Fig. 2.2b is

due to LTC. As ignition introduces more heat to the mixture, the $\dot{\mathrm{Q}}\mathrm{OOH}$ compound described previously, aside from combining with $\mathrm{O_2}$, can disintegrate into either alkene, epoxide or β-scission products, leading to $\mathrm{H\dot{O}_2}$, $\mathrm{H_2O_2}$, and $\dot{\mathrm{O}}\mathrm{H}$ production. $\mathrm{H\dot{O}_2}$ is also produced at intermediate temperatures from fuel radical combining with $\mathrm{O_2}$. This chain branching phenomenon is referred to as ITC in the literature [85] as shown in Eqs. 2.2- 2.5. Note that another possible reaction in ITC channel can be the $\dot{\mathrm{R}}\mathrm{O_2} \rightarrow R$ reaction which dominates over the inverse reaction at sufficiently high temperature. Sufficiently high temperatures ultimately result in substantially slower fuel oxidation, promoting olefin production through β-scission with $\dot{\mathrm{O}}\mathrm{H}$ and $\mathrm{H\dot{O}_2}$ addition, following another chain branching path identified as HTC pathway [132] (Eq. 2.6). As temperature increases, ITC and HTC pathways are promoted and enter in competition with the LTC pathway. As ITC and HTC chain-branching is slow at temperatures at which LTC is active, this competition explains the drop in mixture reactivity following first-stage ignition (Fig. 2.2). HTC eventually dominates over ITC, leading to the second peak in HRR (second-stage ignition).

In Fig. 2.1 it was shown that temperature negatively impacts the ignition delay during a temperature interval which is called the NTC region. In conjecture on the fuel oxidation pathways described in this section, Curran *et al.* [34] showed through sensitivity analysis that the initial ITC reaction, $\dot{\mathrm{Q}}\mathrm{OOH} \rightarrow \mathrm{olefin} + \mathrm{epoxide}$, reduces the overall rate of oxidation in the lower temperature half of the NTC regime. This means that the mixture reactivity reduces and subsequently retards the occurrence of ignition as the ITC channel becomes more favored.

2.2 Laminar premixed flames

Laminar flow is characterized by fluid particles following smooth paths in layers where little to no mixing is observed. Generally, laminar flames are seen under conditions with low Reynolds numbers. An example of a laminar premixed flame is one produced by a Bunsen burner. The fuel (*e.g.*, natural gas) is well mixed with air inside the burner nozzle before reacting as the mixture flows through the flame. Since the temperature of the mixture is low (low reactivity), to initiate the flame, the premixed mixture must be ignited with the assistance of a spark, *i.e.*, the mixture is non-autoignitive. A flame eventually stabilizes over the nozzle as the fuel-air mixture flow rate is maintained.

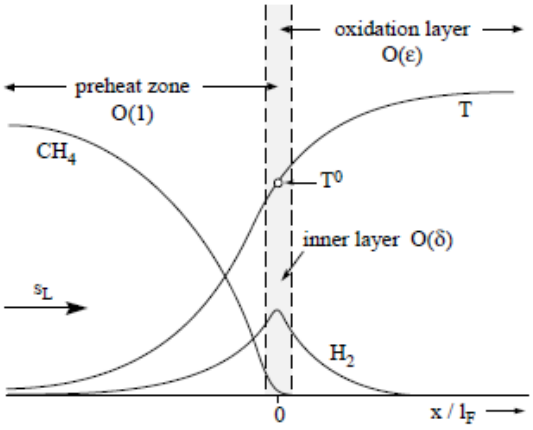

FIGURE 2.4: Schematic illustration of a methane-air premixed flame structure taken from [130].

Figure 2.4 added from [130] shows the conceptual structure of a simple non-autoignitive methane-air premixed flame consisting of a preheat zone caused by diffusion of heat and radicals upstream from a reaction zone, where most of the chemical reactions occur, and an oxidation layer, where slow reactions (associated with low heat release rate) take place. In the preheat zone, advection of chemical species and temperature is balanced by diffusion, while chemical reactions are balanced by diffusion in the reaction zone.

A (non-autoignitive) laminar premixed flame is characterized by its thickness l_F and its propagation speed (called laminar flame speed) S_L, *i.e.*, the speed normal to itself at which the flame moves in a frame of reference attached to the unburnt mixture. Both l_F and S_L depend strongly on the thermochemical parameters of the premixed gas ahead of the flame. The flame thickness, l_F, can be defined as (thermal flame thickness)

$$l_F = \frac{T_b - T_u}{|\nabla T|_{\max}}, \tag{2.7}$$

where T_u is the unburnt temperature, T_b is the temperature in the burnt mixture, and $|\nabla T|_{\max}$ is maximum temperature gradient. Introducing the heat diffusivity α, l_F can also be defined as (diffusion flame thickness)

$$l_F = \frac{\alpha}{S_L} \tag{2.8}$$

with

$$\alpha = \frac{\lambda}{\rho c_p}, \tag{2.9}$$

where c_p is the heat capacity and λ is the conductivity of the mixture. Furthermore, the

diffusion time through the flame thickness, also known as the flame characteristic time is given by

$$t_F = \frac{l_F}{S_L}. \tag{2.10}$$

2.3 Spontaneous ignition *vs.* deflagration

In order to understand the flame behavior, in particular, controlling the ignition timing and flame propagation [43], the mechanisms responsible for stabilization of the flame should be identified. In that regard, various studies have suggested that two types of propagation regimes known as spontaneous ignition and deflagration are liable to control flame stabilization. Spontaneous ignition occurs when flame stabilization is controlled by advection and chemistry due to an increase in mixture reactivity stimulated by increase of temperature or compression without interference of an external source of ignition, such as a flame or spark. If a homogeneous premixed fuel-air mixture is preheated to sufficient temperatures at proper pressure, chain branching reactions accelerate the generation of radicals and heat which subsequently leads to a thermal runaway. If the residence time within the combustion chamber is sufficiently long, autoignition will occur. Deflagration is a phenomenon that occurs when flame propagation is dominated by molecular and heat diffusion from the flame front towards the unburnt mixture (reactants) sitting at the preheat zone. This deflagrative combustion wave travels at subsonic speeds through the unburnt gas immediately ahead of the flame front causing the temperature and reactivity of the unburnt side mixture to increase, leading to ignition of the preheat zone. This procedure is observed as a flame moving towards the inlet (burning the mixture ahead of the flame through diffusion). Deflagrations propagating through a non-autoignitive mixture were discussed in the previous section. In autoignitive conditions, a flame front can also propagate as a deflagration. The transition from a spontaneous ignition to a deflagration in such conditions is discussed below. Note that if the wave is supersonic, a different combustion mode called detonation [101, 102] is observed which is not the focus of this study.

The occurrence of spontaneous ignition *vs.* deflagration is expected to depend on the ignition delay and the residence time of ignitable mixtures. Zeldovich [203] pioneered the classification of combustion regimes in autoignitive conditions. It was suggested

that the temperature inhomogeneities will initiate a sequence of thermal explosions that propagate down the imposed negative temperature gradient. Moreover, the spontaneous ignition front takes place and propagates if the inverse of the magnitude of ignition delay gradients is larger than the laminar reference speed S_L (deflagration speed limit). The aforementioned criterion is as follows

$$S_L < S_{SP} = \frac{1}{|\nabla \tau_{\text{ign}}|} \tag{2.11}$$

where S_{SP} is the speed of the spontaneous ignition front and τ_{ign} is the local ignition delay. The ignition delay is the time span of the induction process preceding the thermal runaway (remaining time to ignition) and it depends on the kinetic properties of the reaction process and the local mixture composition, temperature and pressure (or, alternatively, the initial composition, temperature and pressure, and the time history of the local fluid element). As the ignition delay gradient diminishes, the velocity of the flame front continues increasing while for high ignition delay gradients, due to diffusive transport, the flame speed refuses to drop lower than the laminar flame speed. In open combustion systems, gradients in ignition delay that are mostly attributed to gradients in residence time. This is relevant to jet engines or during fuel injection in diesel engines. In closed combustion systems, gradients in ignition delay are attributed to gradients in mixture composition or temperature. This is the case for the problem of knock in gasoline engines or ignition timing in HCCI engines, where the residence time of the fuel-air mixture following a compression stroke is uniform. Consistently, high-fidelity simulation studies have shown that in the context of HCCI the magnitude of temperature or composition fluctuation gradients controls the propagation regime (*i.e.,* spontaneous ignition or deflagration) of reacting fronts [26, 71, 112, 157, 202].

As a foundation for turbulent studies, steady-state laminar flames [68, 95, 96, 164, 166, 168, 169, 197] have been previously discussed to investigate the transition from spontaneous ignition fronts to deflagrations. Krisman *et al.* [95] investigated the laminar combustion of dimethyl ether-air mixture in an inflow-outflow domain within which both hot and cool flames were stabilized. It was shown that at sufficiently large inflow velocity, the hot flame, due to HTC, and the cool flame, due to LTC, stabilize as spontaneous ignition fronts. As the inflow velocity decreases, diffusion becomes dominant and the lifted flame propagates upstream. Note that for these conditions, at low inflow velocity, deflagrative cool flame would not be observed, since the hot flame would overtake the cool flame. This is while Savard *et al* [166] showed that for *n*-heptane and *n*-dodecane (Spray A) in autoignitive conditions, laminar deflagrative cool flames exist

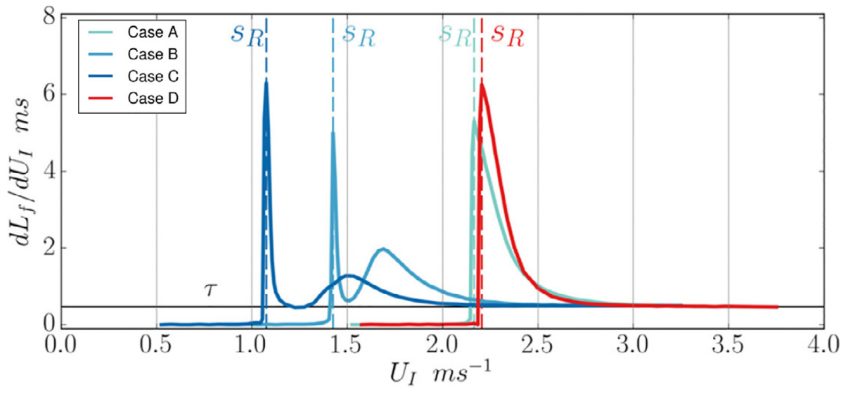

FIGURE 2.5: Flame position response to U_{in} modified from [95]. Case (A) DME above the NTC region with one-stage ignition, Case (B) DME in the NTC regime with two-stage ignition, Case (C) DME below the NTC region with two-stage ignition, Case (D) ethanol which has a single-stage autoignition without NTC.

in the NTC regime. The autoignitive flame fronts are stabilized at a distance called the lift-off length denoted by L_{f}. A hot spontaneous ignition flame front is found until, upon decreasing the inflow velocity U_{in}, $\mathrm{d}L_{\mathrm{f}}/\mathrm{d}U_{\mathrm{in}}$ reaches a maximum, beyond which the flame is a deflagration. Upon further decreasing U_{in}, the deflagration eventually attaches to the inlet. The velocity at which this transition threshold occurs was termed the laminar reference speed, denoted s_{R}. This deflagration speed is analogous to the laminar flame speed S_L in non-autoignitive conditions. Note that S_L instead of s_R will be used in the next chapters to denote the laminar reference flame speed. Examples of $\mathrm{d}L_{\mathrm{f}}/\mathrm{d}U_{\mathrm{in}}$ *vs.* U_{in} plots obtained by Krisman *et al.* [95] for DME (cases A, B, and C) and ethanol (case D) are shown in Fig. 2.5.

Finally, Soriano and Richardson [178] observed a similar transition in methane-*n*-heptane-air mixtures and provided a model to describe the contribution of pre-ignition chemistry.

2.4 Turbulence

Turbulence is an unsteady, random and chaotic feature of fluid flow. In its essence, a large range of intermixing and interacting length scales are induced appearing as random collection of coherent structures. These structures can show some regularity when examined statistically [142].

In practicality, combustion devices are usually subject to a turbulent flow. Although turbulent flows are difficult to predict and control due to their random motion, they result in rapid mixing which increases rates of momentum, mass and heat transfer, as

well as turbulent flame speed. It follows that power output with respect to engine size is increased under turbulent condition.

Turbulent flows are characterized by their amplitudes, length scales and time scales. For a particular turbulent flow field, three primary kinematic properties are considered: the turbulent kinetic energy, the turbulent kinetic energy dissipation rate ϵ and the kinematic viscosity ν. The turbulent kinetic energy (TKE) is defined as

$$\mathrm{TKE} = \frac{3}{2}u'^2, \tag{2.12}$$

where u' is the root-mean-square (rms) of turbulent velocity fluctuations or turbulence intensity. The small coherent structures often called eddies are defined by various length scales. These length scales are associated with different velocity and time scales. The life span of the eddies containing most of the TKE, know as the integral eddy turnover time, is obtained as

$$\tau_{t,o} = \frac{l}{u'}, \tag{2.13}$$

where the integral length scale l corresponds to the length scale with the largest TKE density (*i.e.*, the wave number associated with l is the wave number at which the TKE spectrum peaks).

For statistically steady homogeneous isotropic turbulence there is a steady transfer of TKE from large to small scale eddies and the TKE is consumed at small scales through viscous dissipation (eddy cascade hypothesis [142]). Dissipation acts on all eddies but it is far more significant on the smaller eddies as they are subjected to the largest local velocity gradients. Therefore, for smaller length scales, viscosity and dissipation play the important role so as the smallest scale of dynamic importance in turbulence called the Kolmogorov scale is defined as

$$\eta = \left(\frac{\nu^3}{\epsilon}\right)^{1/4}. \tag{2.14}$$

The Kolmogorov time scale is defined as

$$\tau_\eta = \left(\frac{\nu}{\epsilon}\right)^{1/2}. \tag{2.15}$$

Moreover, using the largest and the smallest scales, and the turbulent Reynolds number Re_t, a relation between these properties can be derived as

$$\frac{l}{\eta} = {Re_t}^{3/4}, \tag{2.16}$$

with

$$Re_t = \frac{u'l}{\nu}. \tag{2.17}$$

Note that the above is a very brief description of turbulence. More details can be found in the books of Pope [142] and Tennekes and Lumley [187].

2.5 Classical turbulent premixed flame regimes

Classical turbulent premixed flame regimes were proposed in the context of turbulent deflagrations only. More precisely, the unburnt mixture is assumed to be non-autoignitive. Turbulent premixed flames in autoignitive conditions are reviewed in the next section.

Several non-dimensional numbers are introduced. The Damköhler number, a ratio of transport to chemical time scales, is introduced as:

$$Da = \frac{\tau_{t,o}}{t_F} = \frac{S_L l}{u' l_F}. \tag{2.18}$$

The Karlovitz number is defined as the inverse of Damköhler number based on the Kolmogorov scale rather than the integral scale:

$$Ka = {Da_\eta}^{-1} = \frac{t_F}{\tau_\eta}. \tag{2.19}$$

Using Eq. 2.14 and 2.15, the Kolmogorov time scale can be expressed as

$$\tau_\eta = \frac{\eta^2}{\nu}. \tag{2.20}$$

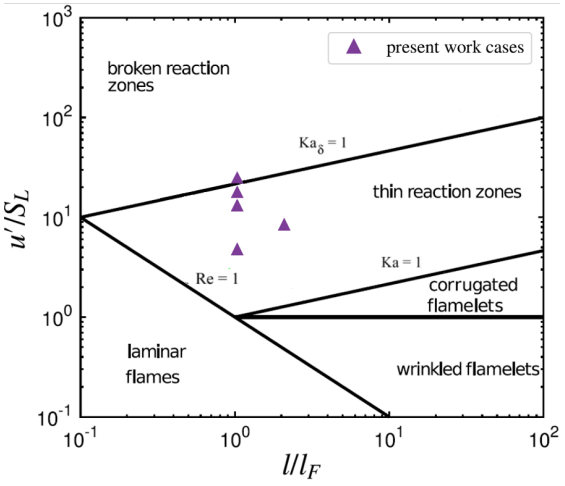

FIGURE 2.6: Turbulent premixed flames regime diagram as proposed by Peters [129].

Assuming unity Prandtl number, using Eq. 2.8 for the flame thickness, and combining with Eq. 2.10, 2.19 and 2.20, the Karlovitz number can be simplified to

$$Ka = \frac{{l_F}^2}{\eta^2}. \tag{2.21}$$

A reaction zone Karlovitz number was also defined by Peters [131] as

$$Ka_\delta = \frac{\delta^2}{\eta^2}, \tag{2.22}$$

where δ is the reaction zone thickness.

Using these non-dimensional numbers, several regimes are identified based on scaling arguments in the literature [1, 21, 129, 130, 141]. A well accepted regime diagram is proposed by Peters [129] as shown in Fig. 2.6. In this diagram, to delimit boundaries between the different regimes of premixed turbulent combustion various lines are depicted. The line $Re_t = 1$ separates laminar from turbulent flames, the line $u'/S_L = 1$ separates the wrinkled and corrugated flamelets, $Ka = 1$ separates the thin reaction zones regime from the corrugated flamelet regime, and lastly $Ka_\delta = 1$ separates the thin reaction zones regime from the broken/distributed reaction zones regime. Note that Ka_δ is often approximated as 100 times larger than Ka, hence $Ka_\delta = 1$ could be replaced by $Ka = 100$.

These regimes are characterized as follows. (Recall that here it is assumed that premixed flames propagate in non-autoignitive conditions, i.e., they are deflagrations.) For $u'/S_L < 1$ the flame is wrinkled and laminar. In this regime, flame propagation is dominant and the displacement by S_L is faster than displacement by u'. For $u'/S_L > 1$ while

$Ka < 1$, the flame is corrugated. Here, eddies are too large to penetrate the flame, but are sufficiently strong to corrugate the flame front. If $Ka > 1$ and $Ka_\delta < 1$, turbulence enables the disruption of the flame by having sufficiently small eddies to penetrate and thicken the preheat zone through turbulent mixing. For $Ka_\delta > 1$ or $Ka > 100$ it is argued that the small eddies can penetrate the reaction zone, either thickening it, hence distributed reaction zone, or disrupting it, hence broken reaction zone.

Most practical applications used in the industry perform under high values of Ka. Therefore, experimental [27, 52–54, 79, 138, 177, 180, 207] and numerical [6–8, 52, 70, 99, 108, 159, 160, 190] studies have focused on the structure of turbulent premixed flames by employing sufficiently high Ka. Particularly, the thin reaction zones regime has been consistently observed for flames at moderate unburnt temperatures [7, 8, 52, 99, 108, 156, 159, 177], *i.e.*, when a significant preheat zone is present. Distributed and broken reaction zones have also been identified [10, 52, 99, 165, 207]. However, there is no perfect match with the theory discussed above. In particular, distributed and broken reaction zones have been identified at much lower Ka than expected, due to the coupling between turbulence, differential diffusion and chemistry [8, 159] or the small relative thickness of the preheat zone (at higher unburnt temperature) [165]. It is clear from the literature that other parameters such as mean flow shear, equivalence ratio, fuel, and unburnt temperature cannot be neglected to accurately predict the turbulent premixed flame structure. Nevertheless, due to lack of a better simple regime diagram, the above identifications are still consistently used to provide nominal regimes based on experimental or simulation parameters. In this study, mixture properties and ambient conditions are defined based on the aforementioned regime diagram such that the flame regimes fall in the region of thin reaction zones regime as shown with purple symbols in Fig 2.6.

2.6 Turbulent premixed autoignitive flames

In HCCI engines, flame stabilization and controlling ignition timing are the current challenges deferring their applicability [43]. Previously, mixture sensitivity to temperature variations has been studied fundamentally to understand the advent and propagation of ignition kernels in HCCI conditions [26, 44, 71, 80, 82, 124, 154, 157, 182, 202]. A high sensitivity of ignition delay to inevitable small temperature fluctuations inside the cylinder was observed [80]. Moreover, it was found that the propagation regime

mode of reacting fronts is controlled by the magnitude of temperature fluctuation gradients [157]. HCCI was further studied in presence of turbulence (although decaying conditions) and regime modes were identified such that spontaneous ignition was favored as temperature gradients were dissipated [13, 64, 82]. Note that this is a transient ignition problem where the flow residence time is uniform and gradients in ignition delay are due to temperature gradients.

Sequential burner heavy-duty gas turbines perform under statistically steady autoignitive conditions with reheat system employed [67, 87, 199]. Combustion in these systems consists of two stages. In the first combustor, a lean premixed mixture is burnt keeping the temperature relatively lower, while in the reheat combustor, more fuel is injected in the hot products of the first-stage, resulting in a fast combustion. This method reduces emissions as both stages limit NO_x production, the first stage by ensuring low products temperature, and the second stage by having low reactive mixture residence time. Similar to HCCI systems, studies on gas-turbine reheat combustion also show spontaneous ignition and deflagration take part in the flame stabilization [2, 55, 65, 162, 169].

Aditya *et al.* [2] studied the problem of flame stabilization in reheat systems under autoignitive conditions in a simple model combustor. DNS of turbulent lean hydrogen-vitiated air combustion showed that combustion occurs due to both autoignition and deflagration modes. First, it was shown that autoignition plays a dominant role in fuel consumption along the centerline of the combustion chamber duct. Deflagrations were seen where the unburnt temperature was reduced, mainly near the corners of the expansion. Second, upstream of the expansion area, intermittent ignition was seen in the mixing duct which results in uncertainty in the identification of the flame position. This was suggested to be due to the extremely high temperature sensitivity of the ignition delay for the corresponding fully premixed hydrogen-air mixtures. The former, more stable behavior is favored in engine applications. This is because the latter behavior gives an off-design ignition timing due to early autoignition of the highly reactive spots in the mixture (*i.e.*, spots with low ignition delay). Avoiding intermittent ignition, and in general, controlling the ignition timing of this type of engines remains a challenge.

Ebi *et al.* [55] performed an experimental study on the transient flame stabilization of natural gas in the second-stage of a lab-scale sequential combustor at atmospheric pressure. High-speed OH-PLIF as well as OH chemiluminescence imaging were employed to observe the stable flame in the second stage of the combustor. It was shown that both spontaneous ignition and deflagration control the stabilization of fuel and vitiated air mixture combustion with spontaneous ignition becoming dominant upon increasing the

mixing temperature (decreasing the dilution air flow rate) downstream of the first stage. The flame structure and the ignition process varied depending on the regime mode. In spontaneous ignition mode the ignition showed a stable behavior, favoring the applicable design of these combustors. This is while at propagating conditions, the kernels formed more randomly, causing inconsistency in ignition delay predictions. Note that this observation is in contrast with the findings in the study described in the previous paragraph, although not in contradiction. There are two main differences that may have caused variance in the findings. First, the former study was simulated numerically and the mixture was designed to be well mixed in a mixing duct prior to injection, while in this study, an experimental investigation was provided with fuel and air being only partially mixed. Second, in the previous case, hydrogen fuel was considered which was mentioned to have high temperature sensitivity of the ignition delay, causing the unsteady ignition behaviour, as opposed to this study where natural gas has been used.

In a recent study, Savard *et al.* [162] addressed the problem of turbulence-chemistry interaction in a hydrogen-vitiated air mixture at reheat combustion conditions by performing DNS of premixed turbulent flames in a canonical inflow-outflow configuration. A theoretical model for the transition between spontaneous ignition and deflagration based on inflow velocity and turbulent Reynolds number was derived as follows. Assuming having an initial spontaneous ignition front, remaining time to ignition is defined as

$$\tau_{\text{ign}}(\boldsymbol{x}, t) = \tau - r(\boldsymbol{x}, t), \tag{2.23}$$

where τ is the ignition delay of the mixture at the beginning of the simulation (reactive mixture injection), and r is the residence time of the reactive mixture. Note that the configuration is defined such that the flow residence time is zero at the inlet upstream of the flame. Assuming a homogeneous mixture (*i.e.*, $\nabla\tau = 0$) in Eq. 2.23 and considering the Zeldovich criterion from Eq. 2.11, a transition to deflagration should be seen as

$$|\nabla r| S_L > 1. \tag{2.24}$$

To extend this inequality to capture turbulent flames, Eq. 2.25 in a mean form is described as

$$\langle |\nabla r| | r = \tau \rangle S_L > 1, \tag{2.25}$$

where $\langle . \rangle$ is an ensemble average. Using the decomposition $r = \langle r \rangle + r'$, and assuming uniform density, an equation is derived as

$$\nabla r = \frac{1}{U_{\text{in}}} \boldsymbol{e}_x + \nabla r', \tag{2.26}$$

where $\boldsymbol{e}_x$ is the unit vector parallel to the inlet bulk flow (U_{in}). It results that

$$\langle |\nabla r|^2 | r = \tau \rangle = \frac{1}{U_{\text{in}}^2} + \langle |\nabla r'|^2 | r = \tau \rangle. \tag{2.27}$$

Assuming residence time diffuses like a scalar (*i.e.*, the fluid age concept can be used [173, 174]), transport equations for r and r' are written as

$$\frac{\partial r}{\partial t} + \boldsymbol{u}.\nabla r = \frac{1}{\rho} \nabla.(\rho D \nabla r) + 1, \tag{2.28}$$

$$\frac{\partial r'}{\partial t} + \boldsymbol{u}.\nabla r' = \frac{1}{\rho} \nabla.(\rho D \nabla r'), \tag{2.29}$$

where D is the diffusivity. With the assumption of uniform density, r' behaves as a passive scalar in a mean scalar gradient (MSG) flow. Following the assumption of homogeneous isotropic turbulence (HIT) [123],

$$\langle |\nabla r'|^2 | r = \tau \rangle = \frac{1}{2D} \langle \chi_{r'} | r = \tau \rangle \approx \frac{1}{2D} \langle \chi_{r'} \rangle, \tag{2.30}$$

where $\chi_{r'}$ is the dissipation rate of the fluctuating component of the residence time. Considering MSG-HIT flow, $\chi_{r'}$ is equal to the evolution of the steady-state scalar variance which is approximated by the statistical results from Pope [142] (with $Re_t \sim \mathcal{O}(10)$–$\mathcal{O}(1000)$) as

$$\langle \chi_{r'} \rangle = -\frac{\langle u r' \rangle}{U_{\text{in}}} \approx \frac{u' l}{U_{\text{in}}^2}. \tag{2.31}$$

Combining Eqs. 2.25, 2.27, 2.30, 2.31 an approximate semi-analytical transition function was derived as

$$\frac{U_{\text{in,trans}}}{S_L} = 1 + a Re_t^{1/2}, \tag{2.32}$$

where a is a constant expected to depend on thermochemical conditions and $U_{\text{in,trans}}\,(Re_t)$ is the inflow velocity at which transition is expected at a given turbulent Reynolds number (deflagration if $U_{\text{in}} < U_{\text{in,trans}}\,(Re_t)$ and spontaneous ignition if $U_{\text{in}} > U_{\text{in,trans}}\,(Re_t)$).

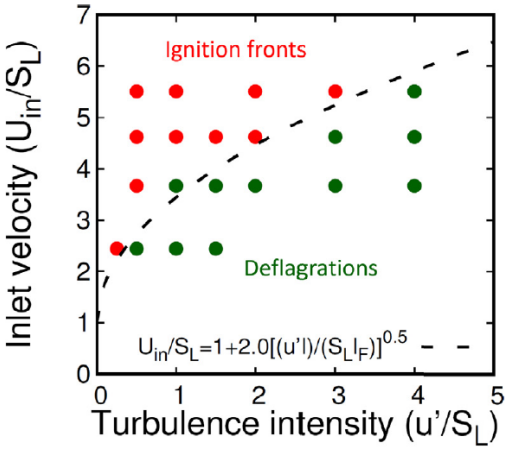

(a) Regime diagram with respect to the normalized inflow velocity and turbulence intensity.

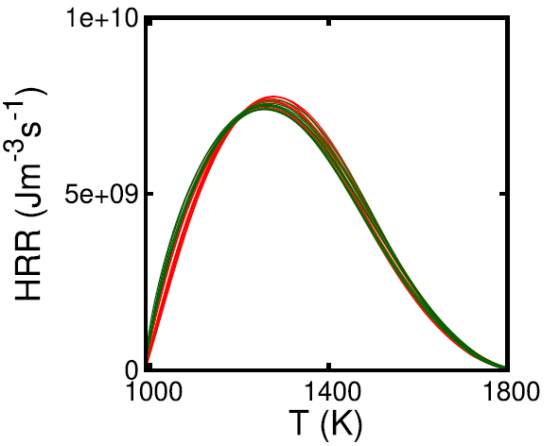

(b) Conditional mean HRR *vs.* temperature.

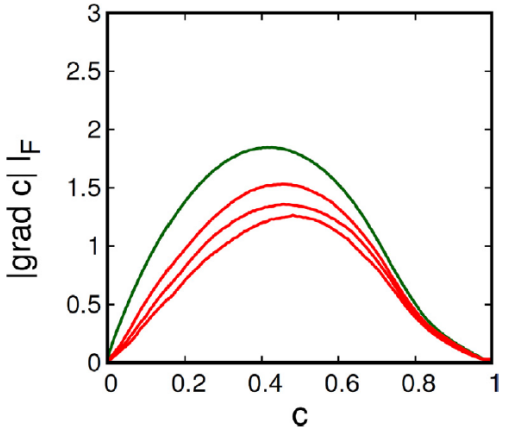

(c) Conditional mean magnitude of progress variable gradient $|\nabla c|$ *vs.* progress variable.

FIGURE 2.7: Turbulent premixed autoignitive hydrogen-vitiated air flame stabilization regimes and structure added from [162] depicting (a) the propagation regime diagram, (b) conditional mean of HRR with respect to temperature, (c) conditional mean of the magnitude of progress variable gradient in progress variable space. The progress variable used is a normalized H_2O mass fraction. Red denotes spontaneous ignition and green indicates deflagration.

This transition function is extended to both LTC and HTC in the present conditions in Section 4.2.

Flame stabilization and structure results are added from this paper in Fig. 2.7. Accordingly, Fig. 2.7a shows the regime diagram delimited by the identified transition function ($a = 0.24$, with $0.24Re_t^{1/2} = 2.0\left[(u'l)\,/\,(S_L l_F)\right]^{1/2}$). It is evident that inflow velocity and turbulence both contribute in the transition, while turbulence could solely trigger the transition from spontaneous ignition to a deflagration.

Following that the effect of transition was studied on the flame structure shown in Fig. 2.7b. This was a simple case of hydrogen fuel, and the flame structure in phase

space was only weakly altered with a very limited influence from regime transition on the flame structure. This is while in contrast, cool turbulent and laminar *n*-heptane/air flames [164] as well as very rich turbulent and laminar *n*-dodecane flames [161] showed considerable influence.

To further elucidate the transition mechanism, a gradient analysis shown in Fig. 2.7c was conducted. According to this figure, the mechanism responsible for transition was found to be the increase of mean magnitude of progress variable gradient at the reaction zone, which is triggered by added turbulence. In the present thesis, this phenomenon is clarified by expanding the aforementioned proposed model to identify transition at Spray A flame conditions, with the added complexity of LTC.

In another recent study, Gruber *et al.* [65] performed DNS for both laminar and turbulent hydrogen-vitiated air premixed flames at autoignitive conditions (adiabatic and non-adiabatic) and in a canonical configuration. Note that compressibility effects were enabled as part of the simulation setup to model the flames. First, laminar simulations of spontaneous ignition flames were investigated. It was found that the steadiness of these flames is strongly affected by the equivalence ratio as well as the premixed mixture temperature, where instabilities emerge from the variation of the unburnt mixture temperature. Furthermore, these effects were expressed analytically to characterize the unsteady ignition of the reaction front for both laminar and turbulent (1D, 2D and 3D) simulations. Second, the effect of turbulence was studied on the flame front velocity and its sustainability at autoignitive conditions. Self-excited instabilities were seen in turbulent hydrogen–air flames at atmospheric pressure. Additionally, an increase in the flame front reactivity with increasing turbulence intensity was encountered, caused by diffusion of hydrogen radicals and heat to the reactants. This induced a transition from spontaneous ignition fronts to propagating deflagration regimes. Note that all 3D turbulent flames in this study were deflagrations. Ultimately, a threshold was identified for the inflow velocity in the robust hydrogen-air ignition to ensure stabilization and applicability of this system.

In HCCI combustion, turbulence dissipates thermal stratification and favours spontaneous ignition, while in contrast, in premixed reheat systems this picture is altered such that deflagrations are encountered in higher turbulence environments. Here, the effects of turbulence are addressed in a fully premixed combustion system in the presence of mean residence time gradient but under CIE diesel conditions. Although all the aforementioned studies provided detailed insight into turbulent autoignitive flames, our understanding of the role of turbulence on the ignition, stabilization and structure remains

limited as only simple fuels under idealized conditions (*i.e.*, low pressure) have been considered.

Chapter 3

Methods

This chapter is organized as follows: 1) introduction to the governing equations, 2) numerical approach and the chemical mechanism, 3) thermochemical properties and laminar reference flames, 4) turbulent flow configuration, and 5) simulation parameter setup for the turbulent flames.

Author's contribution: The laminar flame simulations presented in this section are all performed by the author. In addition, similar simulations, but performed with a different chemical kinetics mechanism were also performed by the author (not shown) and contributed to a co-authored article published in Combustion and Flame (Savard *et al.* [166]). Finally, the author contributed to the design of the turbulent flame setup and parameters and performed all turbulent flame simulations.

3.1 Governing equations

Governing equations describing the dynamics of low-Mach unsteady chemically reacting flows, subject to turbulence forcing (to maintain the desired level of turbulence intensity), are presented in this section. The reacting mixture is composed of N species.

The continuity and conservation of momentum equations read:

$$\frac{\partial \rho}{\partial t} + \nabla.(\rho \boldsymbol{u}) = 0, \tag{3.1}$$

$$\frac{\partial(\rho \boldsymbol{u})}{\partial t} + \nabla.(\rho \boldsymbol{u} \otimes \boldsymbol{u}) = -\nabla p + \nabla \cdot \boldsymbol{\sigma} + \rho \boldsymbol{f}, \tag{3.2}$$

where ρ is the mixture density, $\boldsymbol{u}$ is the velocity vector, p is the hydrodynamic pressure, and $\boldsymbol{\sigma}$ is the viscous stress tensor given by

$$\boldsymbol{\sigma} = 2\mu \left[\boldsymbol{S} - \frac{1}{3}(\nabla \cdot \boldsymbol{u})\boldsymbol{I} \right]. \tag{3.3}$$

$\boldsymbol{S} \equiv 1/2\left(\nabla \boldsymbol{u} + (\nabla \boldsymbol{u})^{\intercal}\right)$ is the strain rate tensor, $\boldsymbol{I}$ as the identity matrix, and μ is the mixture dynamic viscosity.

To simulate high Ka flames in the absence of mean shear, a velocity forcing term, $\boldsymbol{f}$ is appended to the momentum equation to maintain the desired turbulence intensity across the simulation domain (the configuration is introduced in Section 3.4.1). The linear velocity forcing method is used [25, 109, 153] and the implementation follows that of Savard *et al.* [159].

The temperature equation is given by:

$$\frac{\partial \rho T}{\partial t} + \nabla \cdot (\rho \boldsymbol{u} T) = \nabla \cdot (\rho \alpha \nabla T) + \dot{\omega}_T - \frac{1}{c_p} \sum_{i=1}^{N} c_{p,i} \boldsymbol{j}_i \cdot \nabla T + \frac{\rho \alpha}{c_p} \nabla c_p \cdot \nabla T, \tag{3.4}$$

where temperature is denoted by T, c_p is the mixture specific heat at constant pressure, $\alpha = \lambda/(\rho c_p)$ is the thermal diffusivity, with λ the thermal conductivity, $\dot{\omega}_T$ is the chemical production rate (heat release rate divided by c_p), and $c_{p,i}$ is the specific heat at constant pressure of the ith species. Moreover, $\boldsymbol{j}_i$ is the species diffusion flux described as

$$\boldsymbol{j}_i = -\rho D_{i,m} \frac{Y_i}{X_i} \nabla X_i - \rho Y_i \boldsymbol{u}_c, \tag{3.5}$$

where X_i is the ith species mole fraction and Y_i its mass fraction. $D_{i,m}$ is the mixture-averaged species diffusion coefficient and is defined as follows:

$$D_{i,m} = \frac{1 - Y_i}{\sum_{j \neq i} \frac{X_j}{\mathcal{D}_{ij}}}, \tag{3.6}$$

with $\mathcal{D}_{ij}$ the ordinary multi component diffusion coefficient of the jth species relative to the ith species. Note that Soret/Dufour diffusion is neglected. Some reference laminar flame cases in this thesis are simulated using the unity Lewis number assumption, *i.e.*,

the species diffusivity is instead computed as

$$D_{i,m} = \frac{\alpha}{Le_i}, \tag{3.7}$$

with Le_i the species Lewis number assumed equal to unity.

Next, species conservation leads to the following transport equation for the ith species:

$$\frac{\partial \rho Y_i}{\partial t} + \nabla \cdot (\rho \boldsymbol{u} Y_i) = -\nabla \cdot \boldsymbol{j}_i + \dot{\omega}_i. \tag{3.8}$$

To describe the chemical model, $\dot{\omega}_i$ is implemented in Eq. 3.8 as the net chemical production rate of the ith species expressed as a function of the production term, $\dot{\omega}_{i,p}$ and the consumption term, $\dot{\omega}_{i,c}$, as

$$\dot{\omega}_i = \dot{\omega}_{i,p} - \dot{\omega}_{i,c}, \tag{3.9}$$

with

$$\dot{\omega}_{i,p} = W_i \sum_{j=1}^{K} \left[k_j \prod_{s=1}^{N} \left(\frac{\rho Y_s}{W_s} \right)^{\nu_{js}} \right], \nu_{js} > 0, \tag{3.10}$$

$$\dot{\omega}_{i,c} = W_i \sum_{j=1}^{K} \left[k_j \prod_{s=1}^{N} \left(\frac{\rho Y_s}{W_s} \right)^{-\nu_{js}} \right], \nu_{js} < 0, \tag{3.11}$$

with W_i the molecular weight of species i, ν_{js} the stoichiometric coefficient of species s in reaction j, and the constant k_j is given by

$$k_j(T) = A_j T^{b_j} e^{-T_{aj}/T}, \tag{3.12}$$

where A_j is the pre-exponential factor, b_j is the temperature exponent, and T_{aj} is the activation temperature of the jth reaction. Moreover, $\dot{\omega}_T$ employed in Eq. 3.4 is defined as

$$\dot{\omega}_T = -\sum_{j=1}^{N} h_i \dot{\omega}_i, \tag{3.13}$$

with h_i the specific enthalpy of the ith species, given as

$$h_i = h_i^0 + \int_{T_0}^{T} c_{p,i} dT, \tag{3.14}$$

with h_i^0 its value at standard temperature T_0.

The equation of state for a mixture of ideal gases, is

$$P_0 = \frac{\rho R_u T}{W}, \tag{3.15}$$

where P_0 is the thermodynamic pressure, uncoupled from the hydrodynamic pressure under the low-Mach assumption, with the pressure given by $P(\boldsymbol{x}, t) = P_0(t) + p(\boldsymbol{x}, t)$. Note that in this setup, the background pressure P_0 is constant. R_u is the universal gas constant and W is the mixture molecular weight given by

$$W = \left(\sum_{i=1}^{N} \frac{Y_i}{W_i} \right)^{-1}. \tag{3.16}$$

3.2 Numerical approach

In this study, the equations introduced in the previous section are resolved numerically using a DNS approach previously executed in [160, 164]. The numerical approach employs the energy conservative, finite difference code NGA [45]. The numerical scheme used is second-order accurate in space and time [167]. The third-order bounded QUICK scheme, BQUICK, is used for the scalar transport equations [73]. A semi-implicit Crank-Nicolson time integration is used [137, 167].

The mechanism for *n*-dodecane oxidation is described by a chemical kinetics system with 35 species [20], reduced from the skeletal mechanism with 53 species and 269 reactions due to Yao *et al.* [200]. The mechanism contains high-temperature and semi-global low-temperature chemistry pathways, optimized for diesel engine conditions. Mixture-averaged diffusivity is used for species transport, and the mixture viscosity, and thermal diffusivity are computed as in [167].

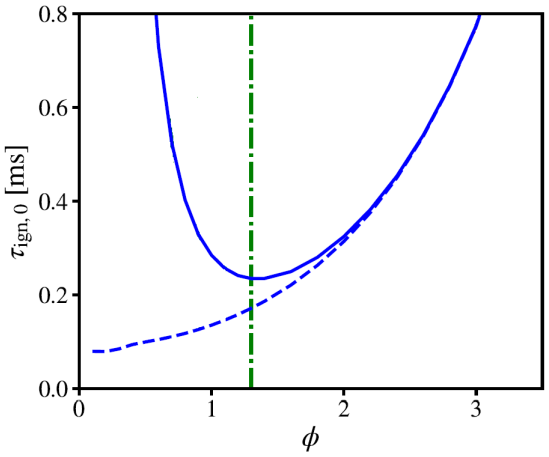

FIGURE 3.1: Ignition delay obtained from constant-pressure homogeneous reactor *vs.* equivalence ratio for *n*-dodecane-oxidizer mixtures along the mixing line at Spray A conditions. Solid blue line: HTC ignition delay. Dotted blue line: LTC ignition delay. Dash-dotted vertical lines: equivalence ratios used in the present study.

3.3 Thermochemical conditions and reference laminar flames

The thermochemical conditions are chosen to match those of the most reactive mixture in the Engine Combustion Network's baseline *n*-dodecane Spray A flame. Figure 3.1, modified from [166] shows the ignition delay along the mixing line of the Spray A flame with 15% volume of O_2, temperature of 900 K in the ambient gas (oxidizer side) and gaseous *n*-dodecane with the same enthalpy as liquid *n*-dodecane at 363 K on the fuel side, with a pressure of 60 atm. In these conditions, the most reactive mixture (*i.e.*, lowest second-stage ignition delay) is characterized by an equivalence ratio of 1.3 (with corresponding unburnt temperature of 812.7 K) which exhibits two distinct ignition stages. This mixture is adopted in this study to elucidate the two-stage ignition characteristics of *n*-dodecane-oxidizer mixture while having a pre-dominant influence on Spray ignition and flame stabilization. The variation of Spray A with 21% O_2 in the ambient will be considered for a few cases.

The approach taken to identify the flame reference speed is described by Krisman *et al.* [95]. Figure 3.2a presents the steady-state flame lift-off position L_f (based on the location of maximum heat release rate (HRR) during the first and the second stages) as a function of inlet velocity U_{in} for both unity Lewis number and mixture-averaged (non-unity Lewis numbers) transport models. Figure 3.2b presents the derivative of L_f with respect to U_{in}, as a function of U_{in}. As proposed by Krisman *et al.*, in the diagram of the derivative $\mathrm{d}L_f/\mathrm{d}U_{\mathrm{in}}$ *vs.* U_{in}, the inlet velocity at which the peak in $\mathrm{d}L_f/\mathrm{d}U_{\mathrm{in}}$

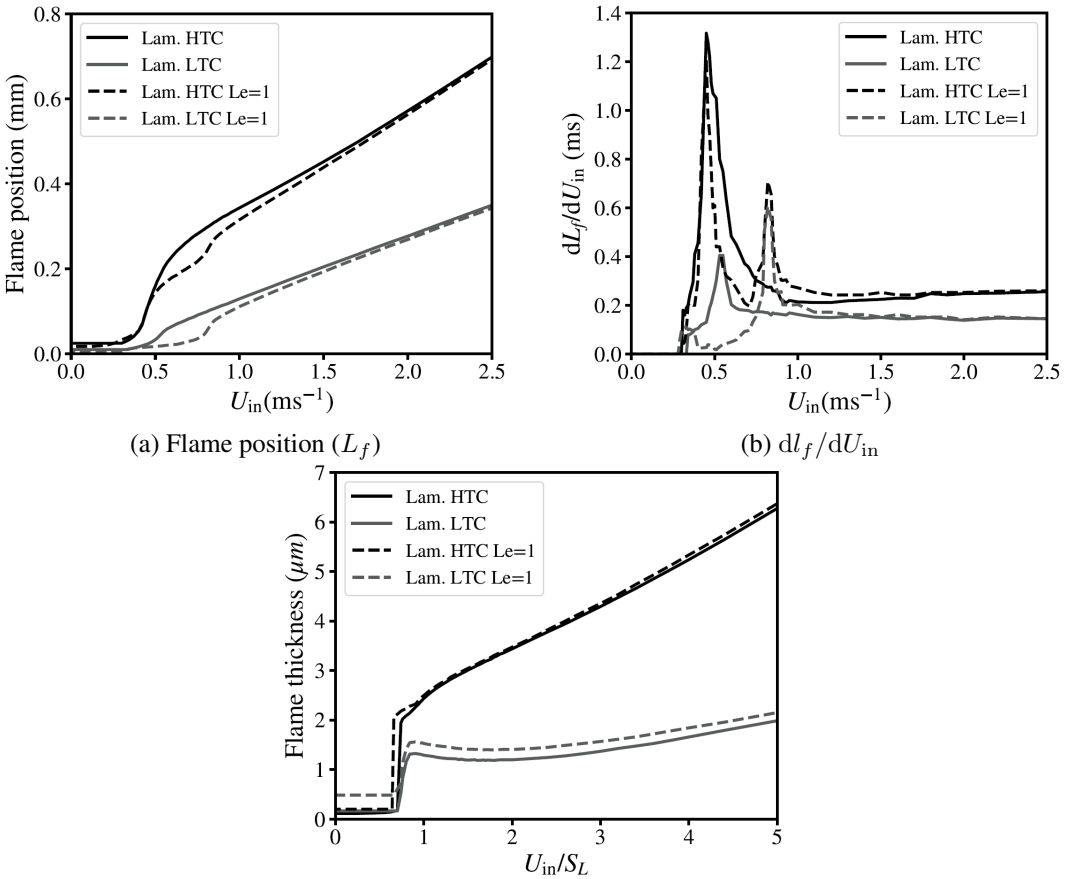

(a) Flame position (L_f)

(b) $\text{d}l_f/\text{d}U_{\text{in}}$

(c) Flame thickness (l_F)

FIGURE 3.2: (a) First and second-stage flame position for both unity and non-unity Lewis number conditions with respect to the inflow velocity under laminar conditions. (b) Flame position derivative with respect to U_{in} *vs.* U_{in}. (c) First and second-stage flame thickness for both unity and non-unity Lewis number conditions, with respect to the normalized inflow velocity under laminar conditions.

occurs corresponds to the laminar flame speed S_L. Note that the cool and hot flame speeds are approximately equal for the present mixture. Accordingly, the expected intrinsic deflagration speed can be verified from Fig. 3.2b. By referring to this figure, the reference speed for unity Lewis number flames can be verified as approximately $S_L = 0.5$ m/s, the same as the non-unity Lewis number flames. Additionally, non-unity Lewis number laminar flame speed for LTC has the same value, while the unity Lewis number flame speed for LTC has a value of 0.8 m/s. The laminar flame thickness l_F (based on maximum thermal gradient) is evaluated and depicted in Fig. 3.2c as a function of normalized U_{in}. Generally, both cool and hot flames get thicker upon increasing the inlet velocity, with the larger slope attributed to the hot flames. Note that for LTC, the flame thickness during $0.8 < U_{\text{in}}/S_L < 1.8$ drops slightly before rising back up again.

The difference in slope between LTC and HTC for large U_{in} in Fig. 3.2a and 3.2c is

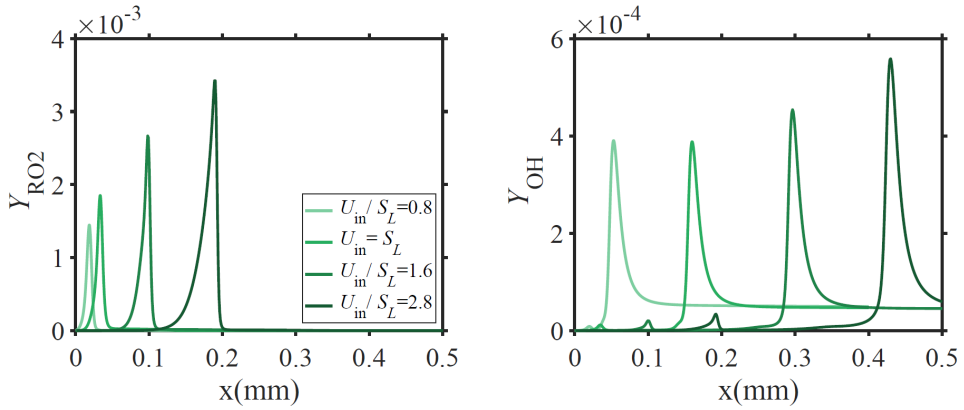

(a) Y_{RO_2} in physical space.

(b) Y_{OH} in physical space.

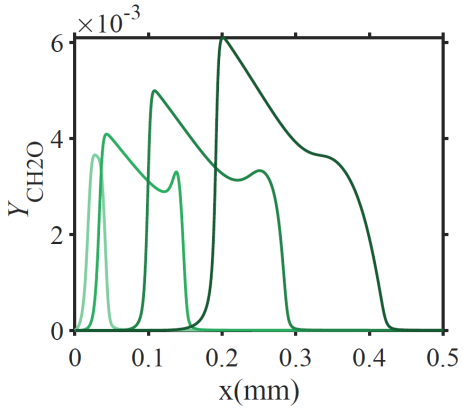

(c) Y_{CH_2O} in physical space.

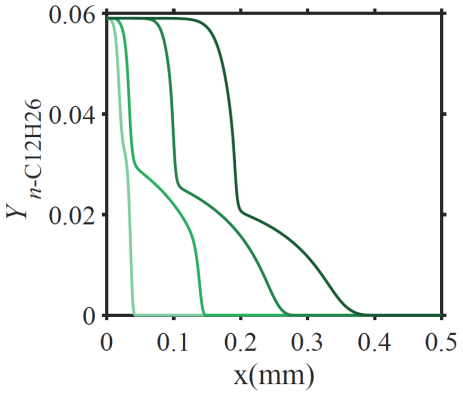

(d) $Y_{n-C_{12}H_{26}}$ in physical space.

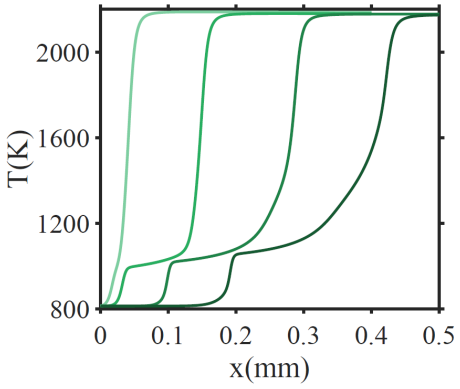

(e) Temperature in physical space space.

FIGURE 3.3: Laminar flame structure in physical space for (a) mass fraction of RO_2, (b) mass fraction of OH, (c) mass fraction of formaldehyde, (d) fuel mass fraction, and (e) temperature.

attributed to gas expansion across the cool flame. As fluid elements go through the cool flame, they accelerate due to mass conservation and the decrease in density.

The double-stage structure of the current flames in physical space is provided in Fig. 3.3, showing four laminar cases with different inflow velocities spanning from deflagrations

to spontaneous ignition fronts. Note that cases with $U_{\text{in}} < S_L$ are deflagrations, and $U_{\text{in}} > S_L$ are spontaneous ignition fronts.

3.4 Turbulent flames setup

3.4.1 Flow configuration

The computational domain consists of a rectangular duct of length L_x and square cross section of width $L_y = L_z = L$, with $L_x > L$ (see Table 3.1). Inflow-outflow boundary conditions are imposed in the streamwise direction (x-direction), with periodic boundary conditions imposed in both the y- and z-directions.

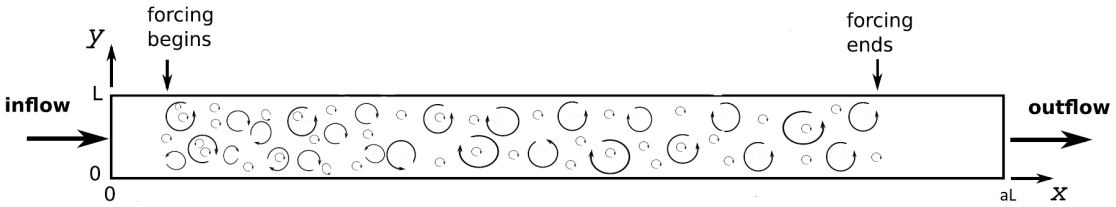

FIGURE 3.4: Canonical configuration of the turbulent flame simulations in presence of the turbulence forcing (prior to reactive mixture (fuel/air) injection).

The flow is initialized with a non-reactive oxygen-nitrogen mixture, with the inflow boundary conditions taken from a separate homogeneous isotropic turbulence simulation with linear forcing. The simulation is run until the convected (and forced) turbulent flow field is well developed. The configuration setup corresponding to the turbulent simulations is depicted in Fig. 3.4 showing the initial turbulent flow field prior to fuel/air injection. At the far left side of the domain, the unburnt mixture is injected at constant bulk velocity. Turbulent kinetic energy (TKE) is low (forcing magnitude is 0) at both ends of the domain to avoid negative inlet velocities. Away from inlet and outlet regions (at about $0.5L$), turbulence is forced (forcing magnitude is increased to produce the desired Re_t) to maintain a constant TKE across the flame. After turbulence is fully developed in the domain, at the beginning of the simulation, the reactive fuel-air mixture (*n*-dodecane-oxygen-nitrogen) is injected at the inlet with the velocity boundary conditions unchanged (time-varying turbulent flow field). The simulation is further run for an adequate amount of time, well beyond the occurrence of ignition, until a statistically steady state is reached. Data is acquired from the start of the reactive mixture injection,

which corresponds to the zero residence time. Note that a similar initialization procedure was adopted for the laminar simulations presented in Section 3.3. This allows systematic comparison of ignition delays between laminar and turbulent configurations. As the turbulence naturally decays in the present configuration, turbulent kinetic energy is maintained via the linear velocity forcing method described in [159, 163].

3.4.2 Simulation parameters

The simulations are set up in order to span both spontaneous ignition and deflagration regimes. Based on the work of Savard *et al.* [162], it is expected that sufficiently high inflow velocity with low turbulent Reynolds number would lead to a turbulent spontaneous ignition front for both cool and hot flames, while higher Re_t with sufficiently low inflow velocity would lead to both cool and hot flames propagating upstream in a deflagrative mode, and eventually attaching themselves to the inlet. Consequently, in this section, a parametric sweep is designed to span the two regimes by altering inflow velocity, U_{in}, Reynolds number, ambient oxygen percentage, and integral length scale, l. The effects of these parameters are later shown on flame ignition, stabilization, and structure. Details of the physical and numerical parameters for a total of 19 turbulent cases are presented in Table 3.1. Inflow velocities span from $U_{\mathrm{in}}/S_L = 4$ to $U_{\mathrm{in}}/S_L = 16$, and Reynolds numbers vary from $Re_t = 50$ to $Re_t = 220$. Two cases with larger integral length scale are considered ($l/l_F = 2$) to elucidate the effects of integral length scale in current conditions. Additionally, to assess the effect of oxygen level on the flame reactivity and stabilization, three cases with $\mathrm{O}_2 = 21\%$ are considered. The parameters utilized in Table 3.1 are defined in Section 2.4 and are set to expand across the regime diagram shown in Fig. 2.6. Re_t, Ka_{u}, and Da are expressed as in 2.17, 2.18, and 2.19, respectively. Eddy turnover time $\tau_{t,o}$ is defined as 2.13. Moreover, τ is the second-stage ignition delay in a constant pressure homogeneous reactor, and t_{end} is the total simulation time. Note that intermittent ignition was seen in some cases, therefore, simulation time is relatively long (between 3 to 6 ignition delays), to make sure a statistically-steady state is reached. The streamwise domain length is selected based on the magnitude of inflow velocity to ensure both LTC and HTC reaction zones fall within the domain.

A uniform grid spacing of at most 1 micron is maintained to ensure a minimum of 10 grid points across the thinnest reactive species layers [37, 166]. For case 4, with

Case	l/l_F	$\%O_2$	U_{in}/S_L	u'/S_L	Ka_{u}	Re_t	Da	$t_{\text{end}}/\tau_{t,o}$	t_{end}/τ	L_x/L_y	$\text{N}_x \times \text{N}_y \times \text{N}_z$
1	1	15	4	5	39	50	0.036	182	7.3	6.4	$832 \times 130 \times 130$
2	1	15	4	13	142	120	0.016	388	6.6	6.4	$832 \times 130 \times 130$
3	1	15	4	18	269	180	0.010	658	7.3	6.4	$832 \times 130 \times 130$
4	1	15	6	24	351	220	0.008	346	3.2	10.0	$1680 \times 168 \times 168$
5	1	15	7	5	39	50	0.036	124	5	11.2	$1456 \times 130 \times 130$
6	1	15	7	13	142	120	0.016	260	4	11.2	$1456 \times 130 \times 130$
7	1	15	7	18	269	180	0.010	428	4.8	11.2	$1456 \times 130 \times 130$
8	1	15	10	5	39	50	0.036	107	4.3	16.0	$2080 \times 130 \times 130$
9	1	15	10	13	142	120	0.016	216	3.7	16.0	$2080 \times 130 \times 130$
10	1	15	10	18	269	180	0.010	349	3.9	16.0	$2080 \times 130 \times 130$
11	1	15	13	13	142	120	0.016	198	3.4	20.8	$2704 \times 130 \times 130$
12	1	15	13	18	269	180	0.010	317	3.5	20.8	$2704 \times 130 \times 130$
13	1	15	16	5	39	50	0.036	122	4.9	25.6	$3328 \times 130 \times 130$
14	1	15	16	18	269	180	0.010	372	4.2	25.6	$3328 \times 130 \times 130$
15	2	15	13	9	62	180	0.040	43	1.95	10.4	$2704 \times 260 \times 260$
16	2	15	16	9	62	180	0.040	36	1.7	16.0	$4160 \times 260 \times 260$
17	1	21	13	13	142	120	0.016	130	2.2	11.2	$1456 \times 130 \times 130$
18	1	21	13	13	142	120	0.016	197	3.3	16.0	$2080 \times 130 \times 130$
19	1	21	13	13	142	120	0.016	223	3.8	20.8	$2704 \times 130 \times 130$

TABLE 3.1: Turbulent simulation parameters.

the largest Reynolds number, the grid spacing is constrained by the resolution of all turbulence length scales.

All laminar and turbulent flame simulations were ran on Niagara using Compute Canada resources, amounting to approximately 5.4 million CPU-hours. The total simulation cost is relatively high due to simulating various turbulent cases with high Ka where a total of 1 billion grid points were used. Highest simulation cost was attributed to the two cases with large integral length scale ($l/l_F = 2$), totaling 460 million grid points across the flame domain. Moreover, simulation times up to 650 turnover times (or 6.6 times the 0D ignition delay) per simulation were used to achieve statistically steady solution for the purpose of post-processing and flame stabilization analysis.

Chapter 4

Results and discussion

Turbulent flame results are presented in this chapter. A qualitative presentation of the time evolution of representative flames is presented in the first section. Then, the role of turbulence on the flame stabilization is discussed including regime classification. Next, an analysis of the flame ignition behavior is studied, followed by flame structure characterisation and regime transition modeling. Section 4.5 contains a chemical explosive mode analysis (CEMA) used to systemically support the conclusions of the previous sections. In all the above sections, only the cases corresponding to the Spray A baseline conditions (15% O_2 in the ambient gas) are considered. The effect of oxygen level in the ambient gas is presented in Section 4.6. Finally, a discussion on the generality of the results and modeling challenges/recommendations is provided.

Author's contribution: The author performed all the post-processing leading to the results presented here. This task involved parallel code development by the author. All figures were obtained by the author. Finally, the author significantly contributed to the analysis of the results.

4.1 Overview

Figures 4.1 and 4.2 present time sequences of contours of heat release rate (HRR) on 2D slices of selected turbulent flames. A logarithmic colour scale is used to simultaneously highlight both the LTC and HTC regions. HRR contour analysis is used mainly as it lays out information for both cool and hot flames, and provides insights into flame overall structure. The flow direction is from left to right. Time frames are chosen from

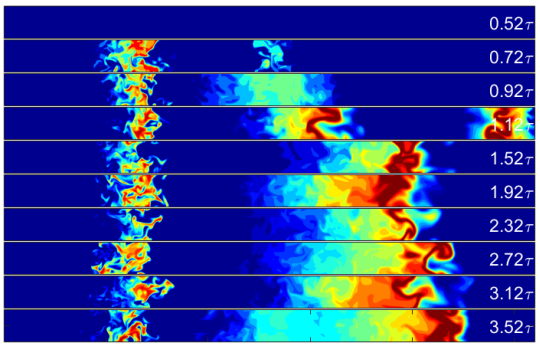

(a) $U_{\text{in}}/S_L = 10$, $Re_t = 50$.

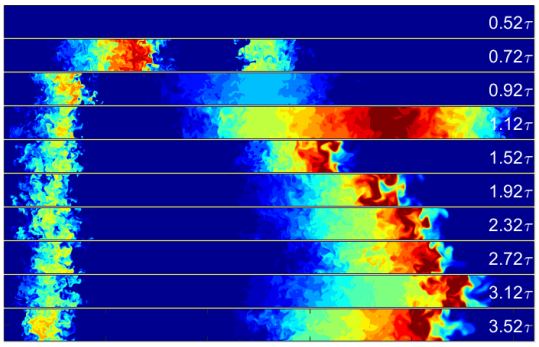

(b) $U_{\text{in}}/S_L = 10$, $Re_t = 180$.

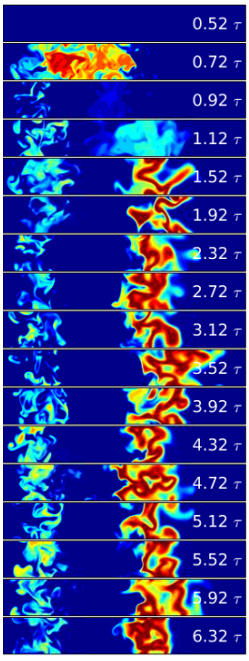

(c) $U_{\text{in}}/S_L = 4$, $Re_t = 50$.

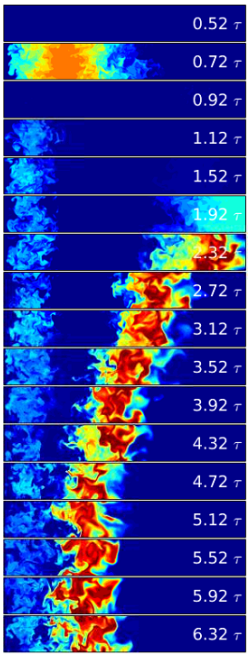

(d) $U_{\text{in}}/S_L = 4$, $Re_t = 180$.

(e) Color scale (logarithmic), ranging from 10 to 12.5 log(Jm$^{-3}s^{-1}$).

FIGURE 4.1: 2D HRR contours corresponding to (a) $Re_t = 50$, (b) $Re_t = 180$, for $U_{\text{in}}/S_L = 10$, and (c) $Re_t = 50$, (d) $Re_t = 180$, for $U_{\text{in}}/S_L = 4$. Numbers in white on the right side of the contours represent time where τ is the 0D ignition delay equal to 2.25×10^{-4} s. The first contour in each case corresponds to the half of 0D ignition delay (0.13 ms after injection), just prior to the first stage ignition delay.

just before first-stage ignition (at $\tau/1.7$, or 0.13 ms after injection) until a statistically steady state is reached. The HRR regions upstream of the domain correspond to LTC (cool flame), and the ones downstream are due to HTC (hot flame). Cases 1, 3, 8, and 10 from Table. 3.1 are selected and compared in Fig. 4.1. For all these cases, consistent with the 0D behavior, the cool flame ignites first, followed by HTC ignition. However,

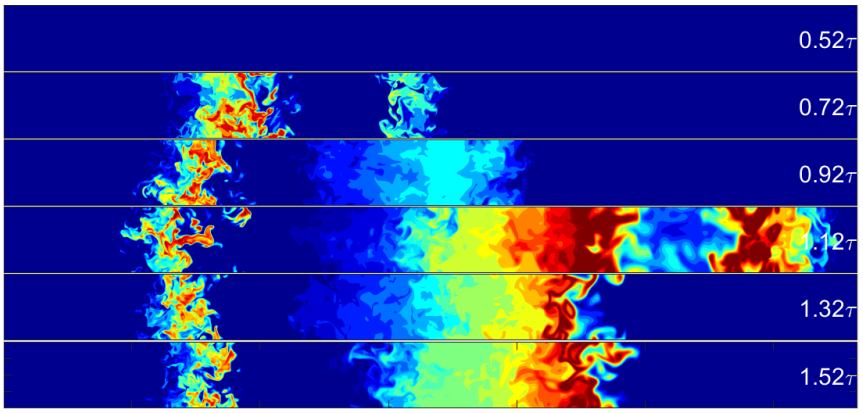

(a) $l/l_F = 2$, $U_{\text{in}}/S_L = 16$, $Re_t = 180$.

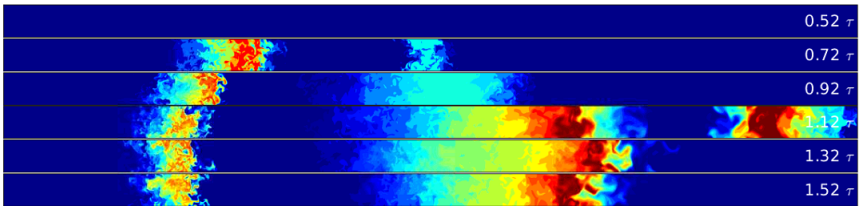

(b) $l/l_F = 1$, $U_{\text{in}}/S_L = 16$, $Re_t = 180$.

FIGURE 4.2: 2D HRR contours corresponding to (a) $l/l_F = 2$, (b) $l/l_F = 1$, with $U_{\text{in}}/S_L = 16$, $Re_t = 180$. Numbers in white on the right side of the contours represent time where τ is the 0D ignition delay equal to 2.25×10^{-4}. The first contour in each case corresponds to the half of 0D ignition delay (0.13 ms after injection), just prior to the first stage ignition delay.

the time elapsed between these two ignition stages varies greatly from case to case. A quantitative evaluation of ignition delay is presented in Section 4.3.

For case 1 (Fig. 4.1a) both cool and hot flames stabilize away from the inlet suggesting both are stabilized by spontaneous ignition, the respective propagation speeds matching the incoming bulk velocity. Compared to Fig. 4.1b we see that a sufficiently high turbulence intensity triggers the cool spontaneous ignition front to transition into a cool deflagration, causing it to move upstream towards the inlet. This is while the hot flame, still stabilized by spontaneous ignition, is pushed further downstream, effectively "splitting" the double cool-hot flame. As for case 3, illustrated in Fig. 4.1d, we observe that, at sufficiently low inflow velocity, in a highly turbulent environment, both cool and hot flames transition to deflagrations, propagating upstream and finally attaching to the inlet.

The observed remarkable "split" of the cool-hot double flame under the sole effect of turbulence has never been reported in the literature, to the best of the author's knowledge. The phenomenon can be explained using results from our recent work on laminar

flames under similar thermochemical conditions [166]. Under such conditions, as a cool spontaneous ignition front transitions to a deflagration, heat diffusion from the cool flame products affects the chemical pathways, leading to a reduced reactivity in its products, *i.e.*, an increase in HTC ignition delay. In the present case, as HTC is stabilized by spontaneous ignition, an increased ignition delay leads to the flame stabilizing further downstream. The chemical explosive mode analysis presented in Section 4.5 will provide further support to this explanation.

Cases 14 and 16, which have the same U_{in}/S_L and Re_t, but different integral length scales, are compared in Fig. 4.2. The ignition and stabilization behaviors are qualitatively similar between the two cases. Quantitative comparison will be presented in the next sections. The observation is consistent with the results of Savard *et al.* [162] obtained for (single-stage) hydrogen combustion. Note that both LTC and HTC reaction zones appear more distributed, or diffused, in the smaller integral length scale case. This is a result of the larger Karlovitz number at fixed Re_t.

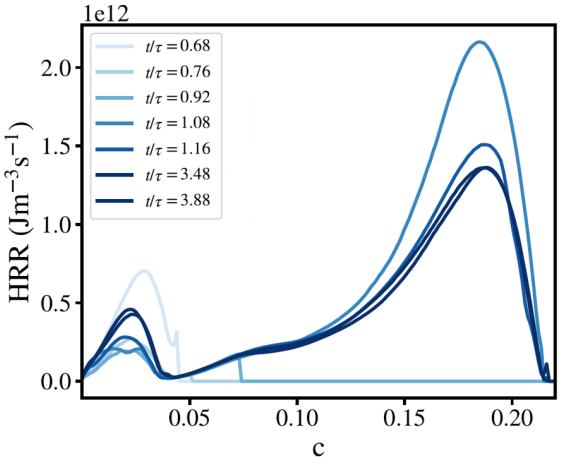

FIGURE 4.3: Flame evolution for case 8 from Table 3.1.

The HRR evolution in progress variable space, $c = Y_{\text{H}_2}+Y_{\text{H}_2\text{O}}+Y_{\text{CO}}+Y_{\text{CO}_2}$, is shown in Fig. 4.3 for case 8 ($U_{\text{in}}/S_L = 10$, $Re_t = 50$). The color scheme evolves to a darker color as simulation time increases. Each line is obtained from averaging HRR conditional on local values of progress variable, c. The first (second) peak at low (high) c values corresponds to the cool (hot) flame. Following first-stage ignition, we first see a drop in HRR magnitude in the cool flame region, followed by a smaller increase as the flame reaches steady-state. For the hot flame, we see a sudden increase as the second-stage ignition takes place, followed by a drop until the flame is stabilized in the steady-state regime.

4.2 Stabilization regime identification

To identify the propagation regime for each turbulent case, the time evolution of cool and hot flame positions is presented in Fig. 4.4. The LTC (HTC) flame position is based on the instantaneous position of maximum mass fraction of RO_2 (OH) in the domain.

For cool flames (Fig. 4.4a), the flame moves towards the inlet following first-stage ignition (initial transient period), before a steady-state flame position is reached, after approximately one to two τ. A clear separation in steady state lift off position between the red and the green/blue cases is apparent. For cases in green or blue, the cool flame propagates upstream until it attaches to the inlet, *i.e.*, its propagation speed is limited by the imposed boundary conditions at the inlet (refer to the contour sequence figures in Appendix A for visualization). For these cases, the cool flame is deemed to have transitioned to a deflagration. In contrast, for the cases in red, the cool flame reaches a statistically steady position far downstream from the inlet, suggesting that its stabilization is controlled by spontaneous ignition, the flame propagating exactly at the incoming bulk mixture velocity.

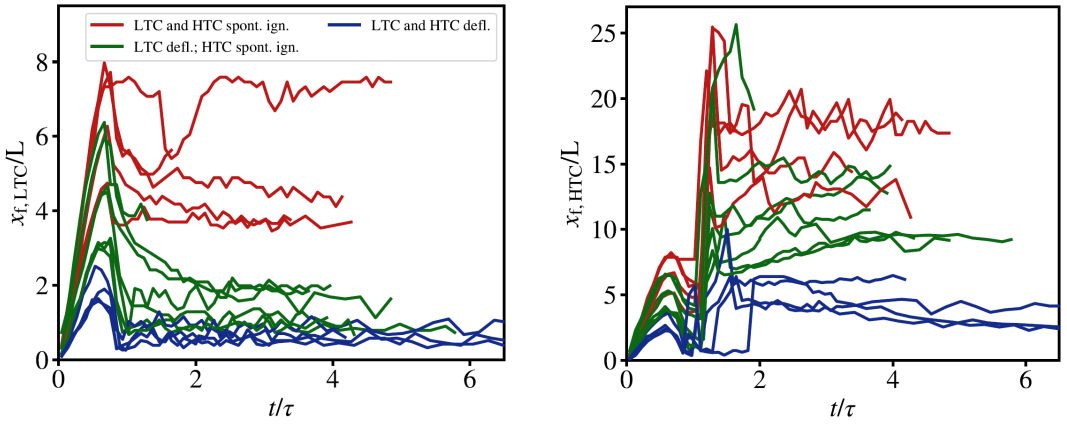

(a) LTC flame position

(b) HTC flame position

FIGURE 4.4: Cool and hot flame positions normalized by L. Red: LTC and HTC spontaneous ignition fronts; green: LTC spontaneous ignition front and HTC deflagration; blue: LTC and HTC deflagrations. The resolution in time is 2e-5 s, 1400 times larger than the timestep size.

Similarly, Fig. 4.4b shows the position of hot flames as a function of time. A difference in HTC steady state flame position between red/green and blue lines is readily identified. For cases in blue, the hot flame has transitioned to a deflagration, its propagation speed overcoming the bulk inflow velocity, while for cases in green and red, the hot flame is stabilised by spontaneous ignition. For the cases in green the flame moves downstream

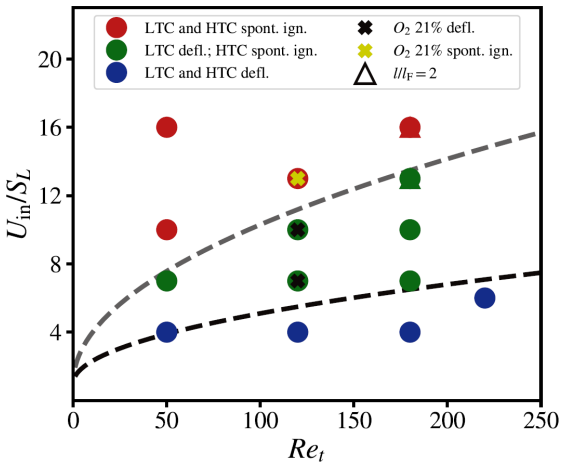

FIGURE 4.5: Flame stabilization with respect to the inflow velocity and Reynolds number. Red dots denote both first and second-stage spontaneous ignition; green dots correspond to first-stage deflagration, second-stage spontaneous ignition; blue dots refer to both first and second stage deflagration; red triangle shows the larger integral length scale case.

before reaching its steady state position. This is due to the reduced reactivity of cool deflagration products, as described in Section 4.1.

Note that the flame position for deflagrations does not exactly reach zero (inlet). This is attributed to the following reasons. First, turbulent flame brushes are thick under strong turbulence intensity (refer to Appendix A). Second, turbulence forcing starts at $x \approx L$, such that deflagrations reaching this region see their propagation speed reduced. The approach taken to identify the different regimes is consistent with that taken by Savard *et al.* [162] for hydrogen flames.

To gather statistics for the analysis of turbulent deflagrations, Savard *et al.* [162] considered the upstream propagation period preceding the steady state "attached" period. While this approach has the advantage of avoiding potential flame interaction with the inlet boundary, in the present cases, the upstream propagation period is too short to gather meaningful statistics. Hence, it is chosen to consider only the steady state period to conduct the analysis in this section. Nevertheless, it was verified, as shown in Appendix B, that heat loss to the inlet is negligible for all except one case (case 3).

With the stabilization regime identified for all cases, a diagram is constructed and shown in Fig. 4.5. Transition of the flame stabilization from spontaneous ignition to deflagration is encountered essentially by lowering the inflow velocity or sufficiently increasing the turbulent Reynolds number. In contrast, for large inflow velocity and small turbulence intensity, the flame stabilization is identified as spontaneous ignition, controlled

mostly by chemical reactions rather than diffusion. As discussed earlier, in particular flow conditions it was observed that the cool flame deflagrates and attaches to the inlet, while the hot flame is still burning as a spontaneous ignition front (green cases). The higher propensity of cool flames to deflagrate, in contrast with hot flames, is attributed to 1) the present thermochemical conditions (the laminar cool reference deflagration speed is the same as that of the hot flame, while it is larger with the unity Lewis number transport model[1]) and 2) the decrease in turbulent Reynolds number across the flame associated with the increase in kinematic viscosity.

In Fig. 4.5, two separate curves corresponding to the transition functions for LTC and HTC are included. Here, the same model described by [162] shown in Eq. 2.32 is employed to approximate the transition functions of the current two-staged ignition flames. Rewriting this equation we have

$$\frac{U_{\mathrm{in,trans}}}{S_{\mathrm{L}}} = 1 + aRe_t^{1/2}. \tag{4.1}$$

Here, the transition function is fitted to both the transitions to LTC deflagration and HTC deflagration separately. The value of a that provides the best fit is found to be 0.93 for LTC, and 0.41 for HTC transition functions, respectively.

4.3 Ignition

Figure 4.6 presents the ignition delays *vs.* transition function, with

$$\text{Transition function} = \frac{S_L}{U_{\mathrm{in}}}\left(1 + aRe_t^{1/2}\right), \tag{4.2}$$

with $a = 0.93$ for LTC and $a = 0.41$ for HTC (see previous section). If the transition function takes values greater (less) than unity, the flame is a deflagration (spontaneous ignition front). Turbulent flame results in Fig. 4.6 are compared to those obtained from laminar flame simulations with both the unity Lewis number and mixture-averaged transport models. First-stage ignition (LTC) is weakly affected across laminar and turbulent cases with just a minor increase with increasing LTC transition function over the range considered. In contrast, second-stage (HTC) ignition is significantly increased with increased HTC transition function. The remarkable increase in the ignition delay

[1]Since turbulent mixing results in effective Lewis numbers to approach unity [9, 131, 158, 165] the characteristics of laminar deflagrations in the unity Lewis number limit are likely to play a role in the turbulent flames.

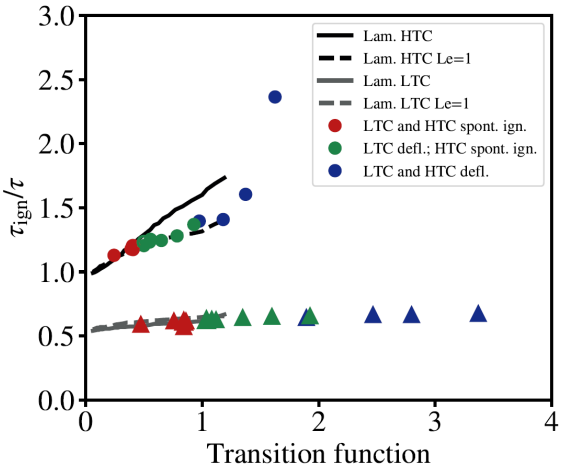

FIGURE 4.6: First and second-stage ignition delay with respect to the normalized inflow velocity for both laminar and turbulent flames. LTC ignition delay is denoted by triangles while HTC ignition delay is shown with circle symbols.

for the second-stage is likely to be a result of the reduction in LTC products' reactivity with increasing relative importance of effective diffusion in the cool flame [166] attributed to turbulent mixing. Strong turbulent mixing has been previously argued theoretically [131, 158] and found numerically [6, 9, 99, 160, 165, 191] to be driving effective Lewis numbers towards unity, *i.e.*, effectively reducing the importance of differential diffusion. The very good match between the unity Le laminar flame results and the turbulent flame results is consistent with the concept of increased effective diffusion through increased turbulent mixing. In addition, the match between turbulent and laminar results for both HTC and LTC suggests that the transition function identified is appropriate to model the increase in local ignition delay gradients (Eq. 2.32), associated with increased importance of diffusion.

The ignition delay is nearly two and a half times the corresponding homogeneous reactor value at $U_{\text{in}}/S_L = 4$ and $Re_t = 180$. Considering that the turbulent Reynolds number in the Spray A experiment is of order 1000 [127], the present phenomenon may contribute substantially to the Spray A flame ignition and stabilization behavior even though the jet center-line velocity at the flame lift-off location is an order of magnitude larger than the velocities considered here [37].

Finally, Fig. 4.6 indicates that integral length scale has a negligible effect on ignition delay over the range considered here, as all cases covering both integral length scales are included.

4.4 Flame structure and regime transition mechanism

4.4.1 Quasi-steady flame structure in progress variable space

Figure 4.7 presents the conditional mean of mass fraction of important species in progress variable space, with lines colored according to their propagation regime. LTC and HTC spontaneous ignitions are shown with red; LTC deflagration and HTC spontaneous ignition with green; LTC and HTC deflagrations denoted with blue. The laminar deflagration reference case ($U_{\text{in}} = 0.5$ m/s) is provided with dashed black line to show the deflagration limit in the absence of turbulence, while the 0D solution (pure spontaneous ignition) is presented with a solid black line.

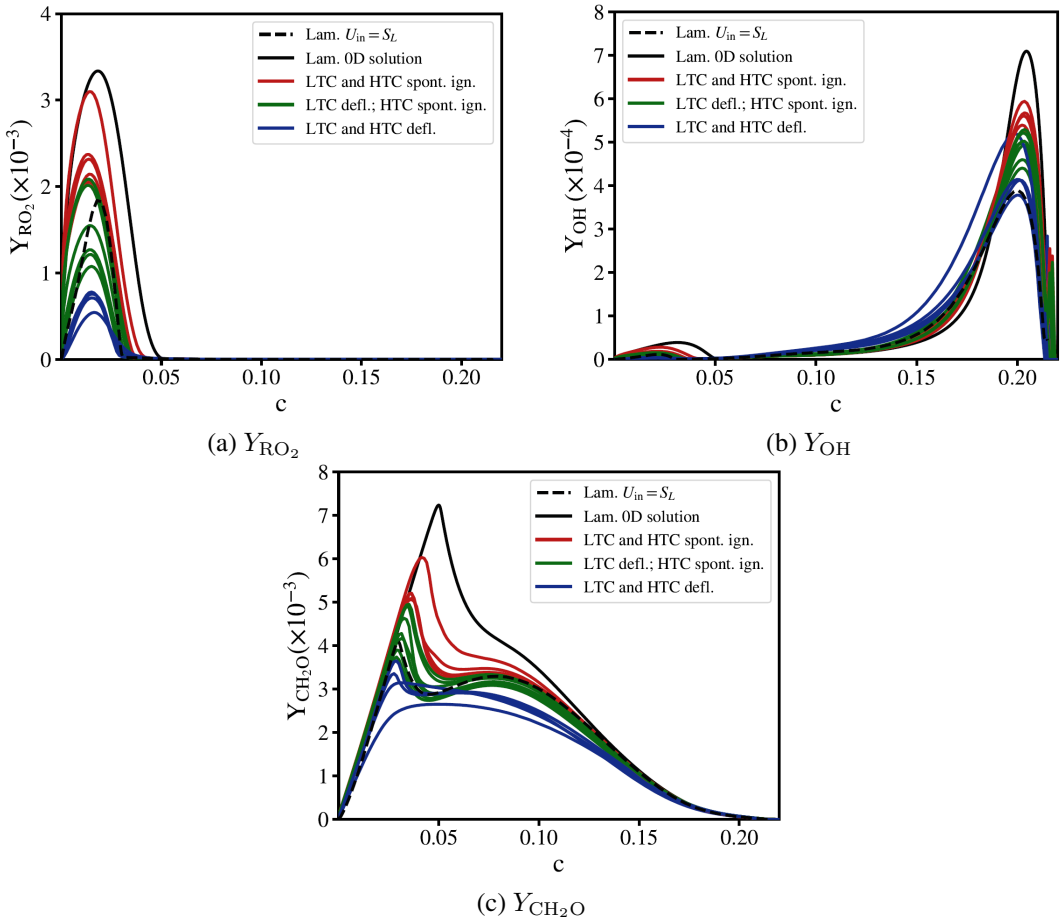

(a) Y_{RO_2} (b) Y_{OH}

(c) $Y_{\text{CH}_2\text{O}}$

FIGURE 4.7: Conditional mean of selected species mass fractions *vs.* progress variable for all turbulent flames showing (a) Y_{RO_2}, (b) Y_{OH}, and (c) $Y_{\text{CH}_2\text{O}}$.

Figure 4.7a shows Y_{RO_2} structure with respect to the progress variable. It can be seen that the laminar reference case is also a turning point for the propagation regime of the LTC flames in the presence of turbulence. As the magnitude of Y_{RO_2} drops lower

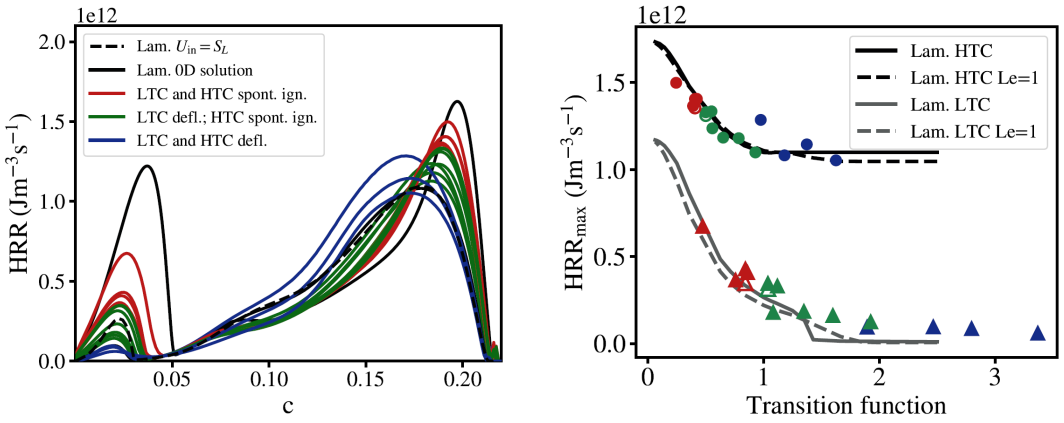

(a) Heat release rate (HRR)

(b) Maximum heat release rate

FIGURE 4.8: (a) Conditional mean of HRR *vs.* progress variable for all turbulent flames. Black dashed and solid lines denote laminar deflagration limit and 0D ignition, respectively. (b) First (LTC) and second (HTC) peaks obtained from (a) as a function of the transition function. Circles and triangles are used for HTC and LTC, respectively. Results from laminar flames with both transport models are added for comparison.

than that of laminar reference case, the LTC flames show characteristics of deflagration. Figure 4.7b presents the mean OH mass fraction product of HTC conditioned on the progress variable. As seen in this figure, the LTC and HTC deflagration cases match well the laminar deflagration limit, case 3, associated with non-negligible heat loss at the inlet, being an exception. Figure 4.7c presents formaldehyde CH_2O mass fraction, conditioned on the progress variable. Formaldehyde is an intermediate produced during LTC and consumed in HTC. The cases with larger mass fractions show a spontaneous ignition behaviour, and diffusion reduces the production of formaldehyde. It is worth mentioning that the cases with fully deflagrative flame response have an altered structure in terms of Y_{CH_2O} and show a one-peak trend instead of a double peak structure. This implies that the hot flame has caught up with the cool flame in these cases. We can conclude that a similar effect of diffusion on cool flame and hot flames is encountered in all figures. It is evident that diffusion enabled by decreasing inflow velocity or increasing the turbulence intensity, influences OH, RO_2, and CH_2O mass fractions such that lower values are encountered at more dominant diffusion-assisted combustion.

In addition to the qualitative analysis provided for HRR in Section 4.1, conditional mean heat release rate with respect to the progress variable is depicted in Fig. 4.8a, illustrating both LTC (left peak) and HTC (right peak) heat releasing regions. First, regarding LTC, a significant difference in HRR is exhibited between autoignitive and deflagrative cases, with a significant drop in HRR value in the presence of higher diffusion. Second,

for HTC, there is also a considerable change in HRR magnitude as the regime transition occurs. Furthermore, it is evident that the HRR from HTC peaks at lower progress variable values for the cases with higher diffusion contribution. Also, turbulent deflagrations all have a mean structure that is very close to that of laminar deflagrations, all falling in the vicinity of the depicted dashed black line.

The HRR peaks are extracted from Fig. 4.8a and plotted in Fig. 4.8b against the respective transition functions for LTC and HTC. The corresponding trends from laminar flames (mixture average and unity Lewis number) are also provided. The color scheme is the same as Fig. 4.8a for clarity. A significant drop in both LTC and HTC peak HRR is observed as the transition function increases, in particular for LTC. A strong correlation is exhibited between HRR peak and transition function, with the functional dependence between the two matching that of laminar flames.

Overall, these results show that the propagation mode has substantial influence on the flame structure of *n*-dodecane combustion at Spray A conditions. The same observation was made for cool turbulent and laminar *n*-heptane/air [160] and laminar *n*-dodecane flames [166]. In contrast, the study of Savard *et al.* [162] on hydrogen-vitiated air flames showed negligible dependence of the flame structure of the propagation mode (with the exception of HO_2 and H_2O_2 mass fractions). Modeling challenges, which are dependent on the thermochemical conditions considered, will be discussed in Section 4.7.

4.4.2 Mechanism governing the transition from turbulent spontaneous ignition to turbulent deflagration

To investigate the effect of turbulence on regime transition, an approach similar to that taken by Savard *et al.* [162] is followed in this section.

The density-weighted displacement speed of a progress variable iso-surface can be expressed as [61, 133]

$$S_{\mathrm{d}}{}^{*} = S_{\mathrm{d,r}}{}^{*} + S_{\mathrm{d,n}}{}^{*} + S_{\mathrm{d,c}}{}^{*} \tag{4.3}$$

where $S_{\mathrm{d,r}}{}^{*}$, $S_{\mathrm{d,n}}{}^{*}$, and $S_{\mathrm{d,c}}{}^{*}$ correspond to the density-weighted displacement speed components due to reaction, normal diffusion and curvature, respectively, and take the following expressions:

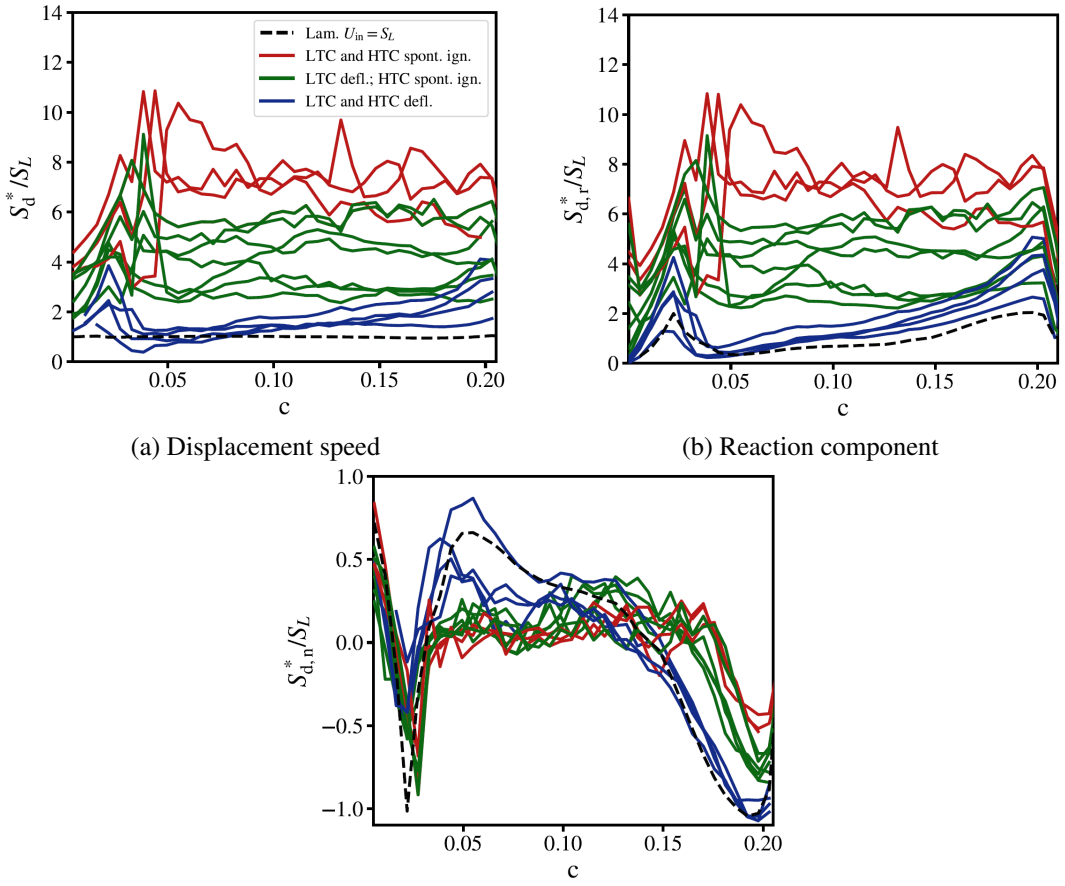

(a) Displacement speed

(b) Reaction component

(c) Diffusion component

FIGURE 4.9: (a) Conditional mean displacement speed ($S_d{}^*$), (b) its reaction component ($S_{d,r}{}^*$), (c) and its diffusion component ($S_{d,n}{}^*$) with respect to the progress variable.

$$S_{\mathrm{d,r}}{}^* = \frac{\dot{\omega}_c}{\rho_0 |\nabla c|}, \tag{4.4}$$

$$S_{\mathrm{d,n}}{}^* = \frac{1}{\rho_0 |\nabla c|} \frac{\partial}{\partial n} \left(\rho D \frac{\partial c}{\partial n} \right), \tag{4.5}$$

$$S_{\mathrm{d,c}}{}^* = -\frac{\rho D}{\rho_0} \kappa. \tag{4.6}$$

Here, $\dot{\omega}_c$ is the chemical source term of the progress variable, D is its diffusivity, n is a coordinate normal to the local progress variable iso-surface, and its curvature is κ.

The conditional mean density-weighted displacement speed and its components normalized with the laminar reference velocity in progress variable space are presented in

Fig. 4.9 for all deflagration and autoignition cases. Overall displacement speed is described in Fig. 4.9a, showing both cool and hot flames attached at displacement speeds around that of the reference laminar speed (blue lines). This suggests a value lower than $S^*_{\mathrm{d,r}}/S_L$ would fall in the LTC and HTC deflagration mode regime. For displacement speeds around 4 times the laminar reference speed, it is clearly observed that both LTC and HTC flames are stabilized as spontaneous ignition fronts (red lines). For displacement speeds in between these values, only the cool flame is attached (green lines). Additionally, the highest displacement speed corresponds to the case with the lowest contribution of diffusion. Furthermore, the mean displacement speed due to reaction and diffusion are depicted in Figures 4.9b and 4.9c, respectively. The mean of the component due to curvature is negligible, hence not shown (similar result obtained with hydrogen flames [162]). In addition, the diffusion component is small compared to the reaction component, particularly for spontaneous ignition cases. In other words, ${S_{\mathrm{d}}}^* \approx {S_{\mathrm{d,r}}}^*$ up to the transition to deflagration.

The reaction component of displacement speed is a function of the progress variable source term and the magnitude of progress variable gradient. The conditional mean magnitude of progress variable gradient is shown in progress variable space in Fig. 4.10b and is compared to the laminar equivalent in Fig. 4.10a. Similarly, the conditional mean of progress variable source term is presented in Fig. 4.10d, with the laminar equivalent in Fig. 4.10c.

According to Fig. 4.10a, gradients in the HTC region are increased as the effect of diffusion increases, eventually matching the laminar deflagration solution. In contrast, in the LTC region, a non-monotonic variation is identified. An increase in gradients is seen when the effect of diffusion is increased to some extent. After a certain threshold, by adding diffusion, we see a drop in the gradients as the flame becomes deflagrative. Similar behaviour is seen for the corresponding turbulent flames shown in Fig. 4.10b.

The observations in the HTC region are consistent with those of Savard *et al.* [162] for hydrogen-vitiated air flames. For LTC, the decrease in $S^*_{\mathrm{d,r}}$ observed across the transition to deflagration, is not attributed to an increase in $|\nabla c|$, but rather a decrease in progress variable source term. This is seen in Fig. 4.10c for laminar, and in Fig. 4.10d for turbulent flames. Accordingly, a considerable change is seen in the magnitude of $\dot{\omega}_c$ when more diffusion is introduced to the flame front. Figure 4.11 presents the evolution of the peaks identified in Fig. 4.10a to 4.10d for both LTC and HTC. This figure summarizes the mechanism through which the transition to deflagration occurs. For HTC,

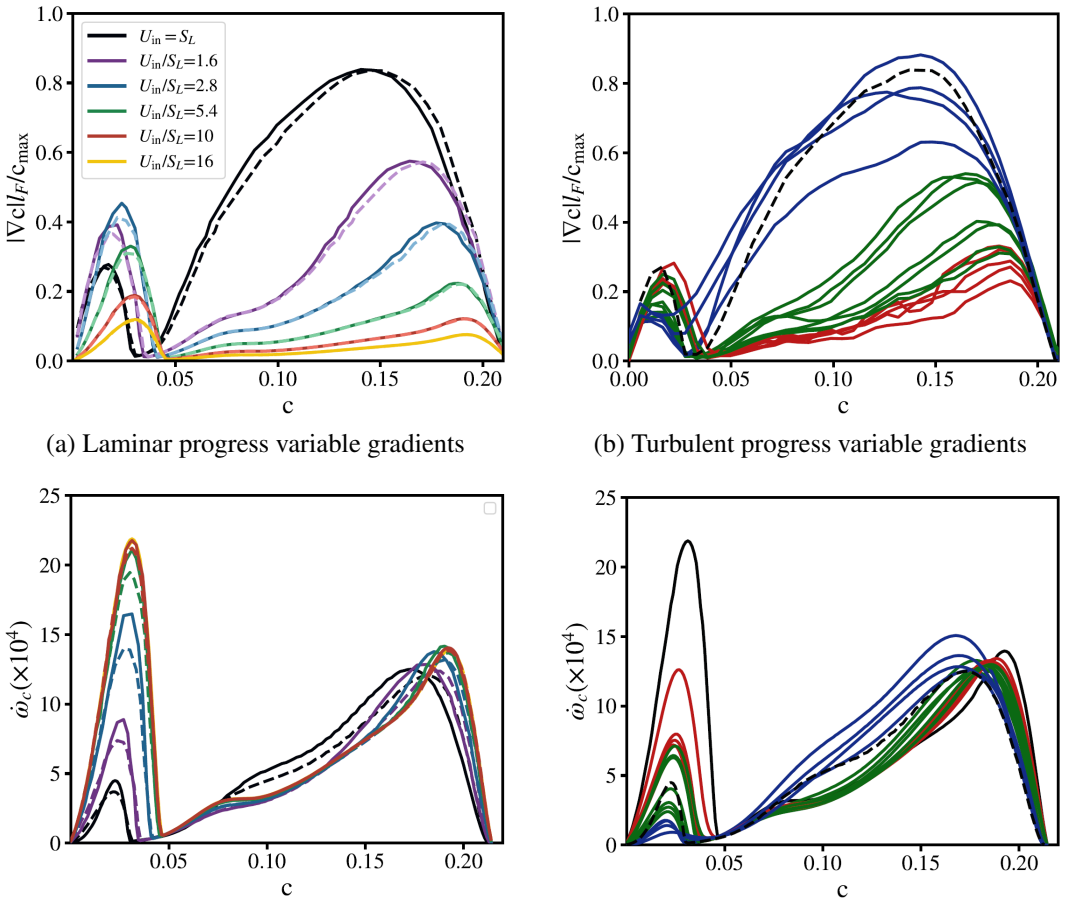

(a) Laminar progress variable gradients

(b) Turbulent progress variable gradients

(c) Laminar progress variable source terms

(d) Turbulent progress variable source terms

FIGURE 4.10: (a and b) Conditional mean magnitude of progress variable gradient ($|\nabla c|$) normalized with the ratio of maximum of progress variable and reference flame thickness *vs.* progress variable. (a) Laminar flames. (b) Turbulent flames. (c and d) Conditional mean progress variable source term *vs.* progress variable. The reference value used for normalization is the peak LTC progress variable source in the laminar reference deflagration. (c) Laminar flames. (d) Turbulent flames.

the mean progress variable source term is relatively insensitive to the transition function, while the mean magnitude of progress variable gradient increases with transition function, leading to the observed decrease in displacement speed. In contrast, for LTC, the mean of progress variable gradient decreases with increasing transition function as it crosses unity, while the mean progress variable source term decreases drastically. The latter decrease explains the decrease in displacement speed also observed for LTC.

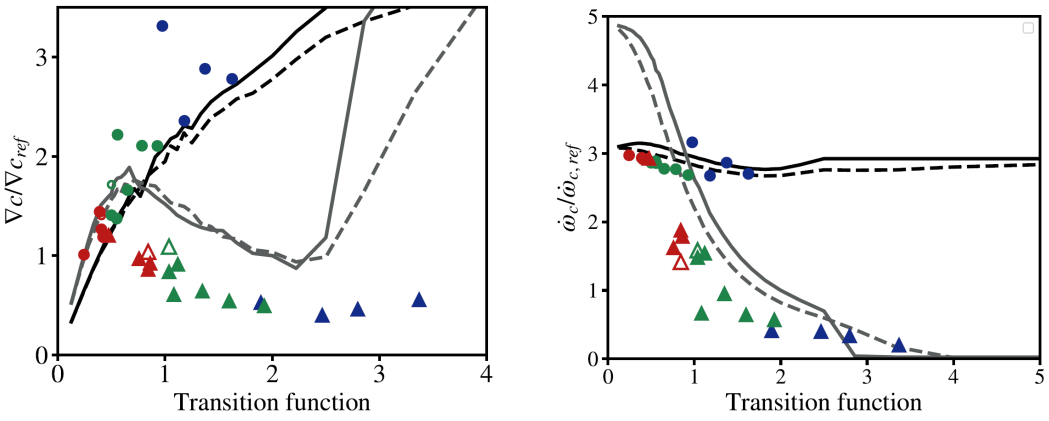

(a) Normalized progress variable gradient.

(b) Normalized progress variable source term.

FIGURE 4.11: Peak values for both LTC and HTC extracted from Fig. 4.10, *vs.* transition function. Reference values used for normalization are taken from the cool flame of the reference laminar deflagration. Circle symbols denote HTC, while triangles indicate LTC.

4.5 Chemical explosive mode analysis

Chemical explosive mode analysis (CEMA) [47, 89, 107, 111, 170, 197] was developed based on the computational singular perturbation [89, 98] framework. With CEMA, the chemistry and diffusion terms in the reactive scalar transport equations are projected onto the fastest growing chemical explosive mode (CEM), *i.e.*, the mode in state space with the largest growth rate, in order to quantitatively compare the relative importance of diffusion and chemistry. An arbitrary ratio of peak diffusion and chemical source term magnitudes has often been used to determine the propagation regime in turbulent ignition and lifted partially premixed flames [112, 202]. However, this ratio can be at least an order of magnitude lower than unity in deflagrations propagating in a highly reactive mixture [162]. In a recent study by Xu *et al.* [197], a more systematic technique was proposed to distinguish between propagation modes in premixed flames. Using 1D laminar flames, the authors showed that the local ratio of diffusion to chemical terms projected onto the fastest CEM consistently crosses unity in the preheat zone of deflagrations, while it remains below unity in spontaneous ignition fronts. Extracting the distribution of this ratio on an appropriately chosen iso-temperature surface within the preheat zone was suggested to be a more appropriate approach to determine the propagation mode in turbulent premixed flames. Savard *et al.* [165] used this approach in 3D hydrogen-vitiated air premixed flames and found the distribution to be an accurate proxy for the propagation mode, while Xu *et al.* [198] applied a similar analysis to 3D high Ka non-autoignitive *n*-dodecane flames. Consequently, in this section, this

CEMA-based method is used in the context of the present, more complex, autoignitive *n*-dodecane flames.

The derivation of Xu *et al.* [197] is provided. A transport equation for the chemical source terms can be written as

$$\frac{\mathrm{D}\dot{\boldsymbol{\omega}}\left(\boldsymbol{Y}\right)}{\mathrm{D}t} = \boldsymbol{J}_{\boldsymbol{\omega}}\frac{\mathrm{D}\boldsymbol{Y}}{\mathrm{D}t} = \boldsymbol{J}_{\boldsymbol{\omega}}(\dot{\boldsymbol{\omega}} + \boldsymbol{s}), \quad \boldsymbol{J}_{\boldsymbol{\omega}} = \frac{\partial\dot{\boldsymbol{\omega}}}{\partial\boldsymbol{Y}}, \tag{4.7}$$

where $\dot{\boldsymbol{\omega}}$ and $\boldsymbol{s}$ are the chemical and the non-chemical (here, molecular diffusion) source terms, respectively. $\boldsymbol{J}_{\boldsymbol{\omega}}$ is the chemical Jacobian, $\boldsymbol{Y}$ is a vector containing the species mass fractions and temperature. We define λ_{exp} as the eigenvalue of $\boldsymbol{J}_{\boldsymbol{\omega}}$ associated with the most explosive mode which are related by

$$\lambda_{\mathrm{exp}} = \boldsymbol{b}_{\mathrm{exp}}\boldsymbol{J}_{\boldsymbol{\omega}}\boldsymbol{a}_{\mathrm{exp}}, \tag{4.8}$$

where $\boldsymbol{a}_{\mathrm{exp}}$ and $\boldsymbol{b}_{\mathrm{exp}}$ are right and left eigenvectors associated with the most explosive mode, respectively. If multiple CEMs exist, λ_{exp} denotes the eigenvalue of the fastest explosive mode. If no CEM is present, λ_{exp} refers to the least negative (real part) eigenvalue. By projecting Eq. 4.7 onto the left eigenvector ($\boldsymbol{b}_{\mathrm{exp}}$) we obtain

$$\boldsymbol{b}_{\mathrm{exp}} \cdot \frac{\mathrm{D}\dot{\boldsymbol{\omega}}\left(\boldsymbol{Y}\right)}{\mathrm{D}t} = \boldsymbol{b}_{\mathrm{exp}} \cdot \boldsymbol{J}_{\boldsymbol{\omega}}(\dot{\boldsymbol{\omega}} + \boldsymbol{s}) = \lambda_{\mathrm{exp}}\boldsymbol{b}_{\mathrm{exp}} \cdot (\dot{\boldsymbol{\omega}} + \boldsymbol{s}) \tag{4.9}$$

$$\frac{\mathrm{D}\phi_{\omega}}{\mathrm{D}t} = \lambda_{\mathrm{exp}}\phi_{\omega} + \lambda_{\mathrm{exp}}\phi_{s} + \frac{\mathrm{D}\boldsymbol{b}_{\mathrm{exp}}}{\mathrm{D}t} \cdot \dot{\boldsymbol{\omega}}\left(\boldsymbol{Y}\right), \tag{4.10}$$

where the projected chemical (ϕ_{ω}) and diffusion (ϕ_{s}) source terms, and subsequently their ratio (local combustion mode indicator) are defined as

$$\phi_{\omega} \equiv \boldsymbol{b}_{\mathrm{exp}} \cdot \dot{\boldsymbol{\omega}}, \quad \phi_{s} \equiv \boldsymbol{b}_{\mathrm{exp}} \cdot \boldsymbol{s} \tag{4.11}$$

$$\alpha = \frac{\phi_{s}}{\phi_{\omega}} \tag{4.12}$$

The last term in Eq. 4.10 relates to the rotation (in phase space) of the most explosive mode. Its role in CEMA warrants further investigation, beyond the scope of this thesis [197].

With the method proposed by Xu *et al.* [197] and used in [162], the authors introduced T_0 defined as the temperature at which ϕ_s becomes greater than ϕ_{ω} in the deflagration

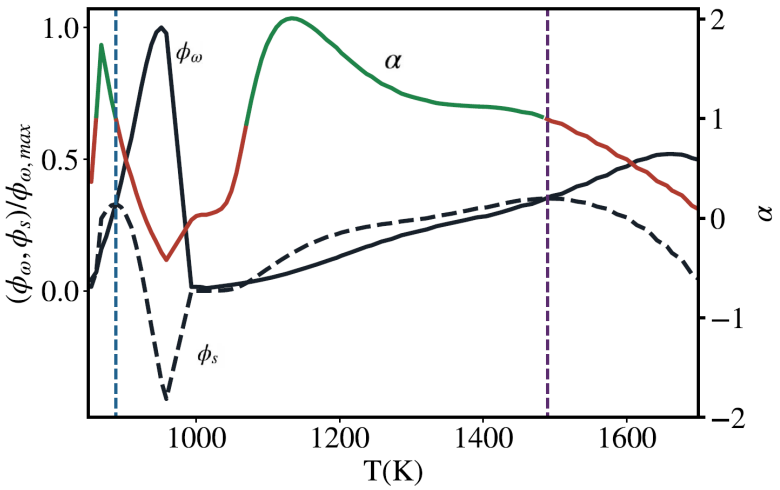

(a) Laminar $U_{\text{in}} = S_L$, providing $T_{0,\text{LTC}}$ and $T_{0,\text{HTC}}$.

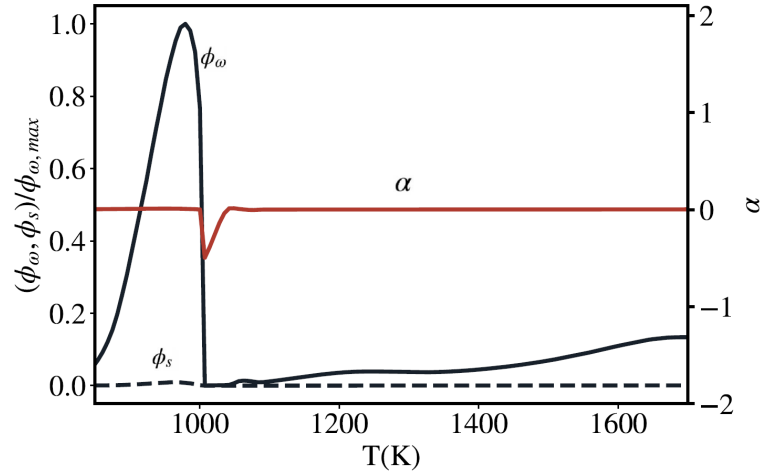

(b) Laminar $U_{\text{in}}/S_L = 16$, indicating a spontaneous ignition case.

FIGURE 4.12: The projected chemical (ϕ_ω) term with solid black line, and diffusion (ϕ_s) term with dashed black line with respect to temperature (normalized with $\phi_{\omega,max}$) are shown for (a) the laminar reference case, and (b) a spontaneous ignition case with $U_{\text{in}}/S_L = 16$. The ratio $\alpha = \phi_s/\phi_\omega$ is also shown in red for $|\alpha| < 1$ (local autoignition mode), and in green for $\alpha > 1$ (local diffusion-assisted ignition mode). The blue dashed line indicates the threshold temperature $T_{0,\text{LTC}}$, and the purple dashed line indicates the threshold temperature $T_{0,\text{HTC}}$.

limit. This method is extended to the present two-stage ignition flames. In that respect, $T_{0,\text{LTC}}$ for cool flames and $T_{0,\text{HTC}}$ for hot flames are identified. The process used to identified these temperatures includes calculation of α corresponding to the reference laminar deflagration ($U_{\text{in}} = S_L$), and subsequently, identifying the temperatures at the point where α becomes greater than 1 within each of LTC and HTC regions, as shown in Fig. 4.12. Evaluated at these temperatures, the value of α indicates the relative importance of chemistry and diffusion in the ignition process for the cool and hot flames,

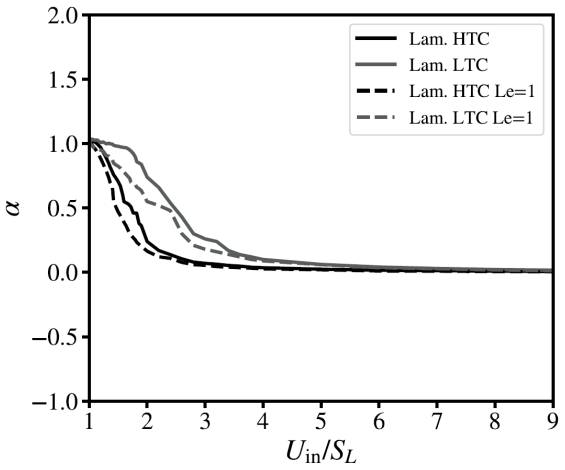

FIGURE 4.13: Laminar α (evaluated at respective T_0) *vs.* normalized inflow velocity for LTC and HTC with both unity and non-unity Lewis number.

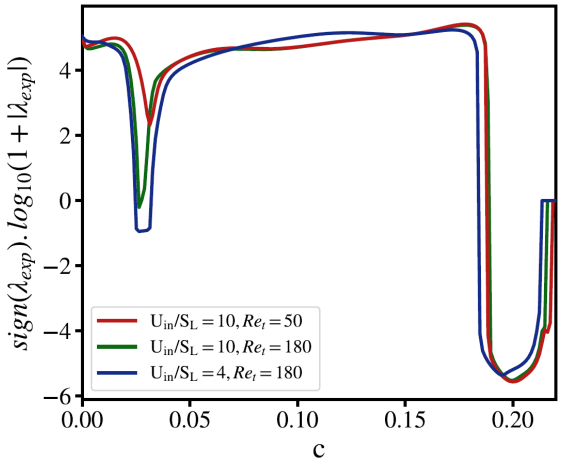

FIGURE 4.14: Explosive mode vs progress variable.

respectively. This is defined as the following. For $\alpha > 1$ a diffusion-assisted or dominant ignition mode is observed. A ratio between unity and minus unity denotes an autoignition mode where chemistry plays a dominant role in ignition while diffusion contributes less to the flame ignition, and lastly, $\alpha < -1$ represent an extinction mode where diffusion dominates and as a consequence reverses the ignition process.

Consistently, as shown in Fig. 4.13, α moves towards zero, *i.e.*, the chemical source term becomes dominant over the diffusion term as the inflow velocity increases. At the conditions which α becomes smaller than 1, we encounter a autoignition mode dominant flame while an α larger than 1, indicates a deflagration. Consistent results are obtained with both transport models (unity Lewis number and mixture-averaged).

In the following, CEMA is applied to the turbulent flames. First, explosive modes are analyzed to elucidate our understanding on the reactivity and explosiveness of the

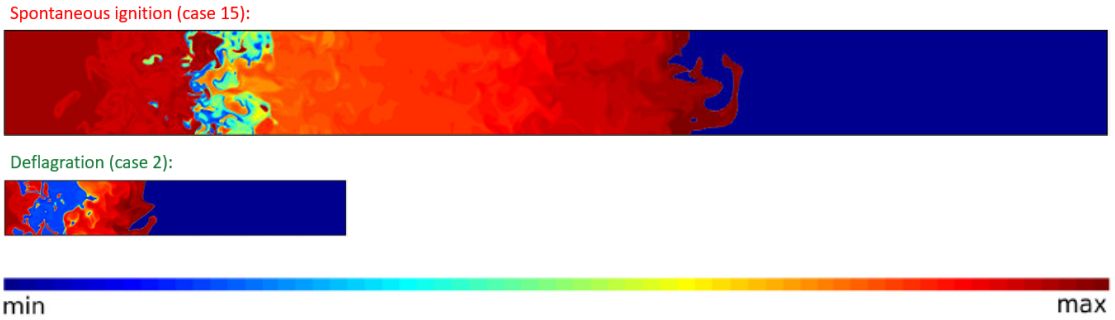

FIGURE 4.15: Contours of λ_{exp} for a representative turbulent ignition front (case 15) and a representative turbulent deflagration (case 2). The color bar shows a logarithmic scale ranging from -2.5 to 5.3.

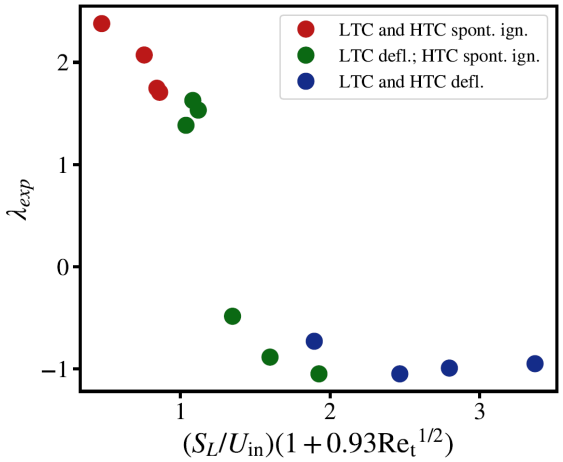

FIGURE 4.16: Minimum eigen value conditioned on temperature *vs.* transition function in the LTC region.

combustion regions for different flame conditions. Depicted in Fig. 4.14 is logarithmic representation of the mean most explosive eigenvalue conditioned on progress variable. According to this figure, the logarithmic scaled eigen-values conditioned on the progress variable show a drop of most explosive mode growth rate just after LTC. This observations shows the reduction in reactivity (explosiveness) of the mixture elements after the first-stage occurrence. An interesting observation is that this drop in reactivity is more pronounced following deflagrative cool flames. In addition, contour plots of λ_{exp} for two representative cases are also added in Fig. 4.15. It can be seen that a larger region with much smaller explosiveness is seen for the deflagration case compared to the spontaneous ignition one. Furthermore, Fig. 4.16 shows the minimum of λ_{exp} (most explosive mode magnitude representing the mode with largest instantaneous change) during the LTC for various cases, distinguished by their respective dominant combustion modes, with respect to the LTC transition function. Note that these values are in logarithmic scale, therefore the difference is considerable. A substantial drop in the LTC product reactivity following transition to deflagration can be clearly seen. This

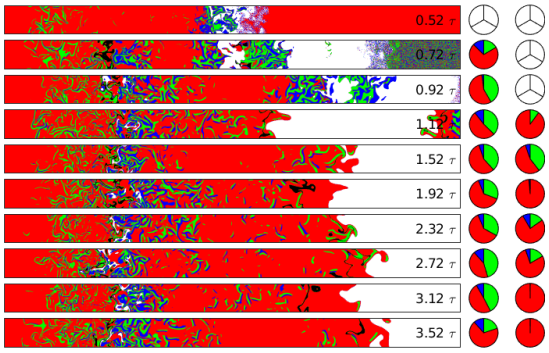

(a) $U_{\text{in}}/S_L = 10$, $Re_t = 50$.

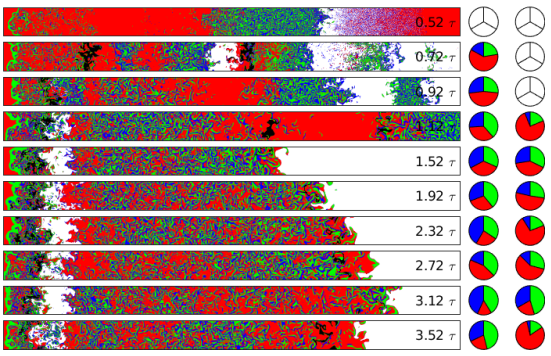

(b) $U_{\text{in}}/S_L = 10$, $Re_t = 180$.

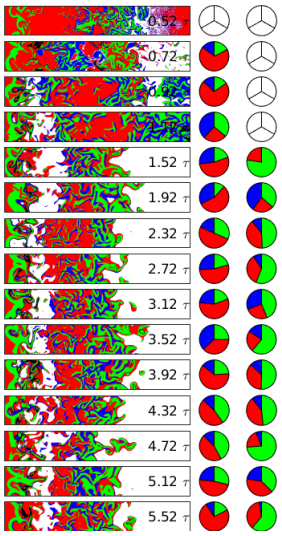

(c) $U_{\text{in}}/S_L = 4$, $Re_t = 50$.

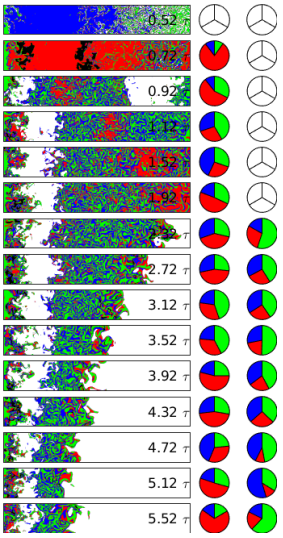

(d) $U_{\text{in}}/S_L = 4$, $Re_t = 180$.

FIGURE 4.17: 2D HRR contours corresponding to (a) $Re_t = 50$, (b) $Re_t = 180$, for $U_{\text{in}}/S_L = 10$, and (c) $Re_t = 50$, (d) $Re_t = 180$, for $U_{\text{in}}/S_L = 4$. τ is the 0D ignition delay equal to 2.25×10^{-4}. The first contour in each case corresponds to the half of 0D ignition delay (0.13 ms after injection), just prior to the first stage ignition delay. Red denotes autoignition mode; green is diffusion; blue indicates extinction mode.

result explains our previous observation in Section 4.3 where a delay in second-stage ignition was seen as cool flames transitioned to deflagrations.

Second, distribution of α is investigated using the same approach used for laminar calculations. Four different flames are considered in Fig. 4.17. The contours represent the three combustion modes defined by the local value of α (autoignition, diffusion, and extinction). The calculated reference temperatures, $T_{0,\text{LTC}}$ and $T_{0,\text{HTC}}$ are used in this section as iso-thermal surfaces to define the contribution pie chart for different flames as shown on the right hand side of each figure. Conditional distribution of α on these temperatures are shown on the left and right pie charts, indicating LTC and HTC

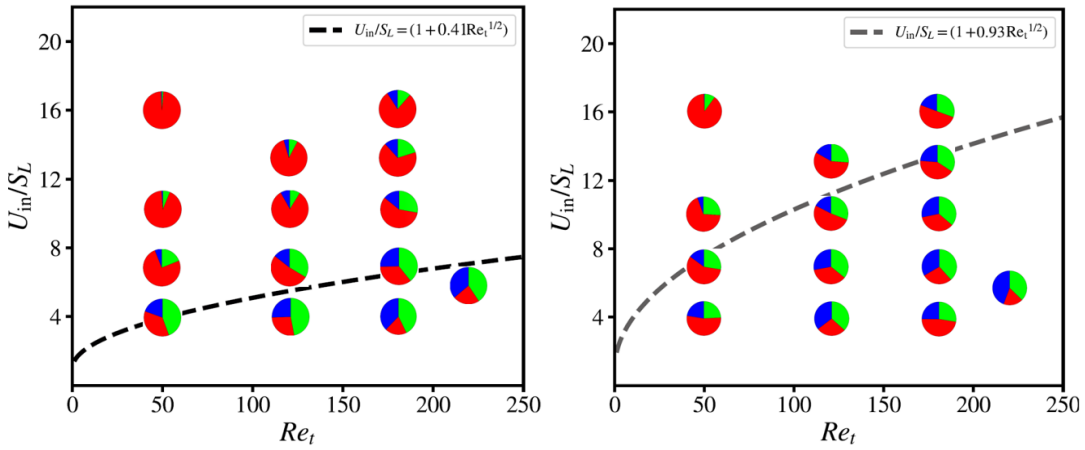

(a) HTC region. (b) LTC region.

FIGURE 4.18: Relative contribution of regime modes. Red denotes autoignition mode. Green indicates diffusion-assisted mode. Blue represents extinction mode.

regime contribution, respectively. Note that data sets with $\lambda_{\text{exp}} < 0$ are subjected to a zero weight to dismiss non-valid results [107, 197]. Looking at Fig. 4.17a, we see substantial contribution from autoignition throughout the domain, ranging from LTC to HTC. As described in the previous section, this case is characterized by LTC and HTC spontaneous ignition fronts. This can be further validated by considering the dominant contribution of spontaneous ignition depicted in the regime charts. Next, Fig. 4.17b also shows most of the mixture ahead of the HTC products evolves under spontaneous ignition, although, both diffusion and extinction modes play an increasingly large role in the LTC area. This indicates a flame with spontaneous ignition HTC while LTC deflagrating towards the inlet. Comparing these two cases, we witness that increased turbulence positively increases both diffusion and extinction. Figures 4.17c and 4.17d show HTC deflagration is enabled by decreasing the inflow velocity. Higher Re_t increases the extinction mode contribution, dominating autoignition even more.

To further specify the CEMA regimes, a period of statistically steady solution is selected for the corresponding flames. The average of these statistics are presented to show the relative contribution of the three combustion regime modes. This analysis is applied to all the turbulent flames performed in the present study and the respective regime diagram for LTC and HTC are shown in Fig. 4.18. First, we see that the incorporated transition functions are well correlated with contribution diagrams. By exploring these plots, we understand that for both LTC and HTC, at $T_{0,\text{LTC}}$ and $T_{0,\text{HTC}}$, respectively, if autoignition is the dominant mode, then the global propagation mode will be spontaneous ignition, while if extinction and diffusion are dominant over autoignition, the overall regime would be controlled by deflagration. This implies that the criterion

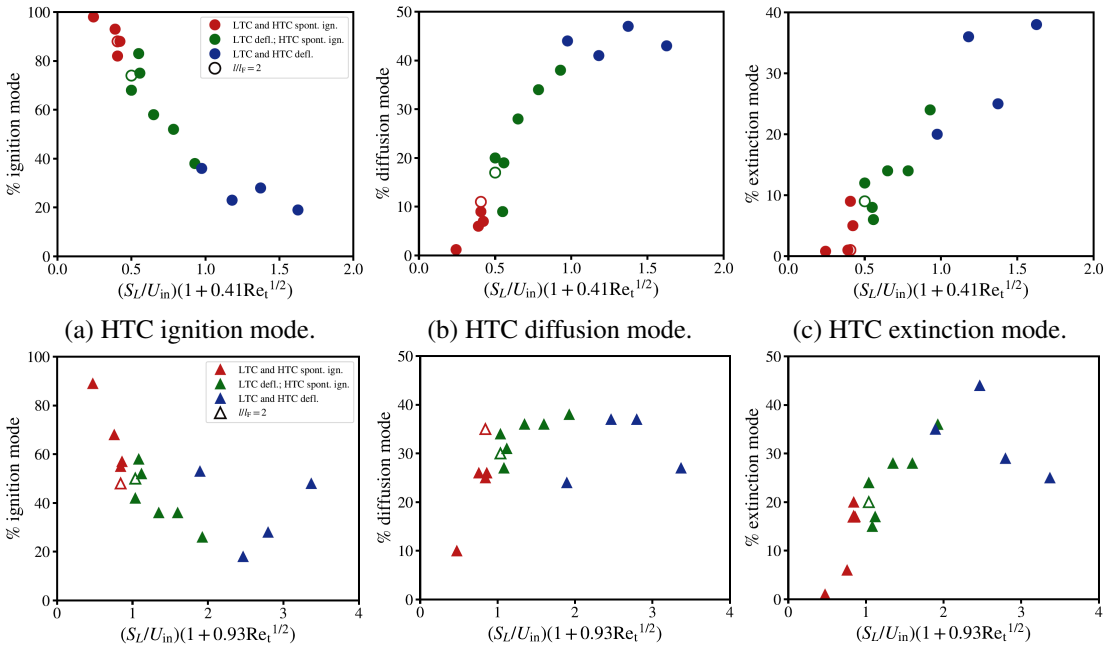

(a) HTC ignition mode. (b) HTC diffusion mode. (c) HTC extinction mode.

(d) LTC ignition mode. (e) LTC diffusion mode. (f) LTC extinction mode.

FIGURE 4.19: Relative contribution of local ignition, diffusion, and extinction modes conditioned on $T_{0,\mathrm{HTC}}$ for (a), (b), and (c), and $T_{0,\mathrm{LTC}}$ for (d), (e), and (f). The contributions are compared with respect to the appropriate transition function for HTC (top three plots) and LTC (bottom three plots).

proposed by Savard *et al.* [162] can be extended to the present mixture in the present study.

A more detailed assessment is provided by extracting and analysing the percentage of autoignition, diffusion, and extinction contribution with respect to the transition function for both LTC and HTC as shown in Fig. 4.19. For both HTC and LTC the contribution from autoignition mode decreases with increased magnitude of the transition function (Fig. 4.19a and 4.19d. The correlation between the two quantities is particularly strong for values of the transition function below unity, *i.e.*, for spontaneous ignition fronts. Diffusion (Fig. 4.19b and 4.19e) and extinction (Fig. 4.19c and 4.19f) modes show an opposite trend, but with a similar degree of correlation.

Savard *et al.* [162] found that the relative contribution of extinction mode was much better correlated with Ka than Re_t in hydrogen-vitiated air autoignitive flames. Here, the opposite was observed, with the strongest correlation obtained with the transition function. This discrepancy with previous work may be linked to the important drop in heat release rate peaks (Fig. 4.8b), but it warrants further investigation in future work. Note that Xu *et al.* [198] also found a strong increase in the contribution of extinction

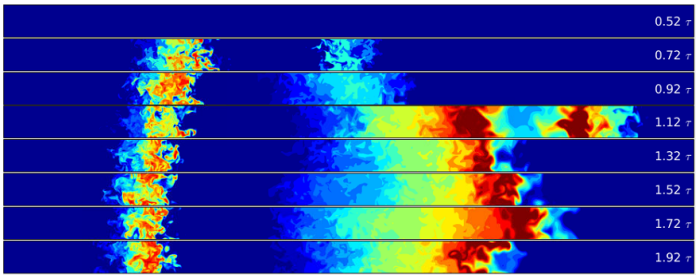

(a) $O_2 = 15\%$, $U_{\text{in}}/S_L = 13$, $Re_t = 120$.

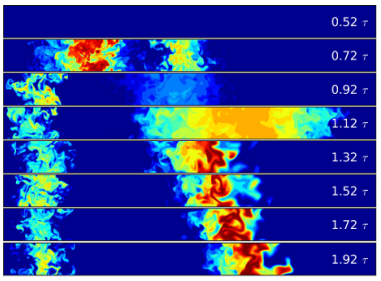

(b) $O_2 = 15\%$, $U_{\text{in}}/S_L = 7$, $Re_t = 120$.

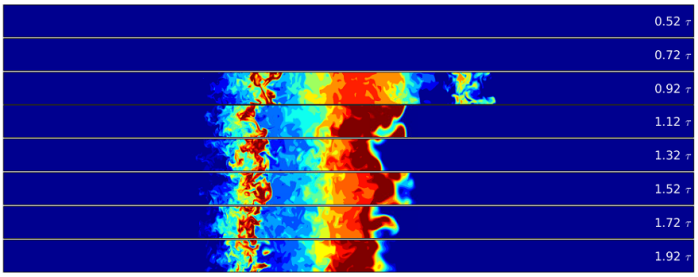

(c) $O_2 = 21\%$, $U_{\text{in}}/S_L = 13$, $Re_t = 120$.

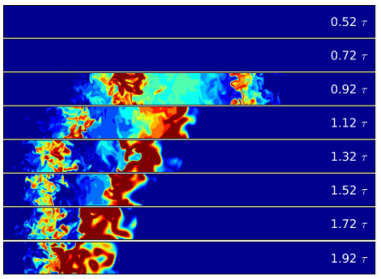

(d) $O_2 = 21\%$, $U_{\text{in}}/S_L = 7$, $Re_t = 120$.

FIGURE 4.20: 2D HRR contours corresponding to (a) $O_2 = 15\%$, (b) $O_2 = 21\%$, with $U_{\text{in}}/S_L = 7$, $Re_t = 120$. τ is the 0D ignition delay equal to 2.25×10^{-4}. The first contour in each case corresponds to the half of 0D ignition delay (0.13 ms after injection), just prior to the first stage ignition delay.

mode with Ka in non-autoignitive *n*-dodecane flames, but correlations with Ka and Re_t were not compared.

4.6 Higher oxygen level cases

By changing the oxygen concentration in the ambient gas at Spray A conditions, LTC and HTC reference flame speeds and ignition delays are altered, as previously noted [166]. It was identified that at higher oxygen concentration, HTC reference speed surpasses that of LTC. Thus, a hot flame is expected to catch up with a cool flame as it transitions to a deflagration. Note that this alteration in LTC and HTC flame speeds is true for the Spray A flames and could differ for other fuel/air mixtures. In this section we assess the role of oxygen concentration for the corresponding Spray A flames in presence of turbulence.

In this section, three turbulent cases are considered with $O_2 = 21\%$ in the unburnt mixture and the same conditions as described in Section 3.3. These cases were ran

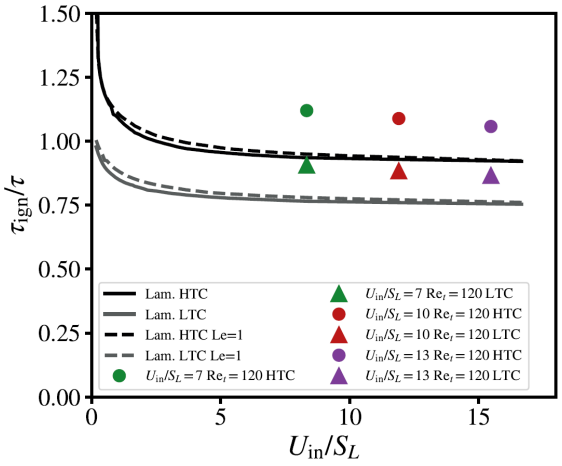

FIGURE 4.21: Laminar and turbulent flames with 21% O_2 level in the unburnt mixture.

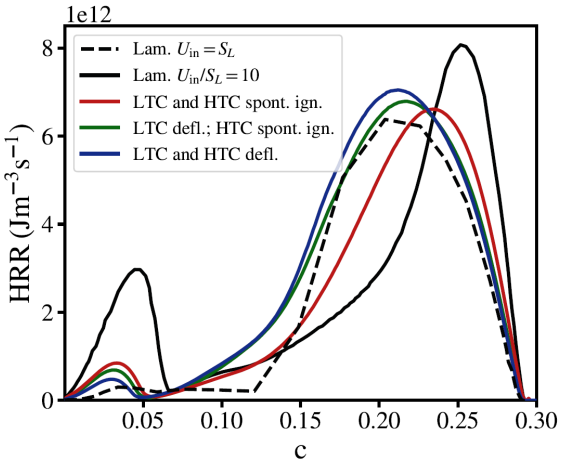

FIGURE 4.22: 21% O_2 HRR conditional mean on progress variable.

with the same Reynolds number, $Re_t = 120$, while with different inflow velocities of U_{in}=3.5 m/s, 5 m/s, and 6.5 m/s. Contour plots of HRR are provided for the aforementioned turbulent cases in Fig. 4.20 and a comparison is made with the corresponding $O_2 = 15\%$ cases. By comparing Fig. 4.20a with Fig. 4.20c, it is seen that a higher oxygen concentration brings the two LTC and HTC flames closer. Since LTC and HTC are spontaneous ignition fronts for both flames, the difference is mainly attributed to differences in first and second stage ignition delays. Upon reducing the inflow velocity (Fig. 4.20b), the cool flame transitions to a deflagration in the 15% O_2 case, with the hot flame pushed downstream. In contrast, in the 21% O_2 case (Fig 4.20d), the hot flame transitions to a deflagration and overtakes the cool flame. All 21% cases are included in the regime diagram presented in Fig. 4.5. For the 21% O_2 cases, no "split" between hot and cool flames was observed.

Turbulent ignition delay for the 21% O_2 cases are shown and compared to that of laminar flames for the corresponding conditions in Fig. 4.21. Comparing LTC and HTC turbulent ignition delay with laminar results we observe a non-negligible increase with turbulence for both stages.

Furthermore, conditional mean of HRR for these flames is provided in Fig. 4.22. A retarding effect upon transition is seen on the HTC HRR in progress variable space. This is while the peak HRR is also reduced as more diffusion is introduced to the flame front. This drop is more substantial in the LTC flames, as a large deviation is seen from the laminar spontaneous ignition front case. As the flames transition in presence of turbulence, their HRR reaches closer to that of the laminar reference deflagration case.

4.7 Discussion

The present quantitative and qualitative numerical results provide fundamental insights on the ignition and flame stabilization of *n*-dodecane turbulent premixed flames at CIE conditions. On one hand, some results obtained by Savard *et al.* [162] with hydrogen-vitiated air flames were found to be applicable to the present thermochemical conditions. First, the transition from spontaneous ignition to deflagration was attributed to Re_t and inflow velocity, with no independent influence of integral length scale. Second, for the hot flame, the mechanism governing this transition is the increase in magnitude of progress variable gradient under increased Re_t or reduced inflow velocity. Third, following the CEMA framework, the relative contribution of the autoignition mode was found to correlate well with the identified transition function. On the other hand, several new features were obtained. First, the transition to deflagration can occur in cool flames, while a hot flame may be stabilized by spontaneous ignition. In such a case, the hot flame is pushed downstream at baseline Spray A conditions (with equivalence ratio of 1.3) due to the reduced reactivity in the products of a cool deflagration. Second, the flame structure in phase space is strongly affected by the propagation mode for the present thermochemical conditions. Third, the mechanism governing the transition to deflagration in cool flames differs from that described above for hot flames. The increase in ignition delay gradients (or reduction in displacement speed) is attributed to a reduction in chemical source terms as the role of diffusion increases. Fourth, in the CEMA framework, the relative importance of the extinction mode was found to correlate with the transition function, rather than Karlovitz number [162]. Fifth, the ignition delay was found to strongly increase with the transition function. Finally, it was

shown that the above results are sensitive to oxygen level in the ambient gas at Spray A conditions, with the HTC favoured as the level is increased.

In the context of LES or RANS applications, a turbulent combustion model should be capable to capture the following turbulence chemistry interaction features identified in this thesis: 1) the transition to deflagration for both cool and hot flames independently, 2) the decreased reactivity following a cool deflagration, and 3) the important drop in chemical source terms in deflagrations, especially for LTC. The present results show that in a fully premixed environment, a simple transition model correlates well with the above features. In addition, it was found that a similar functional dependence on the transition function is obtained between laminar and turbulent cases. This suggests that a turbulent combustion model based on laminar flames (such as a flamelet generated manifold [189]) or on REDIM (reaction-diffusion manifold [23]), if designed carefully, may be appropriate to capture the desired model features listed above.

The present fundamental results are limited in their direct applicability by the fact that purely premixed mixture conditions were considered. In many engine applications (in particular CIEs), the fuel-ambient gas mixture burns in a partially premixed mode. Furthermore, the mean flow field is generally much more complex than that investigated here. Note that, while the transition function involves Re_t and U_{in}, a turbulent combustion model mapping from a laminar combustion manifold may not necessarily require these quantities.

Chapter 5

Conclusions and future work

5.1 Conclusions

A large series of three-dimensional simulations of turbulent premixed autoignitive *n*-dodecane flames at CIE diesel conditions (ECN's Spray A) were performed using DNS. The role of turbulence on the flame ignition, stabilization, and structure was assessed in order to distinguish turbulent spontaneous ignition fronts from turbulent deflagrations. In that regard, a qualitative contour analysis followed by a quantitative analysis on the turbulent flame position was conducted. A transition from spontaneous ignition to deflagration was encountered upon increasing turbulence. Consistent with previous studies, the same transition was seen as inflow velocity decreased, while the integral length scale showed very limited influence on the flame stabilization. Subsequently, stabilization regimes were identified to construct a regime diagram. Interestingly, in particular flow conditions, LTC transition occurred while the HTC ignition front was still maintained. At this point, by increasing diffusion to some extent, the HTC flame was pushed further downstream. This phenomenon denoted as "split" of the cool-hot double flame, was explained using results from our recent study under similar thermochemical conditions [166]. As a cool spontaneous ignition front transitions to a deflagration, heat diffusion from the cool flame products affects the chemical pathways, leading to a reduced reactivity in its products and increasing HTC ignition delay. As the ignition delay is increased the flame stabilizes further downstream.

Ignition delay was presented in terms of the proposed transition functions. The results highlighted the substantial effect of turbulence on HTC ignition delay. In contrast, LTC ignition delay remained constant even at very high diffusion, *i.e.*, low inflow velocity

and/or high turbulence. Additionally, the results further suggested the limited effect of integral length scale on the flame ignition. Ignition delay was shown to closely match the transition function for both LTC and HTC.

The flame structure was shown to substantially alter upon transition and HRR peak was shown to match the transition function for both stages, further approving the reliability of the purposed model. Moreover, displacement speed analysis showed limited influence from diffusion on the flame speed, while the reaction component played the dominant role. Speed limits between regime modes separating both stage spontaneous ignition from only LTC deflagration and both stage deflagration were identified.

For both laminar and turbulent flames, gradients in the HTC region were increased following the increase of diffusion. In contrast in the LTC region, a non-monotonic variation was identified. This was explained as HTC transition depends on increase in $|\nabla c|$ as corroborated in previous studies as well, while LTC transition is attributed to decrease in the progress variable source term. Furthermore, the ratio of the progress variable gradient and the source term of the progress variable was identified and defined as the mechanism responsible for the flame transition.

Finally, CEMA was provided to first support the identified regime diagram by more precisely assessing autoignition, diffusion, and extinction contributions to the overall flame structure and stabilization in quasi-steady state, and second, approve the incorporation of the purposed transition functions for LTC and HTC.

5.2 Original contributions

One, the remarkable "split" of the cool-hot double flame under the sole effect of turbulence was encountered as a new phenomenon in the ignition of two-staged flames under CIE diesel autoignitive conditions. In such a case, the hot flame is pushed downstream due to the reduced reactivity in the products of a cool deflagration.

Two, in the present thermochemical conditions (Spray A with equivalence ratio of 1.3), the flame structure in phase space was found to be highly sensitive to the propagation mode.

Three, a simple transition model was identified based on Re_t and U_{in} in the current fully premixed environment. Moreover, a similar functional dependence on the transition

function was obtained between laminar and turbulent cases. In particular, a negligible dependence on integral length scales was seen. This suggests the applicability of a well designed laminar-flame-based model in modelling of turbulent combustion under the present conditions.

Four, the ignition delay was strongly increased with the rise of the transition function.

Five, the mechanism governing the transition to deflagration in cool flames was found to be the reduction in chemical source terms due to increased diffusion (by increase in Re_t or reduction in U_{in}).

Six, the relative contribution of the extinction mode correlated with the transition function, rather than Ka number.

Seven, oxygen level in the ambient gas at Spray A conditions proved to alter the flame behavior, with the HTC favoured as the level is increased.

To conclude, the findings discussed above led to a simple a priori model capable of capturing the turbulence chemistry interaction features such as: 1) the transition to deflagration for both cool and hot flames, 2) the decreased reactivity as a consequence of a cool deflagration, and 3) the drop in chemical source terms in deflagrations (mainly important for LTC).

5.3 Recommendations for future work

This thesis addressed some of the fundamental concepts regarding the stabilization mechanism and the effect of turbulence on the transition of turbulent premixed flames at CIE conditions. However, the data sets obtained are rich and provide opportunities for further exploration. The 3D simulations were very long and expensive to run and, as such, were not further looked into for higher integral length scales and turbulent Reynolds numbers. Therefore a target would be to run simulations for higher Reynolds numbers to see more deflagrating HTC cases and also upscale the DNS by using higher integral length scales. This could approve or disapprove the low effect of integral length scale found on the current flames.

In the current conditions we used fully premixed configuration, while partially premixed flames are found in practice but relatively more challenging to model. Describing the

transition mechanism in two-stage Spray A flames under partially premixed conditions would be another challenge to resolve.

In this study a simplified canonical configuration was used to provide fundamental understanding on flame stabilization, while more complex configurations can be used to more accurately model real combustion chamber design and witness the effects of more realistic boundary conditions. Although, this would be very expensive with the current facilities and allocations, but hopefully in the near future it would be possible as the capabilities of supercomputers increase.

The studied cases in this thesis fall in the region of the thin reaction zones regime. To further assess the validity of the models and transition effects concluded in this study, it would be interesting to perform simulations in the broken/distributed reaction zones regime. This requires higher Ka, *i.e.* turbulence intensity, and subsequently, higher computational cost.

For the thermochemical conditions, only oneequivalence ratio, and one unburnt mixture temperature were considered. The analysis could be extended to mixtures with different unburnt temperatures and possibly higher or lower equivalence ratios.

Bibliography

[1] ABDEL-GAYED, R., BRADLEY, D., AND LUNG, F. Combustion regimes and the straining of turbulent premixed flames. *Combustion and Flame 76*, 2 (1989), 213–218.

[2] ADITYA, K., GRUBER, A., XU, C., LU, T., KRISMAN, A., BOTHIEN, M., AND CHEN, J. Direct numerical simulation of flame stabilization assisted by autoignition in a reheat gas turbine combustor. *Proceedings of the Combustion Institute 37*, 2 (2019), 2635–2642.

[3] AJROUCHE, H., NILAPHAI, O., MOREAU, B., HESPEL, C., FOUCHER, F., AND MOUNAÏM-ROUSSELLE, C. Engine combustion network (ECN): characterization and comparison of diesel spray combustion in new high-pressure and high-temperature chamber. *Proceeding of the 2017 ILASS 19th annual conference on liquid atomization and spray systems, Jeju, Korea* (2017), 18–21.

[4] AL-ENAZI, A., OKONKWO, E., BICER, Y., AND AL-ANSARI, T. A review of cleaner alternative fuels for maritime transportation. *Energy Reports 7* (2021), 1962–1985.

[5] ANSARI, A., JAYACHANDRAN, J., AND EGOLFOPOULOS, F. N. Parameters influencing the burning rate of laminar flames propagating into a reacting mixture. *Proceedings of the Combustion Institute 37*, 2 (2019), 1513–1520.

[6] ASPDEN, A., DAY, M., AND BELL, J. Lewis number effects in distributed flames. *Proceedings of the Combustion Institute 33*, 1 (2011), 1473–1480.

[7] ASPDEN, A., DAY, M., AND BELL, J. Turbulence–flame interactions in lean premixed hydrogen: transition to the distributed burning regime. *Journal of Fluid Mechanics 680* (2011), 287–320.

[8] ASPDEN, A., DAY, M., AND BELL, J. Turbulence-chemistry interaction in lean premixed hydrogen combustion. *Proceedings of the Combustion Institute 35*, 2 (2015), 1321–1329.

[9] ASPDEN, A., DAY, M., AND BELL, J. Three-dimensional direct numerical simulation of turbulent lean premixed methane combustion with detailed kinetics. *Combustion and Flame 166* (2016), 266–283.

[10] ASPDEN, A., DAY, M., AND BELL, J. Towards the distributed burning regime in turbulent premixed flames. *Journal of Fluid Mechanics 871* (2019), 1–21.

[11] BALDI, F., LARSEN, U., AND GABRIELII, C. Comparison of different procedures for the optimisation of a combined diesel engine and organic rankine cycle system based on ship operational profile. *Ocean Engineering 110* (2015), 85–93.

[12] BANOS, R., AGUGLIARO, F., MONTOYA, F., GIL, C., ALCAYDE, A., AND GÓMEZ, J. Optimization methods applied to renewable and sustainable energy: A review. *Renewable and Sustainable Energy Reviews 15*, 4 (2011), 1753–1766.

[13] BANSAL, G., MASCARENHAS, A., AND CHEN, J. Direct numerical simulations of autoignition in stratified dimethyl-ether (DME)/air turbulent mixtures. *Combustion and Flame 162*, 3 (2015), 688–702.

[14] BENAJES, J., PAYRI, R., BARDI, M., AND MARTÍ-ALDARAVÍ, P. Experimental characterization of diesel ignition and lift-off length using a single-hole ECN injector. *Applied Thermal Engineering 58*, 1-2 (2013), 554–563.

[15] BERGTHORSON, J., AND THOMSON, M. A review of the combustion and emissions properties of advanced transportation biofuels and their impact on existing and future engines. *Renewable and Sustainable Energy Reviews 42* (2015), 1393–1417.

[16] BERTOLINO, A., FÜRST, M., STAGNI, A., FRASSOLDATI, A., PELUCCHI, M., CAVALLOTTI, C., FARAVELLI, T., AND PARENTE, A. An evolutionary, data-driven approach for mechanism optimization: theory and application to ammonia combustion. *Combustion and Flame 229* (2021), 111366.

[17] BHATTACHARJEE, S., AND HAWORTH, D. Simulations of transient *n*-heptane and *n*-dodecane spray flames under engine-relevant conditions using a transported PDF method. *Combustion and Flame 160*, 10 (2013), 2083–2102.

[18] BICER, Y., AND DINCER, I. Life cycle assessment of ammonia utilization in city transportation and power generation. *Journal of Cleaner Production 170* (2018), 1594–1601.

[19] BLANQUART, G. Caltechmech. https://www.theforce.caltech.edu/CaltechMech/, 2015.

[20] BORGHESI, G., KRISMAN, A., LU, T., AND CHEN, J. Direct numerical simulation of a temporally evolving air/*n*-dodecane jet at low-temperature diesel-relevant conditions. *Combustion and Flame 195* (2018), 183–202.

[21] BORGHI, R. On the structure and morphology of turbulent premixed flames. *Recent Advances in the Aerospace Sciences* (1985), 117–138.

[22] BRUNELLE-YEUNG, E., MASEK, T., ROJO, J., LEVY, J., ARUNACHALAM, S., MILLER, S., BARRETT, S., KUHN, S., AND WAITZ, I. Assessing the impact of aviation environmental policies on public health. *Transport Policy 34* (2014), 21–28.

[23] BYKOV, V., AND MAAS, U. The extension of the ILDM concept to reaction–diffusion manifolds. *Combustion Theory and Modelling 11*, 6 (2007), 839–862.

[24] CARDIN, C., RENOU, B., CABOT, G., AND BOUKHALFA, A. Experimental analysis of laser-induced spark ignition of lean turbulent premixed flames: New insight into ignition transition. *Combustion and Flame 160*, 8 (2013), 1414–1427.

[25] CARROLL, P., AND BLANQUART, G. A proposed modification to Lundgren's physical space velocity forcing method for isotropic turbulence. *Physics of Fluids 25*, 10 (2013), 105114.

[26] CHEN, J., HAWKES, E., SANKARAN, R., MASON, S., AND IM, H. Direct numerical simulation of ignition front propagation in a constant volume with temperature inhomogeneities: I. fundamental analysis and diagnostics. *Combustion and Flame 145*, 1-2 (2006), 128–144.

[27] CHEN, Y., AND BILGER, R. Experimental investigation of three-dimensional flame-front structure in premixed turbulent combustion: II. lean hydrogen/air bunsen flames. *Combustion and Flame 138*, 1-2 (2004), 155–174.

[28] CHISHTY, M., BOLLA, M., HAWKES, E., PEI, Y., AND KOOK, S. Soot formation modelling for *n*-dodecane sprays using the transported PDF model. *Combustion and Flame 192* (2018), 101–119.

[29] CHU, S., CUI, Y., AND LIU, N. The path towards sustainable energy. *Nature Materials 16*, 1 (2017), 16–22.

[30] CHU, S., AND MAJUMDAR, A. Opportunities and challenges for a sustainable energy future. *nature 488*, 7411 (2012), 294–303.

[31] CIEZKI, H., AND ADOMEIT, G. Shock-tube investigation of self-ignition of *n*-heptane-air mixtures under engine relevant conditions. *Combustion and Flame 93*, 4 (1993), 421–433.

[32] COLBAN, W., MILES, P., AND OH, S. Effect of intake pressure on performance and emissions in an automotive diesel engine operating in low temperature combustion regimes. *SAE Transactions* (2007), 957–977.

[33] CRABTREE, G., AND DRESSELHAUS, M. The hydrogen fuel alternative. *Mrs Bulletin 33*, 4 (2008), 421–428.

[34] CURRAN, H., GAFFURI, P., PITZ, W., AND WESTBROOK, C. A comprehensive modeling study of *n*-heptane oxidation. *Combustion and Flame 114*, 1-2 (1998), 149–177.

[35] DAGAUT, P., AND CATHONNET, M. The ignition, oxidation, and combustion of kerosene: A review of experimental and kinetic modeling. *Progress in Energy and Combustion Science 32*, 1 (2006), 48–92.

[36] DALAKOTI, D. Direct numerical simulation of lifted flames in diesel engine conditions.

[37] DALAKOTI, D., SAVARD, B., HAWKES, E., WEHRFRITZ, A., WANG, H., DAY, M., AND BELL, J. Direct numerical simulation of a spatially developing *n*-dodecane jet flame under spray A thermochemical conditions: Flame structure and stabilisation mechanism. *Combustion and Flame 217* (2020), 57–76.

[38] DALAKOTI, D., SAVARD, B., WEHRFRITZ, A., DAY, M., BELL, J., AND HAWKES, E. Rich premixed flame in a spatially developing *n*-dodecane jet in diesel engine conditions.

[39] DAVIDOVIC, M., FALKENSTEIN, T., BODE, M., CAI, L., KANG, S., HINRICHS, J., AND PITSCH, H. LES of *n*-dodecane spray combustion using a multiple representative interactive flamelets model. *Oil & Gas Science and Technology–Revue d'IFP Energies nouvelles 72*, 5 (2017), 29.

[40] DE FRAITURE, C., GIORDANO, M., AND LIAO, Y. Biofuels and implications for agricultural water use: blue impacts of green energy. *Water Policy 10*, S1 (2008), 67–81.

[41] DE OJEDA, W., ZOLDAK, P., ESPINOSA, R., AND KUMAR, R. Development of a fuel injection strategy for diesel LTC. Tech. rep., SAE Technical Paper, 2008.

[42] DEC, J. A conceptual model of DL diesel combustion based on laser-sheet imaging. *SAE Transactions* (1997), 1319–1348.

[43] DEMPSEY, A., WALKER, N., GINGRICH, E., AND REITZ, R. Comparison of low temperature combustion strategies for advanced compression ignition engines with a focus on controllability. *Combustion Science and Technology 186*, 2 (2014), 210–241.

[44] DESAI, S., SANKARAN, R., AND IM, H. Direct numerical simulation of an autoignitive turbulent flame in a stratified dimethyl-ether (DME)/air mixture. Tech. rep., Oak Ridge National Lab.(ORNL), Oak Ridge, TN (United States), 2019.

[45] DESJARDINS, O., BLANQUART, G., BALARAC, G., AND PITSCH, H. High order conservative finite difference scheme for variable density low mach number turbulent flows. *Journal of Computational Physics 227*, 15 (2008), 7125–7159.

[46] DHYANI, V., AND BHASKAR, T. A comprehensive review on the pyrolysis of lignocellulosic biomass. *Renewable Energy 129* (2018), 695–716.

[47] DIAMANTIS, D., KYRITSIS, D., AND GOUSSIS, D. The reactions supporting or opposing the development of explosive modes: Autoignition of a homogeneous methane/air mixture. *Proceedings of the Combustion Institute 35*, 1 (2015), 267–274.

[48] DIMITRIOU, P., KUMAR, M., TSUJIMURA, T., AND SUZUKI, Y. Combustion and emission characteristics of a hydrogen-diesel dual-fuel engine. *International Journal of Hydrogen Energy 43*, 29 (2018), 13605–13617.

[49] DINCER, I. Renewable energy and sustainable development: a crucial review. *Renewable and Sustainable Energy Reviews 4*, 2 (2000), 157–175.

[50] DODDS, P., STAFFELL, I., HAWKES, A., LI, F., GRÜNEWALD, P., MCDOWALL, W., AND EKINS, P. Hydrogen and fuel cell technologies for heating: A review. *International Journal of Hydrogen Energy 40*, 5 (2015), 2065–2083.

[51] DREWS, M., LARSEN, M., AND BALDERRAMA, J. Projected water usage and land-use-change emissions from biomass production (2015–2050). *Energy Strategy Reviews 29* (2020), 100487.

[52] DRISCOLL, J., CHEN, J., SKIBA, A., CARTER, C., HAWKES, E., AND WANG, H. Premixed flames subjected to extreme turbulence: Some questions and recent answers. *Progress in Energy and Combustion Science 76* (2020), 100802.

[53] DUNN, M., MASRI, A., AND BILGER, R. A new piloted premixed jet burner to study strong finite-rate chemistry effects. *Combustion and Flame 151*, 1-2 (2007), 46–60.

[54] DUNN, M., MASRI, A., BILGER, R., BARLOW, R., AND WANG, G. The compositional structure of highly turbulent piloted premixed flames issuing into a hot coflow. *Proceedings of the Combustion Institute 32*, 2 (2009), 1779–1786.

[55] EBI, D., DOLL, U., SCHULZ, O., XIONG, Y., AND NOIRAY, N. Ignition of a sequential combustor: Evidence of flame propagation in the autoignitable mixture. *Proceedings of the Combustion Institute 37*, 4 (2019), 5013–5020.

[56] EDENHOFER, O. *Climate change 2014: mitigation of climate change*, vol. 3. Cambridge University Press, 2015.

[57] FLECK, J., GRIEBEL, P., STEINBERG, A., STÖHR, M., AIGNER, M., AND CIANI, A. Autoignition limits of hydrogen at relevant reheat combustor operating conditions. *Journal of Engineering for Gas Turbines and Power 134*, 4 (2012).

[58] GAUTHIER, B., DAVIDSON, D., AND HANSON, R. Shock tube determination of ignition delay times in full-blend and surrogate fuel mixtures. *Combustion and Flame 139*, 4 (2004), 300–311.

[59] GONG, C., JANGI, M., AND BAI, X.-S. Large eddy simulation of *n*-dodecane spray combustion in a high pressure combustion vessel. *Applied Energy 136* (2014), 373–381.

[60] GOODWIN, D., MOFFAT, H., AND SPETH, R. Cantera: An object-oriented software toolkit for chemical kinetics, thermodynamics, and transport processes, 2009.

[61] GRAN, I., ECHEKKI, T., AND CHEN, J. Negative flame speed in an unsteady 2-D premixed flame: A computational study. In *Symposium (International) on Combustion* (1996), vol. 26, Elsevier, pp. 323–329.

[62] GREENE, D., BAKER JR, H., AND PLOTKIN, S. Reducing greenhouse gas emissions from us transportation.

[63] GRIFFITHS, J., HALFORD-MAW, P., AND ROSE, D. Fundamental features of hydrocarbon autoignition in a rapid compression machine. *Combustion and Flame 95*, 3 (1993), 291–306.

[64] GROGAN, K., GOLDSBOROUGH, S., AND IHME, M. Ignition regimes in rapid compression machines. *Combustion and Flame 162*, 8 (2015), 3071–3080.

[65] GRUBER, A., BOTHIEN, M., CIANI, A., ADITYA, K., CHEN, J., AND WILLIAMS, F. Direct numerical simulation of hydrogen combustion at autoignitive conditions: Ignition, stability and turbulent reaction-front velocity. *Combustion and Flame 229* (2021), 111385.

[66] GUEDES, A., BRAGA, S., AND PRADELLE, F. Performance and combustion characteristics of a compression ignition engine running on diesel-biodiesel-ethanol (DBE) blends–part 2: Optimization of injection timing. *Fuel 225* (2018), 174–183.

[67] GÜTHE, F., HELLAT, J., AND FLOHR, P. The reheat concept: the proven pathway to ultralow emissions and high efficiency and flexibility. *Journal of Engineering for Gas Turbines and Power 131*, 2 (2009).

[68] HABISREUTHER, P., GALEAZZO, F., PRATHAP, C., AND ZARZALIS, N. Structure of laminar premixed flames of methane near the autoignition limit. *Combustion and Flame 160*, 12 (2013), 2770–2782.

[69] HASELI, Y. Maximum conversion efficiency of hydrogen fuel cells. *international Journal of Hydrogen Energy 43*, 18 (2018), 9015–9021.

[70] HAWKES, E., CHATAKONDA, O., KOLLA, H., KERSTEIN, A., AND CHEN, J. A petascale direct numerical simulation study of the modelling of flame wrinkling for large-eddy simulations in intense turbulence. *Combustion and Flame 159*, 8 (2012), 2690–2703.

[71] HAWKES, E., SANKARAN, R., PÉBAY, P., AND CHEN, J. Direct numerical simulation of ignition front propagation in a constant volume with temperature inhomogeneities: II. parametric study. *Combustion and Flame 145*, 1-2 (2006), 145–159.

[72] HERNER, J., HU, S., ROBERTSON, W., HUAI, T., CHANG, M., RIEGER, P., AND AYALA, A. Effect of advanced aftertreatment for PM and NO_x reduction on heavy-duty diesel engine ultrafine particle emissions. *Environmental Science & Technology 45*, 6 (2011), 2413–2419.

[73] HERRMANN, M., BLANQUART, G., AND RAMAN, V. Flux corrected finite volume scheme for preserving scalar boundedness in reacting large-eddy simulations. *AIAA Journal 44*, 12 (2006), 2879–2886.

[74] HEUFER, K., AND OLIVIER, H. Determination of ignition delay times of different hydrocarbons in a new high pressure shock tube. *Shock Waves 20*, 4 (2010), 307–316.

[75] HOFFMANN, P. *Tomorrow's energy: hydrogen, fuel cells, and the prospects for a cleaner planet*. MIT Press, 2012.

[76] HOORNWEG, D., SUGAR, L., AND GÓMEZ, C. Cities and greenhouse gas emissions: moving forward. *Environment and Urbanization 23*, 1 (2011), 207–227.

[77] HUANG, D., ZHOU, H., AND LIN, L. Biodiesel: an alternative to conventional fuel. *Energy Procedia 16* (2012), 1874–1885.

[78] HUESTIS, E., ERICKSON, P., AND MUSCULUS, M. In-cylinder and exhaust soot in low-temperature combustion using a wide-range of EGR in a heavy-duty diesel engine. *SAE Transactions* (2007), 860–870.

[79] HULT, J., GASHI, S., CHAKRABORTY, N., KLEIN, M., JENKINS, K., CANT, S., AND KAMINSKI, C. Measurement of flame surface density for turbulent premixed flames using PLIF and DNS. *Proceedings of the Combustion Institute 31*, 1 (2007), 1319–1326.

[80] HULTQVIST, A., CHRISTENSEN, M., JOHANSSON, B., RICHTER, M., NYGREN, J., HULT, J., AND ALDÉN, M. The HCCI combustion process in a single cycle—high-speed fuel tracer LIF and chemiluminescence imaging. *SAE Transactions* (2002), 913–927.

[81] HUO, H., WANG, M., BLOYD, C., AND PUTSCHE, V. Life-cycle assessment of energy use and greenhouse gas emissions of soybean-derived biodiesel and renewable fuels. *Environmental Science & Technology 43*, 3 (2009), 750–756.

[82] IM, H., PAL, P., WOOLDRIDGE, M., AND MANSFIELD, A. A regime diagram for autoignition of homogeneous reactant mixtures with turbulent velocity and temperature fluctuations. *Combustion Science and Technology 187*, 8 (2015), 1263–1275.

[83] JOHNSON, T. Diesel emission control in review. *SAE International Journal of Fuels and Lubricants 1*, 1 (2009), 68–81.

[84] JOSEPH, J., PACHAMUTHU, S., SOLOMON, J., AND SATHYAMURTHY, R. Experimental investigation to enhance the low-temperature nitrogen oxide emission reduction in biodiesel exhaust using selective catalytic reduction with direct ammonia injection and manganese cerium zirconia catalyst. *Environmental Progress & Sustainable Energy* (2021), e13622.

[85] JU, Y., REUTER, C., YEHIA, O., FAROUK, T., AND WON, S. Dynamics of cool flames. *Progress in Energy and Combustion Science 75* (2019), 100787.

[86] KANDA, T., HAKOZAKI, T., UCHIMOTO, T., HATANO, J., KITAYAMA, N., AND SONO, H. PCCI operation with early injection of conventional diesel fuel. *SAE Transactions* (2005), 584–593.

[87] KARIM, H., NATARAJAN, J., NARRA, V., CAI, J., RAO, S., KEGLEY, J., AND CITENO, J. Staged combustion system for improved emissions operability and flexibility for 7HA class heavy duty gas turbine engine. In *ASME turbo expo 2017: turbomachinery technical conference and exposition* (2017), American Society of Mechanical Engineers Digital Collection.

[88] KARIM, M. IMO mandatory energy efficiency measures for international shipping: the first mandatory global greenhouse gas reduction instrument for an international industry. *Macquarie J. Int'l & Comp. Envtl. L. 7* (2011), 111.

[89] KAZAKOV, A., CHAOS, M., ZHAO, Z., AND DRYER, F. Computational singular perturbation analysis of two-stage ignition of large hydrocarbons. *The Journal of Physical Chemistry A 110*, 21 (2006), 7003–7009.

[90] KHAIR, M., AND MAJEWSKI, W. Diesel emissions and their control. Tech. rep., SAE Technical Paper, 2006.

[91] KIRUBAKARAN, A., JAIN, S., AND NEMA, R. A review on fuel cell technologies and power electronic interface. *Renewable and Sustainable Energy Reviews 13*, 9 (2009), 2430–2440.

[92] KNOTHE, G. Biodiesel and renewable diesel: a comparison. *Progress in Energy and Combustion Science 36*, 3 (2010), 364–373.

[93] KOBAYASHI, H., HAYAKAWA, A., SOMARATHNE, K., AND OKAFOR, E. Science and technology of ammonia combustion. *Proceedings of the Combustion Institute 37*, 1 (2019), 109–133.

[94] KRISMAN, A., HAWKES, E., AND CHEN, J. Two-stage autoignition and edge flames in a high pressure turbulent jet. *Journal of Fluid Mechanics 824* (2017), 5–41.

[95] KRISMAN, A., HAWKES, E., AND CHEN, J. The structure and propagation of laminar flames under autoignitive conditions. *Combustion and Flame 188* (2018), 399–411.

[96] KRISMAN, A., MOUNAÏM-ROUSSELLE, C., SIVARAMAKRISHNAN, R., MILLER, J., AND CHEN, J. Reference natural gas flames at nominally autoignitive engine-relevant conditions. *Proceedings of the Combustion Institute 37*, 2 (2019), 1631–1638.

[97] LADOMMATOS, N., ABDELHALIM, S., ZHAO, H., AND HU, Z. The dilution, chemical, and thermal effects of exhaust gas recirculation on diesel engine emissions-part 1: effect of reducing inlet charge oxygen. Tech. rep., SAE Technical Paper, 1996.

[98] LAM, S. Singular perturbation for stiff equations using numerical methods. *Recent advances in the aerospace sciences* (1985), 3–19.

[99] LAPOINTE, S., SAVARD, B., AND BLANQUART, G. Differential diffusion effects, distributed burning, and local extinctions in high karlovitz premixed flames. *Combustion and Flame 162*, 9 (2015), 3341–3355.

[100] LECLERC, F. Detailed chemical kinetic models for the low-temperature combustion of hydrocarbons with application to gasoline and diesel fuel surrogates. *Progress in Energy and Combustion Science 34*, 4 (2008), 440–498.

[101] LEE, J. Dynamic parameters of gaseous detonations. *Annual Review of Fluid Mechanics 16*, 1 (1984), 311–336.

[102] LEE, J. *The detonation phenomenon*. 2008.

[103] LHUILLIER, C., BREQUIGNY, P., CONTINO, F., AND MOUNAÏM-ROUSSELLE, C. Experimental study on ammonia/hydrogen/air combustion in spark ignition engine conditions. *Fuel 269* (2020), 117448.

[104] LILLIESTAM, J., BIELICKI, J., AND PATT, A. Comparing carbon capture and storage (CCS) with concentrating solar power (CSP): Potentials, costs, risks, and barriers. *Energy policy 47* (2012), 447–455.

[105] LIPATNIKOV, A. Stratified turbulent flames: Recent advances in understanding the influence of mixture inhomogeneities on premixed combustion and modeling challenges. *Progress in Energy and Combustion Science 62* (2017), 87–132.

[106] LOPES, J., SOARES, F., AND ALMEIDA, P. Integration of electric vehicles in the electric power system. *Proceedings of the IEEE 99*, 1 (2010), 168–183.

[107] LU, T., YOO, C., CHEN, J., AND LAW, C. Three-dimensional direct numerical simulation of a turbulent lifted hydrogen jet flame in heated coflow: a chemical explosive mode analysis. *Journal of Fluid Mechanics 652* (2010), 45.

[108] LUCA, S., ATTILI, A., SCHIAVO, E., CRETA, F., AND BISETTI, F. On the statistics of flame stretch in turbulent premixed jet flames in the thin reaction zone regime at varying reynolds number. *Proceedings of the Combustion Institute 37*, 2 (2019), 2451–2459.

[109] LUNDGREN, T. Linearly forces isotropic turbulence. Tech. rep., Minnesota Univ Minneapolis, 2003.

[110] LUO, F., SONG, W., LI, J., CHEN, W., AND LONG, Y. Experimental study of kerosene supersonic combustion with pilot hydrogen and fuel additive under low flight mach conditions. *Energy 222* (2021), 119858.

[111] LUO, Z., YOO, C., RICHARDSON, E., CHEN, J., LAW, C., AND LU, T. Chemical explosive mode analysis for a turbulent lifted ethylene jet flame in highly-heated coflow. *Combustion and Flame 159*, 1 (2012), 265–274.

[112] LUONG, M., LUO, Z., LU, T., CHUNG, S., AND YOO, C. Direct numerical simulations of the ignition of lean primary reference fuel/air mixtures with temperature inhomogeneities. *Combustion and Flame 160*, 10 (2013), 2038–2047.

[113] MACDONALD, S., AND EYRE, N. An international review of markets for voluntary green electricity tariffs. *Renewable and Sustainable Energy Reviews 91* (2018), 180–192.

[114] MEHL, M., PITZ, W., WESTBROOK, C., AND CURRAN, H. Kinetic modeling of gasoline surrogate components and mixtures under engine conditions. *Proceedings of the Combustion Institute 33*, 1 (2011), 193–200.

[115] MEHTA, V., AND COOPER, J. Review and analysis of PEM fuel cell design and manufacturing. *Journal of Power Sources 114*, 1 (2003), 32–53.

[116] MEI, B., ZHANG, X., MA, S., CUI, M., GUO, H., CAO, Z., AND LI, Y. Experimental and kinetic modeling investigation on the laminar flame propagation of ammonia under oxygen enrichment and elevated pressure conditions. *Combustion and Flame 210* (2019), 236–246.

[117] MERCHANT, S., GOLDSMITH, C., VANDEPUTTE, A., BURKE, M., KLIPPENSTEIN, S., AND GREEN, W. Understanding low-temperature first-stage ignition delay: Propane. *Combustion and Flame 162*, 10 (2015), 3658–3673.

[118] MINETTI, R., CARLIER, M., RIBAUCOUR, M., THERSSEN, E., AND SOCHET, L. A rapid compression machine investigation of oxidation and autoignition of *n*-heptane: measurements and modeling. *Combustion and Flame 102*, 3 (1995), 298–309.

[119] MUSCULUS, M., MILES, P., AND PICKETT, L. Conceptual models for partially premixed low-temperature diesel combustion. *Progress in Energy and Combustion Science 39*, 2-3 (2013), 246–283.

[120] NA, K., BISWAS, S., ROBERTSON, W., SAHAY, K., OKAMOTO, R., MITCHELL, A., AND LEMIEUX, S. Impact of biodiesel and renewable diesel on emissions of regulated pollutants and greenhouse gases on a 2000 heavy duty diesel truck. *Atmospheric Environment 107* (2015), 307–314.

[121] NIEMEYER, K., AND SUNG, C. Mechanism reduction for multicomponent surrogates: A case study using toluene reference fuels. *Combustion and Flame 161*, 11 (2014), 2752–2764.

[122] NOJOUMI, H., DINCER, I., AND NATERER, G. Greenhouse gas emissions assessment of hydrogen and kerosene-fueled aircraft propulsion. *International Journal of Hydrogen Energy 34*, 3 (2009), 1363–1369.

[123] OVERHOLT, M., AND POPE, S. Direct numerical simulation of a passive scalar with imposed mean gradient in isotropic turbulence. *Physics of Fluids 8*, 11 (1996), 3128–3148.

[124] PAL, P., VALORANI, M., ARIAS, P., IM, H., WOOLDRIDGE, M., CIOTTOLI, P., AND GALASSI, R. Computational characterization of ignition regimes in a syngas/air mixture with temperature fluctuations. *Proceedings of the Combustion Institute 36*, 3 (2017), 3705–3716.

[125] PAN, J., WEI, H., SHU, G., CHEN, Z., AND ZHAO, P. The role of low temperature chemistry in combustion mode development under elevated pressures. *Combustion and Flame 174* (2016), 179–193.

[126] PEI, Y., DAVIS, M., PICKETT, L., AND SOM, S. Engine combustion network (ECN): Global sensitivity analysis of spray a for different combustion vessels. *Combustion and Flame 162*, 6 (2015), 2337–2347.

[127] PEI, Y., HAWKES, E., BOLLA, M., KOOK, S., GOLDIN, G., YANG, Y., POPE, S., AND SOM, S. An analysis of the structure of an *n*-dodecane spray flame using TPDF modelling. *Combustion and Flame 168* (2016), 420–435.

[128] PEIGHAMBARDOUST, S., ROWSHANZAMIR, S., AND AMJADI, M. Review of the proton exchange membranes for fuel cell applications. *International Journal of Hydrogen Energy 35*, 17 (2010), 9349–9384.

[129] PETERS, N. Turbulent combustion. cambridge university press, 2000.

[130] PETERS, N. Fifteen lectures on laminar and turbulent combustion. *Ercoftac Summer School 1428* (1992), 245.

[131] PETERS, N. Turbulent combustion, 2001.

[132] PETERS, N., PACZKO, G., SEISER, R., AND SESHADRI, K. Temperature cross-over and non-thermal runaway at two-stage ignition of *n*-heptane. *Combustion and Flame 128*, 1-2 (2002), 38–59.

[133] PETERS, N., TERHOEVEN, P., CHEN, J., AND ECHEKKI, T. Statistics of flame displacement speeds from computations of 2-D unsteady methane-air flames. In *Symposium (International) on Combustion* (1998), vol. 27, Elsevier, pp. 833–839.

[134] PICARELLI, A., SABIA, P., DE JOANNON, M., AND RAGUCCI, R. Autoignition delay times of methane/air diluted mixtures. numerical and experimental approaches. *Processes and Technologies for a Sustainable Energy* (2010), 1–8.

[135] PICKETT, L., GENZALE, C., BRUNEAUX, G., MALBEC, L., HERMANT, L., CHRISTIANSEN, C., AND SCHRAMM, J. Comparison of diesel spray combustion in different high-temperature, high-pressure facilities. *SAE International Journal of Engines 3*, 2 (2010), 156–181.

[136] PICKETT, L., KOOK, S., PERSSON, H., AND ANDERSSON, Ö. Diesel fuel jet lift-off stabilization in the presence of laser-induced plasma ignition. *Proceedings of the Combustion Institute 32*, 2 (2009), 2793–2800.

[137] PIERCE, C., AND MOIN, P. *Progress-variable approach for large-eddy simulation of turbulent combustion*. PhD thesis, Citeseer, 2001.

[138] PINEDA, D., PAXTON, L., PERAKIS, N., WEI, C., LUNA, S., KAHOULI, H., IHME, M., EGOLFOPOULOS, F., AND SPEARRIN, R. Carbon oxidation in turbulent premixed jet flames: A comparative experimental and numerical study of ethylene, *n*-heptane, and toluene. *Combustion and Flame 221* (2020), 371–383.

[139] PLEE, S., AHMAD, T., AND MYERS, J. Flame temperature correlation for the effects of exhaust gas recirculation on diesel particulate and NO_x emissions. *SAE Transactions* (1981), 3738–3754.

[140] PLEE, S., AHMAD, T., MYERS, J., AND FAETH, G. Diesel NO_x emissions—a simple correlation technique forintake air effects. In *Symposium (International) on Combustion* (1982), vol. 19, Elsevier, pp. 1495–1502.

[141] POINSOT, T., VEYNANTE, D., AND CANDEL, S. Diagrams of premixed turbulent combustion based on direct simulation. In *Symposium (international) on combustion* (1991), vol. 23, Elsevier, pp. 613–619.

[142] POPE, S. Turbulent flows, 2001.

[143] QIAO, B., HE, W., TIAN, Y., LIU, Y., CAI, O., AND LI, Y. Ship emission reduction effect evaluation of air pollution control countermeasures. *Transportation Research Procedia 25* (2017), 3606–3618.

[144] QUADRELLI, R., AND PETERSON, S. The energy–climate challenge: Recent trends in CO2 emissions from fuel combustion. *Energy policy 35*, 11 (2007), 5938–5952.

[145] RAHEMAN, H., AND GHADGE, S. Performance of diesel engine with biodiesel at varying compression ratio and ignition timing. *Fuel 87*, 12 (2008), 2659–2666.

[146] RAHMAN, I., VASANT, P., SINGH, B., ABDULLAH-AL-WADUD, M., AND ADNAN, N. Review of recent trends in optimization techniques for plug-in hybrid, and electric vehicle charging infrastructures. *Renewable and Sustainable Energy Reviews 58* (2016), 1039–1047.

[147] REITER, A., AND KONG, S. Demonstration of compression-ignition engine combustion using ammonia in reducing greenhouse gas emissions. *Energy & Fuels 22*, 5 (2008), 2963–2971.

[148] REITER, A., AND KONG, S. Combustion and emissions characteristics of compression-ignition engine using dual ammonia-diesel fuel. *Fuel 90*, 1 (2011), 87–97.

[149] REITZ, R., AND DURAISAMY, G. Review of high efficiency and clean reactivity controlled compression ignition (RCCI) combustion in internal combustion engines. *Progress in Energy and Combustion Science 46* (2015), 12–71.

[150] REŞITOĞLU, I., ALTINIŞIK, K., AND KESKIN, A. The pollutant emissions from diesel-engine vehicles and exhaust aftertreatment systems. *Clean Technologies and Environmental Policy 17*, 1 (2015), 15–27.

[151] ROGELJ, J., DEN ELZEN, M., HÖHNE, N., FRANSEN, T., FEKETE, H., WINKLER, H., SCHAEFFER, R., SHA, F., RIAHI, K., AND MEINSHAUSEN, M. Paris agreement climate proposals need a boost to keep warming well below 2° C. *Nature 534*, 7609 (2016), 631–639.

[152] ROGELJ, J., POPP, A., CALVIN, K., LUDERER, G., EMMERLING, J., GERNAAT, D., FUJIMORI, S., STREFLER, J., HASEGAWA, T., MARANGONI, G.,

ET AL. Scenarios towards limiting global mean temperature increase below 1.5° C. *Nature Climate Change 8*, 4 (2018), 325–332.

[153] ROSALES, C., AND MENEVEAU, C. Linear forcing in numerical simulations of isotropic turbulence: Physical space implementations and convergence properties. *Physics of Fluids 17*, 9 (2005), 095106.

[154] ROY, R., MUTO, M., AND KUROSE, R. Direct numerical simulation of ignition of syngas (H_2/CO) mixtures with temperature and composition stratifications relevant to HCCI conditions. *International Journal of Hydrogen Energy 42*, 41 (2017), 26152–26161.

[155] SABIA, P., DE JOANNON, M., PICARELLI, A., CHINNICI, A., AND RAGUCCI, R. Modeling negative temperature coefficient region in methane oxidation. *Fuel 91*, 1 (2012), 238–245.

[156] SANKARAN, R. Propagation velocity of a deflagration front in a preheated autoigniting mixture. In *9th US National Combustion Meeting, paper2E09* (2015).

[157] SANKARAN, R., IM, H., HAWKES, E., AND CHEN, J. The effects of non-uniform temperature distribution on the ignition of a lean homogeneous hydrogen–air mixture. *Proceedings of the Combustion Institute 30*, 1 (2005), 875–882.

[158] SAVARD, B., AND BLANQUART, G. An a priori model for the effective species lewis numbers in premixed turbulent flames. *Combustion and Flame 161*, 6 (2014), 1547–1557.

[159] SAVARD, B., AND BLANQUART, G. Broken reaction zone and differential diffusion effects in high karlovitz *n*-C_7H_{16} premixed turbulent flames. *Combustion and Flame 162*, 5 (2015), 2020–2033.

[160] SAVARD, B., BOBBITT, B., AND BLANQUART, G. Structure of a high karlovitz *n*-C_7H_{16} premixed turbulent flame. *Proceedings of the Combustion Institute 35*, 2 (2015), 1377–1384.

[161] SAVARD, B., DALAKOTI, D., WEHRFRITZ, A., AND HAWKES, E. Structure of (very) rich *n*-dodecane premixed turbulent flames at diesel engine conditions: a criterion to distinguish deflagrations from autoignition fronts. *Structure 10* (2018), 13.

[162] SAVARD, B., HAWKES, E., ADITYA, K., WANG, H., AND CHEN, J. Regimes of premixed turbulent spontaneous ignition and deflagration under gas-turbine reheat combustion conditions. *Combustion and Flame 208* (2019), 402–419.

[163] SAVARD, B., LAPOINTE, S., AND TEODORCZYK, A. Numerical investigation of the effect of pressure on heat release rate in iso-octane premixed turbulent flames under conditions relevant to SI engines. *Proceedings of the Combustion Institute 36*, 3 (2017), 3543–3549.

[164] SAVARD, B., WANG, H., TEODORCZYK, A., AND HAWKES, E. Low-temperature chemistry in *n*-heptane/air premixed turbulent flames. *Combustion and Flame 196* (2018), 71–84.

[165] SAVARD, B., WANG, H., WEHRFRITZ, A., AND HAWKES, E. Direct numerical simulations of rich premixed turbulent *n*-dodecane/air flames at diesel engine conditions. *Proceedings of the Combustion Institute 37*, 4 (2019), 4655–4662.

[166] SAVARD, B., WEHRFRITZ, A., LAM, K., MARGERTE, Q., FERNEY, L., AND FARJAM, S. Decreased mixture reactivity and hot flame speed in the products of diffusion-affected autoignitive cool flames in the ntc regime. *Combustion and Flame 222* (2020), 434–445.

[167] SAVARD, B., XUAN, Y., BOBBITT, B., AND BLANQUART, G. A computationally-efficient, semi-implicit, iterative method for the time-integration of reacting flows with stiff chemistry. *Journal of Computational Physics 295* (2015), 740–769.

[168] SCHULZ, O., AND NOIRAY, N. Autoignition flame dynamics in sequential combustors. *Combustion and Flame 192* (2018), 86–100.

[169] SCHULZ, O., AND NOIRAY, N. Combustion regimes in sequential combustors: Flame propagation and autoignition at elevated temperature and pressure. *Combustion and Flame 205* (2019), 253–268.

[170] SHAN, R., YOO, C., CHEN, J., AND LU, T. Computational diagnostics for *n*-heptane flames with chemical explosive mode analysis. *Combustion and Flame 159*, 10 (2012), 3119–3127.

[171] SHARMINA, M., EDELENBOSCH, O., WILSON, C., FREEMAN, R., GERNAAT, D., GILBERT, P., LARKIN, A., LITTLETON, E., TRAUT, M., VAN VUUREN,

D., ET AL. Decarbonising the critical sectors of aviation, shipping, road freight and industry to limit warming to 1.5–2° C. *Climate Policy* (2020), 1–20.

[172] SHEN, H., STEINBERG, J., VANDEROVER, J., AND OEHLSCHLAEGER, M. A shock tube study of the ignition of *n*-heptane, *n*-decane, *n*-dodecane, and *n*-tetradecane at elevated pressures. *Energy & Fuels 23*, 5 (2009), 2482–2489.

[173] SHIN, D., RICHARDSON, E., APARECE-SCUTARIU, V.AND MINAMOTO, Y., AND CHEN, J. Fluid age-based analysis of a lifted turbulent DME jet flame DNS. *Proceedings of the Combustion Institute 37*, 2 (2019), 2215–2222.

[174] SHIN, D., SANDBERG, R., AND RICHARDSON, E. Self-similarity of fluid residence time statistics in a turbulent round jet. *Journal of Fluid Mechanics 823* (2017), 1–25.

[175] SKEEN, S., MANIN, J., AND PICKETT, L. Simultaneous formaldehyde PLIF and high-speed schlieren imaging for ignition visualization in high-pressure spray flames. *Proceedings of the Combustion Institute 35*, 3 (2015), 3167–3174.

[176] SKEEN, S., MANIN, J., AND PICKETT, L. Visualization of ignition processes in high-pressure sprays with multiple injections of *n*-dodecane. *SAE International Journal of Engines 8*, 2 (2015), 696–715.

[177] SKIBA, A., WABEL, T., TEMME, J., AND DRISCOLL, J. Experimental assessment of premixed flames subjected to extreme turbulence. In *54th AIAA aerospace sciences meeting* (2016), p. 1454.

[178] SORIANO, B., AND RICHARDSON, E. Investigation of flame propagation in autoignitive blends of *n*-heptane and methane fuel. *Combustion Theory and Modelling 23*, 6 (2019), 1054–1070.

[179] STAGNI, A., CUOCI, A., FRASSOLDATI, A., FARAVELLI, T., AND RANZI, E. Lumping and reduction of detailed kinetic schemes: an effective coupling. *Industrial & Engineering Chemistry Research 53*, 22 (2014), 9004–9016.

[180] STEINBERG, A., HAMLINGTON, P., AND ZHAO, X. Structure and dynamics of highly turbulent premixed combustion. *Progress in Energy and Combustion Science 85* (2021), 100900.

[181] STRIK, D., HAMELERS, H., SNEL, J., AND BUISMAN, C. Green electricity production with living plants and bacteria in a fuel cell. *International Journal of Energy Research 32*, 9 (2008), 870–876.

[182] SU, L., ZHANG, M., WANG, J., AND HUANG, Z. Direct numerical simulation of DME autoignition with temperature and composition stratification under HCCI engine conditions. *Fuel 285* (2021), 119073.

[183] SUBRAMANIAN, S., SAJIN, J., AND PILLAI, G. Effect of ammonia to reduce emission from biodiesel fuelled diesel engine. *International Journal of Ambient Energy* (2019), 1–5.

[184] TAT, M., VAN GERPEN, J., AND WANG, P. Fuel property effects on injection timing, ignition timing and oxides of nitrogen emissions from biodiesel-fueled engines. In *2004 ASAE Annual Meeting* (2004), American Society of Agricultural and Biological Engineers, p. 1.

[185] TAVONI, M., KRIEGLER, E., RIAHI, K., VAN VUUREN, D., ABOUMAHBOUB, T., BOWEN, A., CALVIN, K., CAMPIGLIO, E., KOBER, T., JEWELL, J., ET AL. Post-2020 climate agreements in the major economies assessed in the light of global models. *Nature Climate Change 5*, 2 (2015), 119–126.

[186] TAY, K., YANG, W., CHOU, S., ZHOU, D., LI, J., YU, W., ZHAO, F., AND MOHAN, B. Effects of injection timing and pilot fuel on the combustion of a kerosene-diesel/ammonia dual fuel engine: a numerical study. *Energy Procedia 105* (2017), 4621–4626.

[187] TENNEKES, H., AND LUMLEY, J. *A first course in turbulence*. MIT Press, 2018.

[188] UPHAM, P., MAUGHAN, J., RAPER, D., AND THOMAS, C. *Towards sustainable aviation*. Earthscan, 2003.

[189] VAN OIJEN, J., LAMMERS, F., AND DE GOEY, L. Modeling of complex premixed burner systems by using flamelet-generated manifolds. *Combustion and Flame 127*, 3 (2001), 2124–2134.

[190] WANG, H., HAWKES, E., CHEN, J., ZHOU, B., LI, Z., AND ALDÉN, M. Direct numerical simulations of a high karlovitz number laboratory premixed jet flame–an analysis of flame stretch and flame thickening [direct numerical simulations of a high ka laboratory premixed jet flame-an analysis of flame stretch and flame thickening]. *Journal of Fluid Mechanics 815*, SAND-2017-0646J (2017).

[191] WANG, H., HAWKES, E., SAVARD, B., AND CHEN, J. Direct numerical simulation of a high Ka CH_4/air stratified premixed jet flame. *Combustion and Flame 193* (2018), 229–245.

[192] WANG, Y., ZHOU, X., AND LIU, L. Theoretical investigation of the combustion performance of ammonia/hydrogen mixtures on a marine diesel engine. *International Journal of Hydrogen Energy 46*, 27 (2021), 14805–14812.

[193] WEHRFRITZ, A., KAARIO, O., VUORINEN, V., AND SOMERS, B. Large eddy simulation of *n*-dodecane spray flames using flamelet generated manifolds. *Combustion and Flame 167* (2016), 113–131.

[194] WEI, H., ZHAO, W., LU, Z., AND ZHOU, L. Effects of oxygen concentrations on the ignition and quasi-steady processes of *n*-heptane spray flames using large eddy simulation. *Fuel 241* (2019), 786–801.

[195] WHITELEGG, J. Aviation: the social, economic and environmental impact of flying. *Ashden Trust, London* (2000).

[196] WINDOM, B., WON, S., REUTER, C., JIANG, B., JU, Y., HAMMACK, S., OMBRELLO, T., AND CARTER, C. Study of ignition chemistry on turbulent premixed flames of *n*-heptane/air by using a reactor assisted turbulent slot burner. *Combustion and Flame 169* (2016), 19–29.

[197] XU, C., PARK, J., YOO, C., CHEN, J., AND LU, T. Identification of premixed flame propagation modes using chemical explosive mode analysis. *Proceedings of the Combustion Institute 37*, 2 (2019), 2407–2415.

[198] XU, C., POLUDNENKO, A., ZHAO, X., WANG, H., AND LU, T. Structure of strongly turbulent premixed *n*-dodecane–air flames: Direct numerical simulations and chemical explosive mode analysis. *Combustion and Flame 209* (2019), 27–40.

[199] YANG, Y., NOIRAY, N., SCARPATO, A., SCHULZ, O., DÜSING, K., AND BOTHIEN, M. Numerical analysis of the dynamic flame response in alstom reheat combustion systems. In *Turbo Expo: Power for Land, Sea, and Air* (2015), vol. 56680, American Society of Mechanical Engineers, p. V04AT04A048.

[200] YAO, T., PEI, Y., ZHONG, B., SOM, S., LU, T., AND LUO, K. A compact skeletal mechanism for *n*-dodecane with optimized semi-global low-temperature chemistry for diesel engine simulations. *Fuel 191* (2017), 339–349.

[201] YEHIA, O., REUTER, C., AND JU, Y. Low-temperature multistage warm diffusion flames. *Combustion and Flame 195* (2018), 63–74.

[202] YOO, C., LU, T., CHEN, J., AND LAW, C. Direct numerical simulations of ignition of a lean *n*-heptane/air mixture with temperature inhomogeneities at constant volume: Parametric study. *Combustion and Flame 158*, 9 (2011), 1727–1741.

[203] ZELDOVICH, Y. Regime classification of an exothermic reaction with nonuniform initial conditions. *Combustion and Flame 39*, 2 (1980), 211–214.

[204] ZHANG, M., ONG, J., PANG, K., BAI, X.-S., AND WALTHER, J. An investigation on early evolution of soot in *n*-dodecane spray combustion using large eddy simulation. *Fuel 293* (2021), 120072.

[205] ZHANG, T., AND JU, Y. Structures and propagation speeds of autoignition-assisted premixed *n*-heptane/air cool and warm flames at elevated temperatures and pressures. *Combustion and Flame 211* (2020), 8–17.

[206] ZHEN, X., LI, X., WANG, Y., LIU, D., AND TIAN, Z. Comparative study on combustion and emission characteristics of methanol/hydrogen, ethanol/hydrogen and methane/hydrogen blends in high compression ratio si engine. *Fuel 267* (2020), 117193.

[207] ZHOU, B., BRACKMANN, C., LI, Q., WANG, Z., PETERSSON, P., LI, Z., ALDÉN, M., AND BAI, X.-S. Distributed reactions in highly turbulent premixed methane/air flames: Part I. flame structure characterization. *Combustion and Flame 162*, 7 (2015), 2937–2953.

[208] ZHOU, T., ZHAO, P., YE, T., ZHU, M., AND TAO, C. Direct numerical simulation of low temperature reactions affecting *n*-dodecane spray autoignition. *Fuel 280* (2020), 118453.

Appendix A

Time sequences of heat release rate 2D contours

All the contour plots mentioned in Table 3.1 are presented in this appendix. Figures A.1, A.2, A.3, A.4, A.5, and A.6 are shown according to their respective inflow velocity and each contain different Reynolds number cases as subfigures. Figure A.7 shows the cases with $l/l_F = 2$. Figure A.8 depicts cases with 21% oxygen level in the ambient gas.

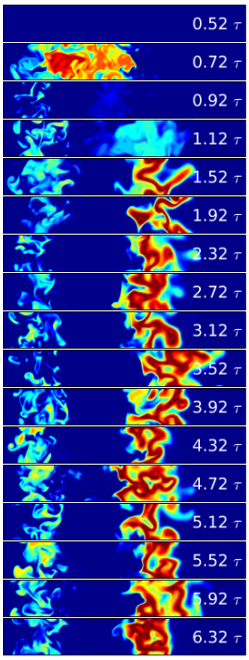

(a) $U_{\text{in}}/S_L = 4$, $Re_t = 50$ (case 1).

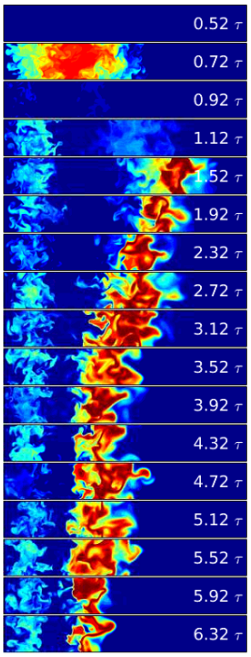

(b) $U_{\text{in}}/S_L = 4$, $Re_t = 120$ (case 2).

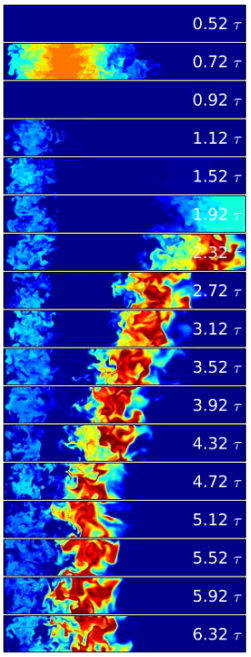

(c) $U_{\text{in}}/S_L = 4$, $Re_t = 180$ (case 3).

(d) Color scale (logarithmic), ranging from 10 to 12.5 log(Jm$^{-3}s^{-1}$).

FIGURE A.1: 2D HRR contours corresponding with properties of $l/l_F = 1$, $O_2 = 15\%$, $U_{\text{in}}/S_L = 4$, showing (a) $Re_t = 50$, (b) $Re_t = 120$, (c) $Re_t = 180$.

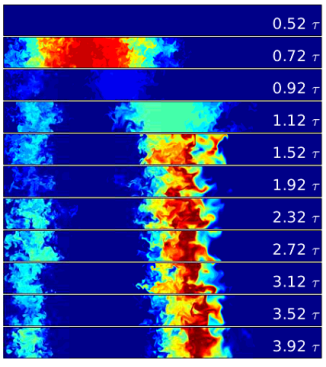

(a) $U_{\text{in}}/S_L = 6$, $Re_t = 220$ (case 4).

FIGURE A.2: 2D HRR contours corresponding with properties of $l/l_F = 1$, $O_2 = 15\%$, $U_{\text{in}}/S_L = 6$, and $Re_t = 220$.

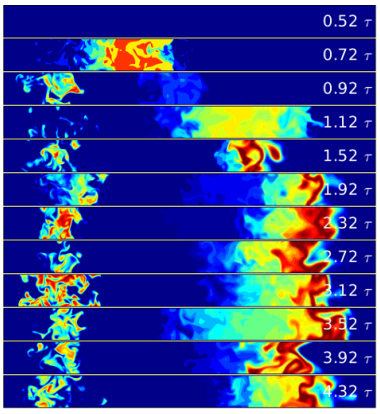

(a) $U_{\text{in}}/S_L = 7$, $Re_t = 50$ (case 5).

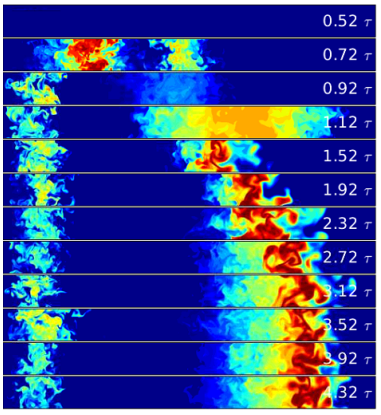

(b) $U_{\text{in}}/S_L = 7$, $Re_t = 120$ (case 6).

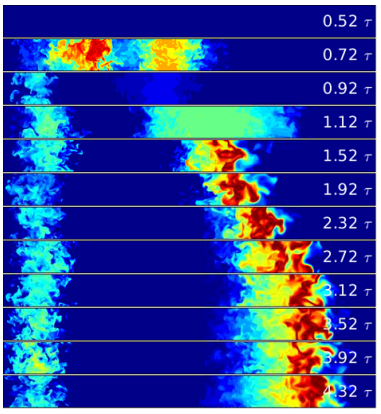

(c) $U_{\text{in}}/S_L = 7$, $Re_t = 180$ (case 7).

FIGURE A.3: 2D HRR contours corresponding with properties of $l/l_F = 1$, $O_2 = 15\%$, $U_{\text{in}}/S_L = 7$, showing (a) $Re_t = 50$, (b) $Re_t = 120$, (c) $Re_t = 180$.

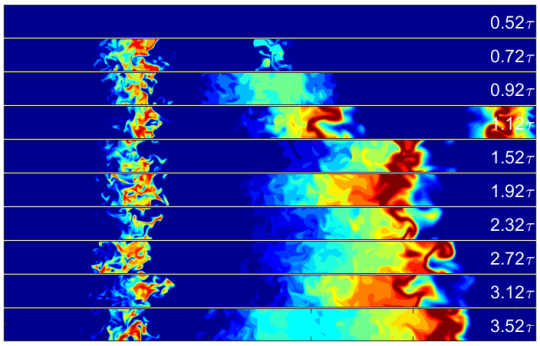

(a) $U_{\text{in}}/S_L = 10$, $Re_t = 50$ (case 8).

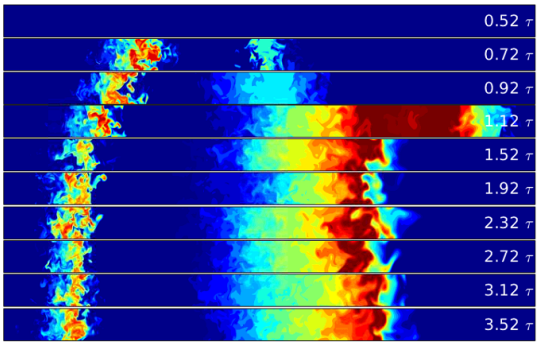

(b) $U_{\text{in}}/S_L = 10$, $Re_t = 120$ (case 9).

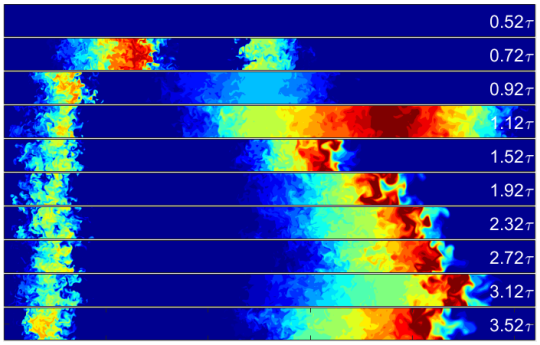

(c) $U_{\text{in}}/S_L = 10$, $Re_t = 180$ (case 10).

FIGURE A.4: 2D HRR contours corresponding with properties of $l/l_F = 1$, $O_2 = 15\%$, $U_{\text{in}}/S_L = 10$, showing (a) $Re_t = 50$, (b) $Re_t = 120$, (c) $Re_t = 180$.

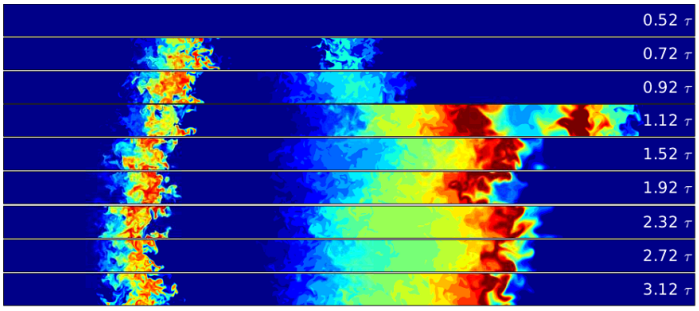

(a) $U_{\text{in}}/S_L = 13$, $Re_t = 120$ (case 11).

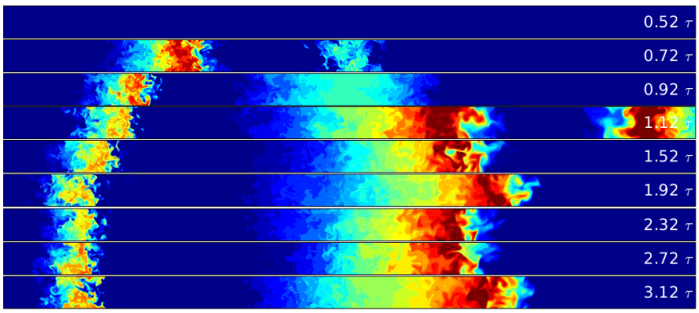

(b) $U_{\text{in}}/S_L = 13$, $Re_t = 180$ (case 12).

FIGURE A.5: 2D HRR contours corresponding with properties of $l/l_F = 1$, $O_2 = 15\%$, $U_{\text{in}}/S_L = 13$, showing (a) $Re_t = 120$, (b) $Re_t = 180$.

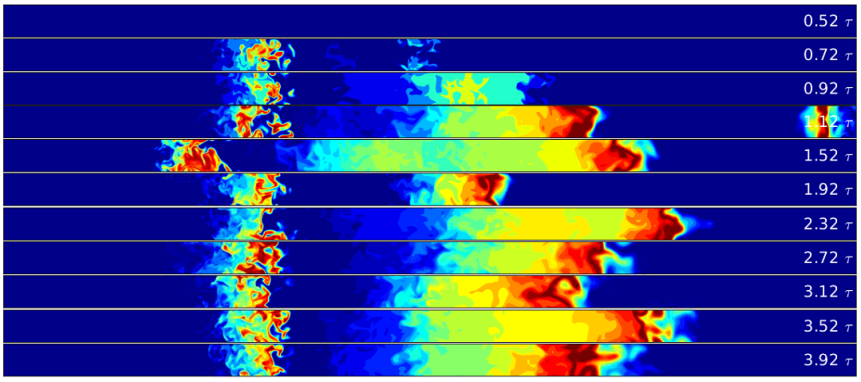

(a) $U_{\text{in}}/S_L = 16$, $Re_t = 50$ (case 13).

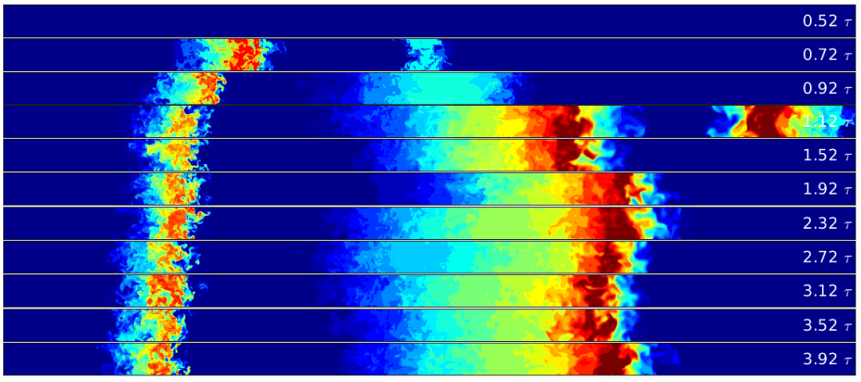

(b) $U_{\text{in}}/S_L = 16$, $Re_t = 180$ (case 14).

FIGURE A.6: 2D HRR contours corresponding with properties of $l/l_F = 1$, $O_2 = 15\%$, $U_{\text{in}}/S_L = 16$, showing (a) $Re_t = 50$, (b) $Re_t = 180$.

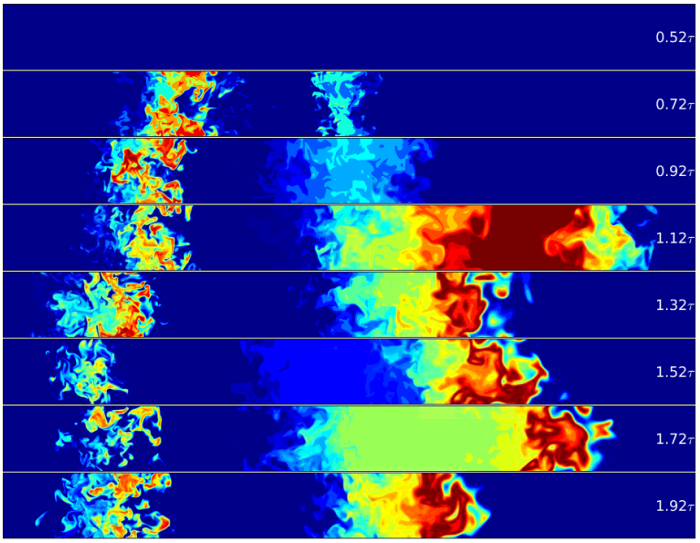

(a) $l/l_F = 2$, $U_{\text{in}}/S_L = 13$, $Re_t = 180$ (case 15).

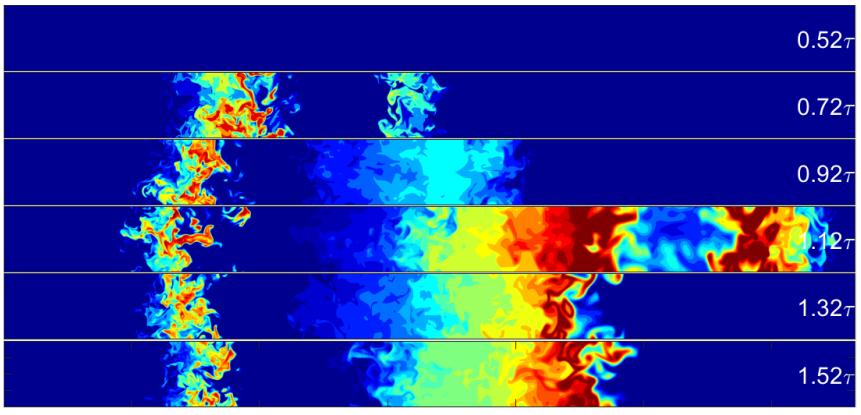

(b) $l/l_F = 2$, $U_{\text{in}}/S_L = 16$, $Re_t = 180$ (case 16).

FIGURE A.7: 2D HRR contours corresponding with properties of $l/l_F = 2$, $O_2 = 15\%$, showing (a) $U_{\text{in}}/S_L = 13$, $Re_t = 180$, (b) $U_{\text{in}}/S_L = 16$, $Re_t = 180$.

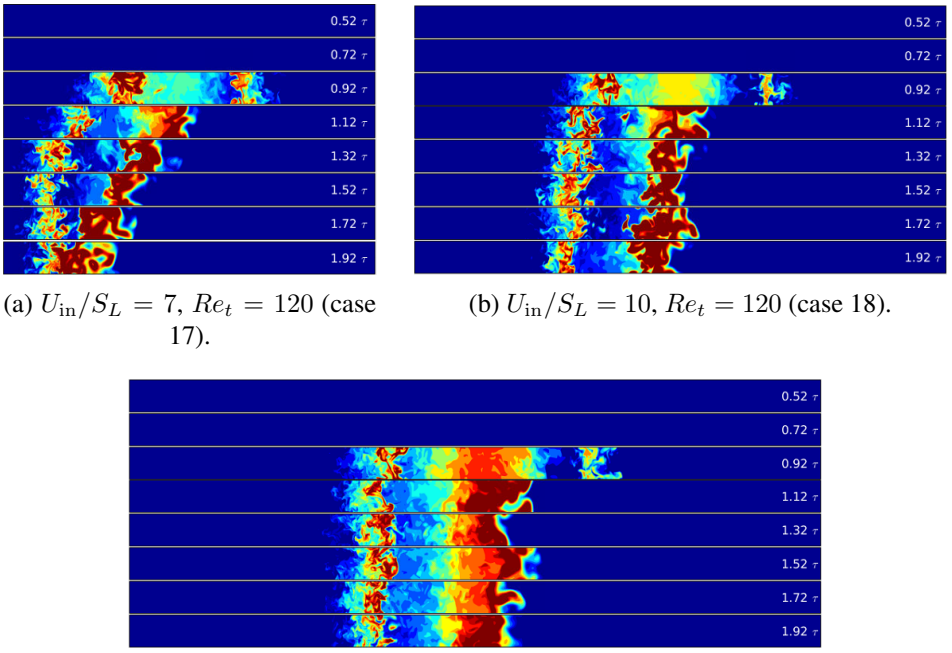

(a) $U_{\text{in}}/S_L = 7$, $Re_t = 120$ (case 17).

(b) $U_{\text{in}}/S_L = 10$, $Re_t = 120$ (case 18).

(c) $U_{\text{in}}/S_L = 13$, $Re_t = 120$ (case 19).

FIGURE A.8: 2D HRR contours corresponding with properties of $l/l_F = 1$, $O_2 = 21\%$, showing (a) $U_{\text{in}}/S_L = 7$, $Re_t = 120$, (b) $U_{\text{in}}/S_L = 10$, $Re_t = 120$, (c) $U_{\text{in}}/S_L = 13$, $Re_t = 120$.

Appendix B

Enthalpy and heat loss

Enthalpy and the equivalent temperature loss for all the turbulent simulations are shown in Figures B.1 and B.2, respectively. According to Fig. B.1, enthalpy reduces as the effect of diffusion increases and the flame transitions. The equivalent temperature loss (ΔT) in Fig. B.2 is calculated as the difference of the inlet and the outlet enthalpy over the specific heat c_p. Highest heat loss is seen for the case with the most diffusion contribution ($U_{\text{in}}/S_L = 4, Re_t = 180$) with 5.5 K temperature loss. Heat loss for the rest of the cases are fairly low, hence, verifying the integrity of the simulations. Figure B.3 shows a comparison between enthalpy of the laminar reference case and a laminar deflagration case to that of the turbulent cases, with respect to the distance from the inlet. An interesting observation is that the turbulent case 3 (most deflagrative turbulent case) from Table 3.1 is showing heat loss (blue line) while we have enthalpy gain in the laminar most diffusive cases (purple line). This variation may be due to a competition between heat loss through conduction and species diffusive flux (with associated enthalpy) at the inlet. Nevertheless, the trends shown in the thesis match well between turbulent and laminar cases which suggests that this flux of enthalpy at the inlet may not have much impact.

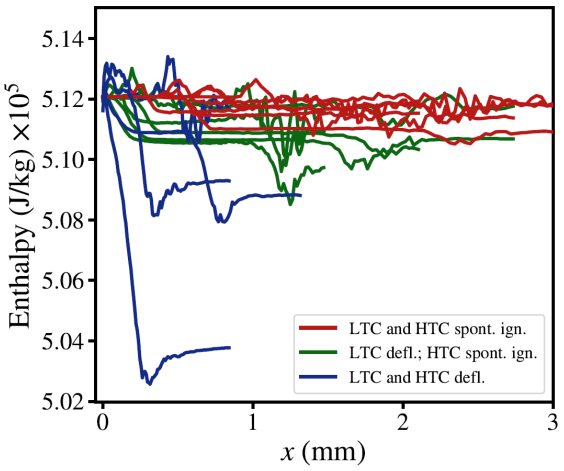

FIGURE B.1: Enthalpy vs distance.

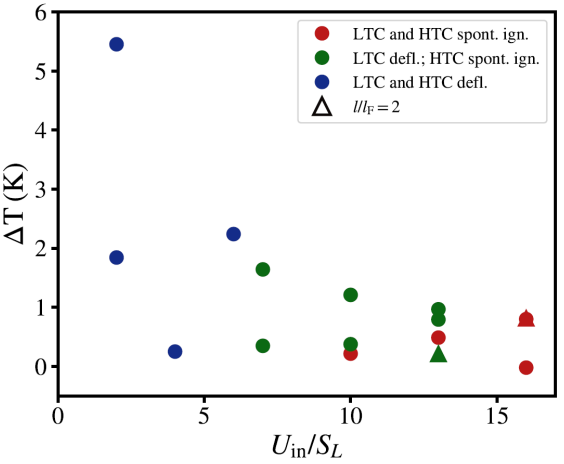

FIGURE B.2: Equivalent temperature loss for turbulent cases.

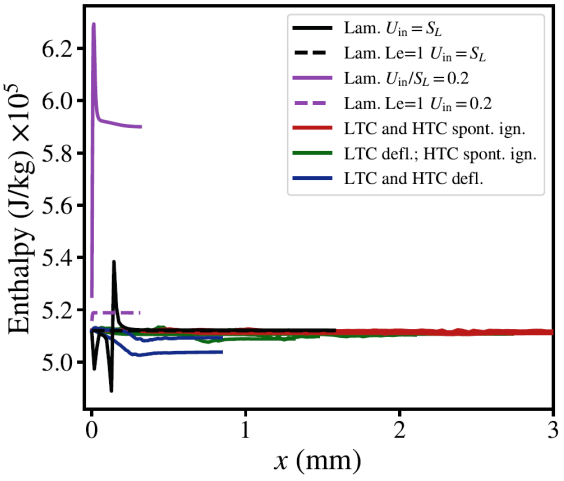

FIGURE B.3: Comparison between enthalpy variations of turbulent cases and laminar.